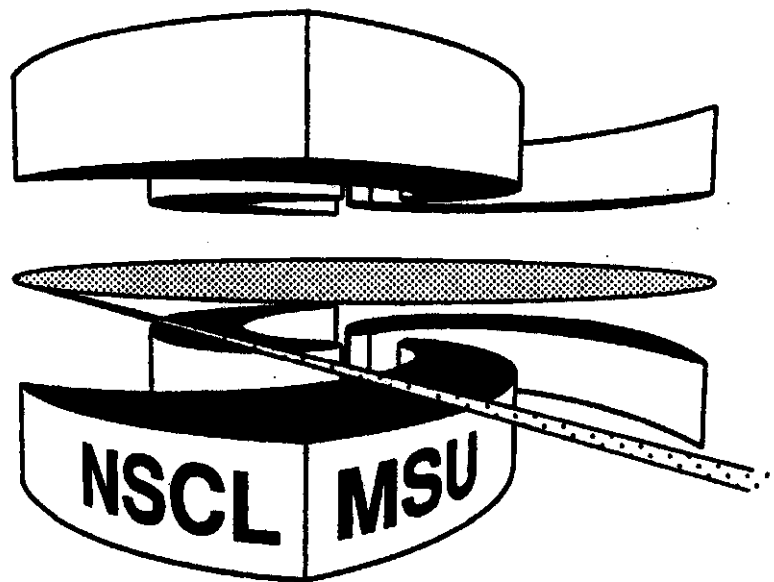# Michigan State University

National Superconducting Cyclotron Laboratory

**Effects of Compression and Collective Expansion
on Particle Emission from Central Heavy-Ion Reactions**

Pawel Danielewicz

Effects of Compression and Collective Expansion on Particle Emission' from Central Heavy-Ion Reactions

P. Danielewicz*

National Sup-conducting Cyclotron Laboratory and

Department of Physics and Astronomy, Michigan State University,

East Lansing, Michigan 48824, USA

(August 16, 1994)

Abstract

Conditions under which compression occurs and collective expansion develops in energetic symmetric reactions of heavy nuclei, are analyzed, together with their effects on emitted light baryons and pions. Within transport simulations, it is shown that shock fronts perpendicular to beam axis form in head-on reactions. The fronts separate hot compressed matter from normal and propagate into projectile and target. As impact parameter increases, the angle of inclination of the fronts relative to beam axis decreases, and in-between the fronts a weak tangential discontinuity develops. Hot matter exposed to the vacuum in directions perpendicular to shock motion (and parallel to fronts), starts to expand sideways, early within reactions. Expansion in the direction of shock motion follows after the shocks propagate through nuclei, but due to the delay does not acquire same strength. Expansion affects angular distributions, mean-energy components, shapes of spectra and

---

'e-mail: danielewicz@nscl.nscl.msu.edu

mean energies of different particles emitted into any one direction, and further particle yields. Both the anisotropy in the expansion and a collective motion associated with the weak discontinuity, affect the magnitude of sideward flow within reaction plane. Differences in mean particle energy components in and out of the reaction plane in semicentral collisions, depend sensitively on the relative magnitude of shock speed in normal matter and speed of sound in hot matter. The missing energy, considered in the past in association with low measured pion-multiplicity in central reactions, may be identified with the energy of collective expansion. Relations are established which approximately govern the behavior of density and entropy in the compressed region in reactions with beam energy and impact parameter.

PACS numbers: 27.75.+r, 21.65.+f, 24.10.-i

2

I. INTRODUCTION

Within the past two decades a considerable effort in the area of energetic heavy-ion reactions was put into identification of signatures of collective phenomena in excited nuclear matter. Particular effort was devoted to the effects of collective motion. The latter has been understood as a motion characterized by the correlation between particle positions and momenta, of a dynamic origin. Early attempts to identify signatures of collective phenomena in single-particle observables were, generally, plagued by ambiguities. Thus it was anticipated [1–3] that nuclear matter gets stopped in the very central collisions, compressed and heated, and subsequently expands primarily in the directions perpendicular to the beam axis. The expansion was suggested [4] to be the cause of observed differences in the transverse slopes of the inclusive pion and proton spectra. However, it was further realized that the production of pions in the reactions mainly proceeds through the Δ resonance excitation and decay, and thus the pion slopes could reflect the Δ-decay kinematics [5]. A sideward peaking of the proton angular distributions in an asymmetric reaction gave a hint of the expected collective behavior [6]. As eventually, though, the neutron distributions had shown no such peaking [7], one was led to the conclusion that the peaking of the proton distributions was a Coulomb effect [8]. Stock *et al.* [9] noted that the measured pion multiplicities in central collisions, lower than predicted within the cascade or fireball models, could be explained by assuming that a part of the available energy was used up for compressing nuclear matter. Subsequent dynamic calculations of collisions [10] have demonstrated, though, a weak sensitivity of the pion yields to the compressibility of matter.

Analyses of the 4π data brought fairly unambiguous evidence [11] of what appeared to be a different type of collective motion than first envisioned in the head-on collisions. This was a sideward deflection in the reaction plane of the fragments moving forward and backward in the center of mass in semicentral collisions. The deflection was quantified with a flow angle or with an average momentum in the reaction plane at a given rapidity. At midrapidity, at high beam energies, a preference was found for fragments to be emitted out of the reaction

plane [12,13]. It has not been obvious whether this preference was of a dynamic origin or due to shadowing. At low energies the emission in the reaction plane was found to be enhanced [14].

Recent years brought new important results on the motion in central reactions. Specifically, Schussler et al. [15,16] have investigated the mean c.m. energies of fragments emitted from the central reactions with Ag in emulsion. For the incident ^{36}Ar ions at 65 ± 15 MeV, and the incident ^{94}Kr ions at 95 ± 25 MeV, they observed a rise of these energies with fragment charge, faster than anticipated on the basis of Coulomb considerations alone. For the two reactions the rise was consistent with a collective expansion characterized by the energy of ~ 3 MeV/nucleon and $\gtrsim 7$ MeV/nucleon, respectively. No rapid rise was observed for the incident ^{16}O ions at 210 ± 10 MeV. The FOPI collaboration at GSI has further analysed the spectra and mean energies of fragments with different charge emitted from central Au + Au collisions at beam energies in the range (150-400) MeV/nucleon [17,18]. They have found that the spectra of fragments with large Z were too broad and, respectively, the mean energies too high to be accounted for by a model of purely statistical decay. Within preliminary analysis [17], data description improved once an assumption of the collective expansion at the time of decay was introduced, of an energy ~ 18 MeV/nucleon at the beam energy 150 MeV/nucleon, and of an energy ~ 51 MeV/nucleon at 400 MeV/nucleon, respectively. In a later more cautious investigation [18], the collective energy was bounded from below with ~ 10 MeV/nucleon in the 150 MeV/nucleon reaction. The fragment yields were separately analysed to extract entropy [19] within the so-called Quantum Statistical Model (QSM). Low entropy values were extracted consistent with low temperatures at reasonable values of freeze-out density. (These values were lower than those extracted in the past from light-fragment yields [20]). The collective expansion could alleviate but not eliminate discrepancies between the temperatures and energy available in the center of mass. Further analysis of spectra for collective motion in a central 100 MeV/nucleon Au + Au reaction was done in [21].

On the theoretical side, emission from central collisions has been analysed within a trans-

4

port model with a dynamic light-fragment production ($A \leq 3$) [22]. Within this model the compression and excitation of nuclear matter in central collisions was observed, followed by an expansion. The mean energies of emitted fragments were observed to rise with the fragment mass, and a rough consistency has been established between the rise with the mass and the collective energy determined from the dynamics. The calculated energies partially agreed and partially disagreed with the Plastic Ball data [23]. A degree of agreement of the calculations was found [24], on the other hand, with the preliminary FOPI data on light fragments. Within the calculations [22], the expansion affected, besides energies, the fragment angular-distributions. A midrapidity out-of-the-reaction-plane peaking at intermediate impact parameters in a heavy system, in a quantitative agreement with the data [13] (see also Refs. [25,26]), was identified as a continuation, with the rise of impact parameter, of a 90° peaking in the polar angle in head-on reactions.

Spurred by the recent experimental evidence [15–18,21] and some forthcoming results [27,24,28], this study extends that carried out in [22]. Very preliminary results have been presented in [29]. Conditions under which a compression occurs in energetic reactions of heavy nuclei, and a collective expansion develops, are analyzed in detail, together with their effects on emitted light baryons and pions. Relations are established which approximately govern the behavior of density and entropy in the compressed region in reactions, with beam energy and impact parameter. Anisotropies in particle emissions in the polar angle in head-on reactions and in the azimuthal angle in semicentral reactions, are explained in terms of a different starting time for expansions in different directions. Besides the effects of collective expansion on baryon and pion spectra, effects on particle yields are demonstrated. The effects on pions turn out to be dramatic, contrary to naive expectations. The role of expansion in the formation of hollow structures at lower energies [30–32,34] is elucidated. The analysis renders an understanding of both recent and older data.

The outline of the paper is as follows. Section II describes the model used for reaction analysis. Section III is devoted to the dynamics and some observables from symmetric head-on reactions of heavy-nuclei. The gained experience is next utilized in the study of

semi-central reactions in Sec. IV. Section V is devoted to the effects of collective expansion on pion yields, effects of the expansion on spectra of relativistic particles in general, and to shadowing of pions in semi-central reactions. Results on entropy and on collective expansion energy from measurements and simulations are discussed in Sec. VI. Section VII discusses the sensitivity of collective energy and its components to nuclear compressibility and elementary cross sections, and further the mechanism of formation of exotic structures at low energies. The results are summarized Sec. VIII.

II. TRANSPORT MODEL

Reaction simulations are carried out within a transport model with explicit nucleon, deuteron, $A = 3$ cluster, pion, and delta and N^* degrees of freedom [35,22]. The phase-space occupation functions f_X of stable particles satisfy transport equations following from the nonequilibrium many-body theory in the quasiparticle limit,

$$\frac{\partial f_X}{\partial t} + \frac{\partial E_X}{\partial \mathbf{p}_X} \cdot \frac{\partial f_X}{\partial \mathbf{r}} - \frac{\partial E_X}{\partial \mathbf{r}} \cdot \frac{\partial f_X}{\partial \mathbf{p}_X} = \mathcal{K}_X^{\lessgtr}(1 \mp f_X) - \mathcal{K}_X^{\gtrless} f_X. \tag{1}$$

In the above E_X is the single-particle energy, and $\mathcal{K}_X^{\lessgtr}$ and $\mathcal{K}_X^{\gtrless}$ are, respectively, the production and absorption rates of the particle X. The upper and lower signs in the statistical factor on the r.h.s are for fermions and bosons, respectively.

The deuterons within the model are formed in the interaction of three nucleons [35,37,38]. The formation rate [38,35] contributing to the deuteron production rate has a form analogous to that of the rate associated with elastic scattering,

$$\begin{aligned}
\mathcal{K}_d^{\lessgtr}(\mathbf{P}) = {}& \frac{8}{3} \frac{m_d}{E_d(\mathbf{P})} \sum_{N=n,p} \int \frac{d\mathbf{p}}{(2\pi)^3} \frac{m_N}{E_N(\mathbf{p})} \frac{d\mathbf{p}_1'}{(2\pi)^3} \frac{m_N}{E_N(\mathbf{p}_1')} \frac{d\mathbf{p}_2'}{(2\pi)^3} \frac{m_N}{E_N(\mathbf{p}_2')} \frac{d\mathbf{p}'}{(2\pi)^3} \frac{m_N}{E_N(\mathbf{p}')} \\
& \times \frac{1}{2} \overline{|\mathcal{M}_{Npn \to Nd}|^2} (2\pi)^3 \delta(\mathbf{P} + \mathbf{p} - \mathbf{p}_1' - \mathbf{p}_2' - \mathbf{p}') 2\pi \delta(E_d(\mathbf{P}) + E_N(\mathbf{p}) \\
& - E_p(\mathbf{p}_1') - E_n(\mathbf{p}_2') - E_N(\mathbf{p}')) (1 - f_N(\mathbf{p})) f_p(\mathbf{p}_1') f_n(\mathbf{p}_2') f_N(\mathbf{p}') + \cdots, \tag{2}
\end{aligned}$$

The dots indicate other terms in the production rate. The factor $\overline{|\mathcal{M}|^2}$ stands for the matrix element squared summed over the final and averaged over the initial spin directions.

6

A term in the deuteron absorption rate accounting for the deuteron breakup into nucleons has an analogous form to the term for the formation (2), with statistical factors for the initial and final states interchanged. Due to the microscopic reversibility the processes of deuteron formation and breakup share the matrix elements squared. The averaged elements squared are then related with the ratio of spin-degeneracies,

$$\overline{|\mathcal{M}_{Npn \to Nd}|^2} = \frac{3}{4}\overline{|\mathcal{M}_{Nd \to Npn}|^2}. \tag{3}$$

In principle, data on deuteron breakup could be used in describing the formation as the differential cross section for breakup is proportional to the matrix element squared,

$$d\sigma_{Nd \to Npn} = \frac{1}{v_1} \frac{m_N}{E_N(\mathbf{p_1})} \overline{|\mathcal{M}_{Nd \to Npn}|^2} 2\pi\delta(m_d + E_N(\mathbf{p_1}) - E_N(\mathbf{p'_1}) - E_p(\mathbf{p'_2}) - E_n(\mathbf{p'_3}))$$
$$\times (2\pi)^3 \delta(\mathbf{p_1} - \mathbf{p'_1} - \mathbf{p'_2} - \mathbf{p'_3}) \frac{m_N}{E_N(\mathbf{p'_1})} \frac{d\mathbf{p'_1}}{(2\pi)^3} \frac{m_p}{E_p(\mathbf{p'_2})} \frac{d\mathbf{p'_2}}{(2\pi)^3} \frac{m_n}{E_n(\mathbf{p'_3})} \frac{d\mathbf{p'_3}}{(2\pi)^3}. \tag{4}$$

In practise, due to the dimensionality of three-body space, the differential cross section is known only within a limited range. In the calculations, a modified impulse approximation is thus used

$$\overline{|\mathcal{M}_{pd \to ppn}|^2} \simeq F\Big\{ |\langle p'_1|\phi_d\rangle|^2 \overline{|\mathcal{M}_{pn \to pn}|^2} + |\langle p'_2|\phi_d\rangle|^2 \overline{|\mathcal{M}_{pn \to pn}|^2}$$
$$+ |\langle p'_3|\phi_d\rangle|^2 \overline{|\mathcal{M}_{pp \to pp}|^2} \Big\}, \tag{5}$$

where ϕ_d is the deuteron wave-function in momentum space, normalized so that

$$\int \frac{d\mathbf{p}}{(2\pi)^3} |<p|\phi>|^2 = 1.$$

The three terms in (5) correspond to the three different nucleons being spectators. The NN matrix elements in are proportional to the NN cross sections. Finally, the overall normalization factor F in (5) is adjusted so that the measured total deuteron breakup cross section is reproduced as a function of bombarding energy [35].

Tritons and helions in the transport model are produced in the interactions involving four nucleons [36,22]. The production of a composite is generally suppressed if the average nucleon occupation over a volume in momentum space, corresponding to the composite wave-function, exceeds a phenomenological cutoff-value of 0.30. At low densities, in the limit of

many interactions, the set of equations for the composites and nucleons yields the required law of mass action. A coalescence scaling [39] for the composite spectra is expected to emerge from the model based on the equations, when the processes of composite production do not vary substantially with space and time.

The pions within the model are produced in two steps [40]. First a Δ or N^* resonance is produced in an NN collision, and then the resonance decays into a nucleon and pion. The cross section for the resonance production appears to nearly exhaust the inelastic NN cross section in the energy range of interest [41]. The resonance occupation functions satisfy transport equations that follow from the nonequilibrium many-body theory in the adiabatic limit [35],

$$\frac{\partial}{\partial t}(f_X \, \mathcal{A}_X) + \frac{\partial E_X}{\partial \mathbf{p}_X}\cdot\frac{\partial}{\partial \mathbf{r}}(f_X \, \mathcal{A}_X) - \frac{\partial E_X}{\partial \mathbf{r}}\cdot\frac{\partial}{\partial \mathbf{p}_X}(f_X \, \mathcal{A}_X) = \mathcal{K}_X^{\lessgtr}(1 \mp f_X)\mathcal{A}_X - \mathcal{K}_X^{\gtrless}f_X\mathcal{A}_X, \quad (6)$$

where $\mathcal{A}_X$ is the spectral function describing the spread of the resonance in mass,

$$\mathcal{A}_X = \frac{\Gamma_X}{(m - m_X)^2 + \frac{1}{4}\Gamma_X^2}, \quad (7)$$

and Γ_X is the resonance width which generally depends on m. The derivatives on the l.h.s. of Eq. (6) are taken at a constant $m - m_X$. The absorption of pions is described with a sequence of inverse processes to those in the production. The resonance formation dominates the πN cross section at the energies of interest, with the cross section for resonance X of the form [42],

$$\sigma_{\pi N \to X} = \frac{\pi}{p^2}\frac{g_X}{2}\Gamma_{X \to \pi N}\mathcal{A}_X \quad (8)$$

with p - c.m. momentum and g_X - resonance spin-degeneracy. Microscopic reversibility and the assumption of a weak dependence of the interaction matrix-element squared on the resonance mass, yield a relation between the cross sections for resonance absorption and production [35,43],

$$\sigma_{XN \to N'N''} = \frac{1}{1 + \delta_{N'N''}}\frac{2}{g_X}\frac{m\,p_{N'N''}^2}{p_{XN}}\frac{\sigma_{N'N'' \to XN}}{\int^{E-m_N} d\widetilde{m}\mathcal{A}_X(\widetilde{m})\widetilde{p}_{XN}}, \quad (9)$$

8

where E is total energy. A variant [44] of the relation relies on the assumption of a rapid variation of the matrix element, for m close to $E - m_N$. In the calculations preceeding [35], a detailed balance relation between the resonance production and absorption cross-sections used was such as for stable particles, leading to an excessive number of pions in equilibrium. In the pion-nucleus interactions the true pion absorption cross section was underestimated. Further violating reversibility in the calculations, in (8) the momentum prefactor was replaced by a constant, affecting the shape of pion spectra.

The single-particle energies in Eqs. (1) and (6) are parametrized in terms of an optical potential, with a local part handled as a scalar potential, and a weaker nonlocal part added on to the particle energies in the system c.m.,

$$E_X = (p^2 + m^2)^2 + q_X \, \Phi + A_X \, U_1^C, \qquad m = m_0 + A_X \, U^C + t_{3X} \, U^T, \qquad (10)$$

where q_X is particle charge, Φ – Coulomb potential, A_X – particle mass number, m_0 – mass in free space, and t_{3X} – isospin component. The dependence of the potentials U on scalar densities is chosen such as in nonrelativistic calculations,

$$U^C = -a \frac{\rho_s}{\rho^0} + b \left(\frac{\rho_s}{\rho^0} \right)^\nu, \qquad U_1^C = -d \, \nabla^2 \left(\frac{\rho_s}{\rho^0} \right), \qquad U^T = c \frac{\rho_s^T}{\rho^0}, \qquad (11)$$

where

$$\rho_s = \sum_X A_X \rho_{sX}, \qquad \rho_s^T = \sum_X t_{3X} \rho_{sX}, \qquad (12)$$

with

$$\rho_{sX} = g_X \int \frac{d\mathbf{p}}{(2\pi)^3} \frac{m_{X0}}{E_X} f_X, \quad \text{and} \quad \rho_{sX} = g_X \int \frac{d\mathbf{p}}{(2\pi)^3} \int \frac{dm}{2\pi} \frac{m_{X0}}{E_X} f_X \qquad (13)$$

for the stable particles and resonances, respectively. The neutron and proton density profiles for initial nuclei are determined by solving a differential equation for baryon density that follows from the Thomas-Fermi (TF) equations in the nuclear frames,

$$E_p(r, p_{Fp}(r)) = \mu_p, \qquad E_n(r, p_{Fn}(r)) = \mu_n. \qquad (14)$$

9

The chemical potentials μ_p and μ_n are adjusted till the values of total proton and neutron numbers for nuclei are reproduced. It appears convenient to solve differential equations set up for the proton and neutron numbers, Coulomb potential, and net energy in parallel to the equation for baryon density.

The normal density is taken equal to $\rho_0 = 0.160\ \text{fm}^{-3}$. The description of charge densities from electron scattering [45] is better with this value than with $\rho_0 = 0.145\ \text{fm}^{-3}$ [22]. As to the other parameters in (11), $a = 357$ MeV, $b = 304$ MeV, and $\nu = \frac{7}{6}$ correspond to the soft equation of state ($K \simeq 200$ MeV), and $a = 123$ MeV, $b = 70.1$ MeV, and $\nu = 2$ to the stiff equation ($K \simeq 375$ MeV); $c = 92$ MeV, $d = 22.4\ \text{MeV fm}^2$ [46,47]. Sample densities for the second parameter set are shown in Fig. 1. Unless otherwise indicated other results in the paper are obtained using the second set. The effects of the momentum dependent potentials on the expansion have not been explored as of yet, due to the involved numerical difficulties with energy conservation and a specific interest in the differences between mean energies and spectra of different emitted fragments.

Occupation functions in the phase space for stable particles, and in the phase space and mass for resonances, are represented in the calculation with test particles. The drift terms on the l.h.s. of Eqs. (1) and (6) are integrated by requiring that the test-particle positions and momenta satisfy the Hamilton's equations. A lattice hamiltonian method of Lenk and Pandharipande [46] is used with the scalar density at lattice sites evaluated with a form factor

$$S_X(\mathbf{r},p) = \frac{A_X}{N_{test}(2\ell)^3} \frac{m_{X0}}{E_X} g(x)g(y)g(z), \qquad (15)$$

where $g(q) = 1$ for $|q| < 0.5\ell$, $g(q) = 1.5 - |q|/\ell$ for $0.5\ell < |q| < 1.5\ell$, $g(q) = 0$ for $|q| > 1.5\ell$. Further, N_{test} is the number of test particles per particle, and ℓ is lattice spacing. The particular form of g allows for a good total energy conservation (to within 0.25 MeV/nucleon in a 100 MeV/nucleon collision), and a good momentum conservation for asymmetric systems, with no considerable computational effort. It should be mentioned that an initialization of the system according to the densities from the TF equations is essential for

an "elastic" algorithm for the drift terms. For other, however sensible, initializations, isolated nuclei develop strong breathing oscillations that can deplete central density to a quarter of normal value. The Coulomb potential is found by solving the Poisson equation using a novel relaxation method [48]. Integrals in the collision rates in Eqs. (1) and (6) are computed using the Monte-Carlo method [35] (see also Ref. [49]). Entropy is calculated by integrating [35] the rate of entropy variation due to collisions.

III. HEAD-ON COLLISIONS OF HEAVY NUCLEI

Emphasis is going to be on symmetric reactions of heavy nuclei. For symmetric systems the experimental identification of specific collective effects may be less ambiguous than for asymmetric systems, due to the well defined center of mass and the lack of shadowing at lowest impact parameters.

A. Shock Fronts

The dynamics of the central high-energy reactions can be broken down into several well identified stages. A 400 MeV/nucleon Au + Au system at $b = 0$ will be used to illustrate specific points. Contour plots of baryon density at different times for that system are shown in the left column of Fig. 2. Initially in the energetic reactions the nuclear densities just interpenetrate, with target and projectile nucleons separated in the momentum space. As the time progresses, in the overlap region NN collisions begin to thermalize the matter, making the momentum distribution centered at zero momentum in the c.m.s. Thereafter, the features of the matter at the center of a system stabilize to a degree. As further the region with the excited matter grows in size, in a heavy system interface regions can be identified in-between the excited and normal matter where such parameters as baryon and entropy density change rapidly, see Figs. 2 and 3. In the head-on collisions the interfaces are perpendicular to the beam axis. With the normal matter diving into the region with excited matter at a speed well in excess of the speed of sound in normal matter (for the first

11

sound the speed is $c_s = \sqrt{K/9m_N}$, i.e. $0.15c$ and $0.21c$ in the case of soft and stiff equation of state, respectively), at the high beam energies, the interfaces are recognized as shock fronts. In the hydrodynamic limit a discontinuity in the velocity in the initial state, such as in-between the projectile and target nucleons at $b = 0$, generally breaks into two shock fronts travelling in opposite directions [50]. Figure 4 displays the nuclear-matter parameters within the hydrodynamic limit, behind a shock front bringing the matter to a halt, as a function of beam energy, obtained by solving the Rankine-Hugoniot (RH) equation [50]

$$\frac{(e_1 + P_1)^2}{\rho_1^2} - \frac{e_0^2}{\rho_0^2} - P_1 \left(\frac{e_1 + P_1}{\rho_1^2} + \frac{e_0}{\rho_0^2} \right) = 0. \tag{16}$$

The parameters with subscript 1 in (16) refer to the shocked matter and e and P are the energy density (including mass) and pressure, respectively. Figure 4 displays further the maximum densities from the $b = 0$ Au + Au simulations and these densities appear to follow the general trend predicted by (16). The excited matter in-between shock fronts in the simulations is exposed to the vacuum in the sideward directions and, respectively, begins to expand into these directions. The features of this process at high energies and at $b = 0$ may be understood at a *qualitative* level in terms of the self-similar cylindrically-symmetric hydrodynamic expansion of an ideal gas.

B. Expansion

In the self-similar expansion [51,52], the velocity is proportional to a distance from the symmetry axis, $v = \mathcal{F}(t)\, r$, which roughly appears to hold in the direction of 90° in the Au + Au collision at 400 MeV/nucleon, cf. Fig. 3. Under the simplifying assumptions of an isentropic flow and an ideal-gas equation of state, yielding $P/\rho^\gamma = \text{const}$ with γ - the heat ratio, the solution to nonrelativistic hydrodynamic equations for the density becomes

$$\rho(r, t) = \rho(0, 0) \frac{R^2(0)}{R^2(t)} \left(1 - \frac{r^2}{R^2(t)} \right)^{1/(\gamma - 1)}. \tag{17}$$

The radius R of the density distribution satisfies

$$\ddot{R}(t) = \frac{2c_s^2(0,0)}{\gamma R(0)} \left(\frac{R(0)}{R(t)}\right)^{2\gamma-1}, \tag{18}$$

with $c_s^2 = \gamma T/m$ - the speed of sound squared. The coefficient $\mathcal{F}$ is related to R with $\mathcal{F}(t) = \dot{R}(t)/R(t)$. Equation (18) may be partially integrated to yield, for $\dot{R}(0) = 0$,

$$\dot{R}(t) = c_s(0,0) \left[\frac{2}{\gamma(\gamma-1)} \left(1 - \left(\frac{R(0)}{R(t)}\right)^{2\gamma-1}\right)\right]^{1/2}. \tag{19}$$

Following Eqs. (18) and (19), the coefficient $\mathcal{F}$ is expected to rise, first linearly, for the time $t \sim R/c_s$ needed for a signal to propagate inward through the radius, and it is expected to fall off later as the inverse of time, reflecting the quadratic initially and linear asymptotically dependence of R on time. Indeed, in the high-energy simulations, the velocity slope dv/dr in the transverse direction, cf. Fig. 3, behaves approximately as described. Within the nonrelativistic ideal-gas approximation, the speed of sound in the central region of the collision at 400 MeV/nucleon is assessed, with $\gamma = 5/3$, at $c_s \sim 0.4c$. The radius of the gold nucleus is ~ 7 fm, and thus the slope might be expected to rise for a time ~ 18 fm/c. The maximum in the simulations is reached at $t \sim 27$ fm/c which appears consistent with the simple estimate as initially some time is spent equilibrating and compressing matter, cf. Fig. 5. The value at maximum $dv/dr \approx 0.040$ c/fm is not far from the one obtained by integrating (19), $\mathcal{F} \approx 0.6\,c_s/R \sim 0.036$ c/fm. At the given instant, according to (19), the transverse matter radius should be about 50% in excess of the original which approximately is the case in the simulation, cf. Figs. 2 and 3. After the time R/c_s, the density in the central region of the reaction should decrease as t^{-2}, following Eqs. (17) and (19).

While the expansion develops in transverse directions, the normal matter continues to enter the excited region along the beam axis for a time $\sim (2R/v_0)(\rho_1 - \rho_0)/\rho_1 \sim 16$ fm/c in the Au + Au collision. Here $v_0 \approx 0.42\,c$ is initial velocity in the center of mass and ρ_1 is the density in the shocked region. After the shock fronts reach the vacuum, an expansion *along* the beam axis sets in that requires a time $\sim (2R/c_s)(\rho_0/\rho_1) \sim 18$ fm/c for a full development. By then, however, the matter is already quite decompressed with particles having moved out in the transverse directions. At the later stages, with the expansion becoming three-

13

dimensional, the density in the central region can be expected to drop as t^{-3}.

While the discussed and few other dynamic features of $b = 0$ high-energy reactions appear to be consistent with a hydrodynamic behavior of the matter, there are also definite differences which cannot be classified as effects of the mean-field potential or relativity. Thus, the baryon density at the center of the system, Figs. 3, 4, and 5, falls short of the value of $2.5\,\rho_0$ expected at 400 MeV/nucleon on the basis of the RH equation. The entropy per baryon never quite reaches values expected for an equilibrated system at the center. Typical combinations of density and mean nucleon kinetic energy such as $\rho \sim 2.1\,\rho_0$ and $E_{kin} \sim$ 91 MeV, should result in $S_B/A \sim 2.8$, compare Fig. 3. For reference, the nonrelativistic formula for the entropy, with statistics ignored, is

$$\frac{S_B}{A} = 2.5 - \log\left(\frac{\rho}{4}\left(\frac{3\pi\hbar^2}{m_N E_{kin}}\right)^{3/2}\right). \tag{20}$$

The shock fronts do not fully develop [53] and/or the system never gets completely thermalized at the center (see also [54]). In a system expanding hydrodynamically into vacuum, local temperatures would have dropped to zero and all kinetic energy would have turned into the collective energy of expansion [51,52]. For that, collisions would need to continue down to appropriately low densities. The mean density in the vicinity of last collisions of particles emitted from head-on Au + Au reactions, is shown as a function of the beam energy in Fig. 6. At 400 MeV/nucleon the freeze-out density is equal to about $0.2\rho_0$. The bottom panel in Fig. 5 shows the evolution of the participant collective transverse energy per nucleon in the 400 MeV/nucleon reaction, which is calculated from the perpendicular components of a local hydrodynamic velocity $\mathbf{v}$ in the vicinity of last collisions,

$$E_{coll}^{\perp}/A = \sum_X \int dr d\mathbf{p} f_X m_X (v^{\perp})^2 \bigg/ \sum_X A_X \int dr d\mathbf{p} f_X . \tag{21}$$

The collective transverse energy per nucleon freezes out in Fig. 5 at a value of 42 MeV. For nucleons this constitutes about 50% of the kinetic energy in transverse degrees of freedom at the freeze-out. (A bit larger fraction is found if relativistic effects are taken into account.) The nuclear systems are, indeed, too small for the entire energy to turn into the collective energy. Simple estimates of mean freeze-out density based on

14

$$\langle \rho \rangle \simeq \int dt \, \frac{\rho}{\tau} \exp\left(\int^t \frac{dt'}{\tau}\right)$$

where $\tau = (\rho \sigma_{NN} v^*)^{-1}$ and v^* is relative thermal velocity, that utilize a nuclear density $\rho(t) \propto t^{-\nu}$ where $\nu = (2 - 3)$, and rely on the assumptions of either adiabatic or isothermal expansion yield $\langle \rho \rangle / \rho_1 \propto (\sigma_{NN} R \rho_1)^{-\kappa}$, where ρ_1 is the density at the start of expansion and κ ranges from 2/3 to 2. Following these estimates, the energy dependence of the freeze-out density seen in Fig. 6, above 100 MeV/nucleon, may be attributed to the variation of elementary cross sections of particles interacting locally with reduced relative velocities. If cross sections are made energy-independent in simulations, indeed little change in $\langle \rho \rangle$ is observed towards high energies.

One of the effects of transverse expansion on observables from very central collisions in the simulations, is the peaking of particle polar-angle distributions at 90° in the c.m.s. This peaking is more pronounced in the distributions of clusters which are more affected by the hydrodynamic motion than are nucleons [55], see e.g. Fig. 7. With the variation of beam energy, the peaking is observed to maximize at about 150 MeV/nucleon. Below 40 MeV/nucleon the emission turns isotropic. The shock width at low energies becomes comparable to the nuclear size [53] and thus a system equilibrates as a whole. For polar-angle distributions from the simulations of 250 MeV/nucleon reactions see Ref. [22]. At very high energies (and/or for light systems like Ca + Ca) the effects of expansion in the simulations compete with the transparency effects in the corona. The proton distributions become forward-backward peaked in the c.m.s., at beam energies above 1.5 GeV/nucleon, and the light-cluster distributions above 1.9 GeV/nucleon in the Au + Au reactions. As seen in Fig. 7, the pion polar-angle distribution peaks at $\theta = 0$ already at 1 GeV/nucleon. For the purpose of demonstrating that, indeed, the transparency plays a role, the figure shows, in addition to the distribution of all pions, the distribution of only those pions which were emitted within the first 14 fm/c. The latter pions constitute about 1/3 of all, and the anisotropy of their polar-angle distribution is nearly 3 times larger than the anisotropy for all. (Possible effects of geometry in a surface emission in shaping the pion angular distribution may

15

be eliminated, as the angular distributions at lower energies are peaked at 90°.) Despite the transparency effects in the corona, the maximum densities at the center of the Au + Au system are not farther away from the RH expectations at the highest of the studied energies than at lower,[1] cf. Fig. 4. The peaking of particle distributions at 90° at $b = 0$, including that for pions at lower beam energies, eventually disappears with an increase of impact parameter [22]. Experimentally, the most central collisions can be selected by using the particle transverse energies or symmetry around the beam axis [18]. In order to avoid a bias in the angular distributions, the analysed particles should be *excluded* from the trigger condition (compare [56]). By forcing the condition to a limit the extraction of information from most central collisions could be reduced to the issue of collecting an adequate event statistics.

Figure 8 shows the mean transverse and longitudinal kinetic-energy components [22],

$$E_{kin} = E - m = \sqrt{m^2 + p^2} - m = \frac{(p^{\perp})^2}{m + E} + \frac{(p^{\parallel})^2}{m + E} = E^{\perp} + E^{\parallel}, \qquad (22)$$

of particles emitted from the $b = 0$ Au + Au collisions, as a function of the bombarding energy. The scale for the transverse component is shifted downward by log 2 relative to the scale for the longitudinal component, in order to allow for a direct visual comparison of the components *per degree of freedom* at the same bombarding energy. It is seen that, per degree of freedom, the transverse baryon energies are higher than longitudinal in a vast range of bombarding energies. This is a reflection of higher, per degree of freedom, collective transverse energy than longitudinal, at freeze-out [22]. The components of the collective energy per nucleon, calculated as in Eq. (21), are shown in Fig. 9. If particle momentum distributions are approximated with anisotropic gaussians and nonrelativistic kinematics is used, then the particle polar-angle distributions become

---

[1] In a comparison in [22] over a more narrow range of energies, the pions and baryon resonances were omitted in the RH prediction and some nonrelativistic approximation was made. Besides, the predictions there were for another equation of state.

$$\frac{4\pi}{N}\frac{dN}{d\Omega} = \frac{(1+\chi)^{1/2}}{(1+\chi\cos^2\theta)^{3/2}}, \tag{23}$$

where $\chi = (\langle E^\perp \rangle/2 - \langle E^\| \rangle)/\langle E^\| \rangle$. Result (23) for tritons emitted from a 1 GeV/nucleon Au + Au collision is shown by a solid line in Fig. 7. In general, it is found that Eq. (23) describes the distributions of emitted particles from high-energy collisions in a semi-quantitative way, even the pion distributions. The 90°-to-0° ratios,

$$R_\theta = \left(\frac{dN}{d\Omega}\right)_{90°} \bigg/ \left(\frac{dN}{d\Omega}\right)_{0°},$$

are quite well described within the approximation, $R_\theta \approx (1+\chi)^{3/2} = (\langle E^\perp \rangle/2\langle E^\| \rangle)^{3/2}$. Within the gaussian approximation, the mean particle energy at 90° is equal to [22] 1.5 × $\langle E^\perp \rangle$. The mean energies at 90° in simulations are slightly lower.

IV. SEMICENTRAL COLLISIONS

The attention is now turned to the dynamics of semicentral collisions, with emphasis put on the similarities and differences compared to the dynamics at $b = 0$.

A. Hydrodynamic Discontinuities

The initial discontinuity between the projectile and target velocities breaks at a finite b in the ideal-fluid limit into two shock fronts propagating into the projectile and target, and a weak tangential discontinuity in-between [55,50]. Unlike across a shock front, the normal velocity component, pressure and, in the case at hand, entropy and density are continuous across the tangential discontinuity, and the tangential velocity component is not. The discontinuities start out in collisions all at the same angle α relative to the beam axis, cf. Figs. 10 and 2,

$$\cos\alpha \approx \frac{b}{2R}\frac{1}{\sqrt{1+(E_{beam}/2m_N)(1+b^2/4R^2)}}, \tag{24}$$

where the beam energy is in MeV/nucleon, and the Lorentz contraction in the c.m.s. is taken into account ($v_0 = (1 + 2m_N/E_{beam})^{-1/2}$, $\gamma_0 = \sqrt{1 + E_{beam}/2m_N}$). Developing inclined shocks can be seen in the $t = 10$ fm/c panels of Fig. 2 for a finite b. Signs of a tangential discontinuity for a finite b are visible in the densities at later times in the figure. Figure 11 shows finally the variation of different quantities along a normal to discontinuities in a collision at $b = 7$ fm. Note that the center of the weak discontinuity is at $r = 0$ where v_t vanishes, while the center of a shock is at $r \sim 3.1$ fm where v_n reaches 1/2 of the value for the intact matter.

In the ideal-fluid limit, the tangential component of a velocity would be unaltered by a shock, and thus the matter behind the shock in collisions would be expected to move at a speed $v_1 = v_0 \cos \alpha$ and angle α relative to the beam axis. The change in the thermodynamic parameters should be then such as for a shock perpendicular to the beam axis, at $b = 0$ and a beam energy (called further an equivalent energy)

$$E'_{beam} = E_{beam} \sin^2 \alpha, \tag{25}$$

where relativity has been thoroughly accounted for. The ideal-fluid dynamics predicts then that the maximum density reached early on in collisions in the c.m. at a finite b, is related to the density at $b = 0$ at a lower beam energy, by

$$
\begin{aligned}
\rho_1(b, E_{beam}) &= \gamma_1 \rho_1(0, E'_{beam}) \\
&= \left(1 - \frac{\beta \epsilon}{(1 + \epsilon)(1 + \epsilon(1 + \beta))}\right)^{-1/2} \rho_1\left(0, E_{beam} \frac{(1 + \epsilon)(1 - \beta)}{1 + \epsilon(1 + \beta)}\right) \\
&\approx \rho_1(0, E_{beam}(1 - \beta)) = \rho_1(0, E_{beam}(1 - b^2/4R^2)), \tag{26}
\end{aligned}
$$

where $\epsilon = E_{beam}/2m_N$ and $\beta = b^2/4R^2$. The approximation following the equalities in (26) is nonrelativistic ($\epsilon \ll 1$). The c.m. maximum density and corresponding rest-frame parameters like entropy behind the shock fronts are expected to change slowly according to (25) and (24), only quadratically, with the rise of b. Indeed, a weak variation behind the shock fronts is found in the simulations. The validity of the relativistic relation (26)

18

is tested in the top panel of Fig. 4 that displays, in particular, the maximum density from 1 GeV/nucleon Au + Au collisions at different b, divided by γ_1, vs E'_{beam} from (26). The relation appears to work up to $b \sim 11$ fm at this and other beam energies. Further predictions based on the ideal-fluid dynamics need not work as well.

In the simulations all the discontinuities have widths that are quite comparable to the size of a system, see Fig. 11. The tails of the weak and strong discontinuities overlap and in consequence the velocity in-between does not, in fact, reach values such as if the discontinuities were separated. For example, at low b, along the axis passing through the center, the magnitude of the transverse velocity component in the reaction plane reaches at most 40% of $(v_0 \sin \alpha \cos \alpha)$ expected in-between separated discontinuities. As a function of time, the width of any shock front (of the order of a mean-free path for a strong shock) remains constant [53,50], provided that the conditions on the two sides of the front remain the same. The width of a tangential discontinuity, on the other hand, increases with time. That this must be the case can be seen directly by adopting the hydrodynamic Navier-Stokes equations [57] to a region of the discontinuity, where they yield a diffusion equation for the tangential component of velocity (or for vorticity $\omega = \nabla \times \mathbf{v}$). The diffusion coefficient is equal to $\eta/(m_N\rho)$, where η is the shear viscosity coefficient (proportional, in general, to the mean-free path). Solving this diffusion equation yields the tangential velocity component as a function of time t and distance r in a direction perpendicular to the discontinuity, in the form

$$v_t(r,t) = v_t^0 \, \text{erf}\left(\frac{r}{2}\sqrt{\frac{m_N\rho}{\eta t}}\right), \tag{27}$$

where v_t^0 is an asymptotic value of the velocity component and erf is error function. According to Eq. (27) the half-width of a weak discontinuity should rise with time as $\delta = 2\sqrt{\eta t/m_N\rho}$. For the situation in Fig. 11, with $\eta \sim 50$ MeV/fm^{2}c [53], this yields $\delta \approx 3.2$ fm which agrees well with what can be deduced from the simulation in the figure. Generally, during the time span lasting from the initial equilibration in simulations till the development of the expansion at intermediate and low impact parameters, the tangential-velocity profile at the

center, is reasonably well described by Eq. (27), despite of the proximity of shocks. The root in (27) alleviates uncertainties associated with the choice of density and a reference time. While δ increases as $t^{1/2}$, the separation between shocks increases as t, and thus, if nuclear systems were large enough and/or viscosity low, the shocks in collisions could separate well from the weak discontinuity, before reaching the vacuum. For large Reynolds numbers $\mathcal{R} = m_N \rho v R / \eta$ the weak discontinuity at the center could break into a turbulence [50]. In the system studied $\mathcal{R} \sim 9$, while typical critical values for turbulence are larger [50]. No sign of any turbulence is seen in the simulations.

In the course of a reaction, the section of the weak discontinuity turns from one given by a straight line to one reminding a hyperbolic tangent, and on the average the discontinuity rotates, decreasing an angle relative to the beam axis. That is because the matter moving forward on one side of a reaction plane, away from the center of the system, emerges facing little or no target matter moving the other way. Symmetrically, the target matter on the other side emerges facing little or no projectile matter. The shock fronts subsonic relative to the matter behind rotate as well. The fronts are generally strong in the vicinity of an axis passing through the center of a system in the direction of the beam; there from the shock in projectile matter continues as strong towards the target side of the reaction plane, and the shock in target matter as strong towards the projectile side of the reaction plane. With the excited region within the geometric overlap of projectile and target fed by incoming matter, the density is maintained behind the shocks during the shock propagation.

The shock in projectile matter is weakest in the vicinity of its edge on the projectile side of the reaction plane. There the front curves, making a low angle relative to the beam axis, the change in the velocity component normal to the front is low, and correspondingly the equivalent energy for the front is low, compare (25). Symmetrically, the front moving into target matter is weakest in the vicinity of its edge on the target side of the reaction plane. The distinction between the strong and weak portions of the fronts is generally pronounced at high beam energies but less at low. The weak shocks propagate with only slightly supersonic velocities relative to the intact matter. These shocks, in what becomes

20

spectator matter at high energies, might remind those away from supersonic bodies moving through a medium. The matter little disturbed by the weak shocks can move out as an entity largely in its original direction in the c.m., see the $t = 35$ fm/c panel in Fig. 2 for $b = 7$ fm. (The spectator matter separates out also in the reaction at $b = 3$ fm at a later time than shown in the figure; the shapes for the matter are far from spherical.)

If the hydrodynamic discontinuities in the region of geometric overlap between projectile and target, were more separated in the simulations, the matter would have moved more to the sides within the reaction plane behind the shocks, strengthening the shock edges. The spectator matter would not have been then as distinct; see the results in [58]. Weakness of the sideward flow in collisions [59], as compared to the ideal-fluid predictions, and the emergence of spectator matter are thus very directly related.

B. Expansion

From the shock formation on, an expansion proceeds to develop in-between the fronts. At low b the expansion in the directions perpendicular to the reaction plane has features similar to the expansion in the directions perpendicular to the beam axis at $b = 0$. The variation of baryon density, entropy and radial velocity at different time instants, with the distance from the center of the system along a line defined by $\theta = 90°$ and $\phi = 90°$, where ϕ is the azimuthal angle relative to the reaction plane, is quite close to the variation given by the dashed lines in Fig. 3. The top panel in Fig. 12 shows the dependence on the impact parameter of the mean particle kinetic energy components out of the reaction plane $E^y = (p^y)^2/(m + E)$, where p^y is the momentum component out of the reaction plane, at c.m. rapidity $y = 0$. It is seen that the mean energy components depend roughly quadratically on b for low values of b (i.e. in such a manner as the maximum density in the collisions). Center panel in the figure shows the energies E^y averaged over whole momentum space. These averages are equal to half of $\langle E^\perp \rangle$ at $b = 0$, and they decrease faster with an increase of b than the averages at $y = 0$, because of larger spectator contributions. Either type of average energies may be

determined experimentally, correcting for fluctuations of the reaction plane [12,60,56].

With regard to the directions in the vicinity of the reaction plane, the initial velocities tangential to the weak discontinuity behind shock fronts (although low compared to those in the ideal-fluid limit) add on to the velocities developed in expansion, and affect the sideward-flow observables. The deflection of particles moving forward and backward in the c.m. is commonly quantified in terms of the mean momentum in the reaction plane as a function of the rapidity [56]. Figure 13 shows the mean momentum divided by the mass, $\langle p^x(y)\rangle/m$, for particles emitted from Au + Au reactions at 1 GeV/nucleon at two impact parameters. For the purpose of minimizing the effects of spectator particles at high energy, the slope of the mean momentum at midrapidity is further used in analyses [61]. The slope

$$F = \frac{d\langle p^x/m\rangle}{dy} \tag{28}$$

is shown in Fig. 14 for 400 MeV/nucleon Au + Au collisions, as a function of the impact parameter, both for the calculations and data. This slope generally increases with particle mass. If the emission pattern at low b and low c.m. rapidities differed from that at $b = 0$ *only* by a rotation of the plane of preferred emission, from the angle of 90° relative to the beam axis, to an effective angle α, then the slope F at midrapidity should be approximately [12,62]

$$F \approx \frac{\chi \sin\alpha \cos\alpha}{1 + \chi \cos^2\alpha}, \tag{29}$$

with χ obtained from the energy components at $b = 0$, cf. (23). In obtaining (29) non-relativistic kinematics was used and momentum distribution in the vicinity of midrapidity was approximated in a gaussian form. The maximum value of F from (29) as a function of α equals to $\chi/(2\sqrt{1+\chi})$. For protons from 400 MeV/nucleon collisions this is 0.22 (using energy values from Fig. 9). However, the proton F in Fig. 14 reaches ~ 0.47 at intermediate impact parameters, indicating the importance of the weak discontinuity. Note that the spectator contributions would tend to lower F.

On taking spectator contributions into consideration, and on analyzing the behavior of the r.h.s. of Eq. (29) with χ, one finds that F provides a lower limit to the angle of inclination of the discontinuities within participant matter relative to the beam axis,

22

$$\alpha > \tan^{-1} F.$$

The calculations in Fig. 14, utilizing parameters for the stiff equation of state and free NN cross-sections, actually somewhat overestimate data. Thorough discussions of the dependence of observables characterizing the sideward deflection on the microscopic input parameters in simulations can be found in Refs. [63]. It follows from Fig. 14 that the highest multiplicity interval within the experiment [61] corresponds to $b \lesssim 2.5$ fm.

Either data or calculations may be analyzed in terms of a kinetic-energy tensor [64]. This tensor can be written in a relativistic form as

$$S^{ij} = \sum_\nu s^{ij}_\nu = \sum_\nu \frac{p^i_\nu p^j_\nu}{m_\nu + E_\nu} \tag{30}$$

where the sum is over particles from a collision. Experimentally, the mean elements of the particle tensors $\langle s^{ij} \rangle$, associated with the reaction plane, may be determined directly as outlined in [12], irrespective of the fluctuations of an estimated reaction-plane about the true plane.[2] The major axis of the mean particle-tensor points in a direction within the reaction plane, at an angle θ_f relative to the beam axis. This direction is intermediate between the direction of discontinuities within the participant matter and the direction of motion of the spectator matter. Eigenvalues associated with the axis pointing out of the reaction plane are identical with the mean energies $\langle E^y \rangle$. The minor axis within the reaction plane, denoted with symbol x', is generally at a considerable angle $\gtrsim 50°$ relative to the strong and weak discontinuities within the participant matter. As $b \to 0$ this axis becomes identical with the

---

[2]Following considerations such as in Ref. [65], optimal weights in a vector [56] for the estimation of the reaction-plane direction, $\mathbf{Q} = \sum_\nu w_\nu \mathbf{p}^\perp_\nu$, are $w_\nu \approx \langle p^x \rangle / \langle (p^\perp)^2 \rangle$, where averages refer to specific rapidities and particle types. A more general equation for the estimation of the azimuthal angle Φ of the reaction plane follows from the requirement $0 = \frac{\partial}{\partial \Phi} \sum_\nu ((p^\perp_\nu \cos(\phi_\nu - \Phi) - \langle p^x \rangle)^2 / \langle (p^x - \langle p^x \rangle)^2 \rangle + (p^\perp_\nu \sin(\phi_\nu - \Phi))^2 / \langle (p^y)^2 \rangle)$. The averages within the equations may be determined self-consistently in data analysis.

beam axis. Eigenvalue energies $\langle E^{x'} \rangle$ are generally less than $\langle E^y \rangle$, see Fig. 12. The ratios $\langle E^y \rangle / \langle E^{x'} \rangle$ increase with particle mass. These ratios maximize at $b = 0$ as a function of the impact parameter, where they coincide with $\langle E^\perp \rangle / 2 \langle E^\parallel \rangle$. Compared e.g. to the variation of the flow angle θ_f (see also Ref. [66]), the variation of the discussed energy ratios with b is, though, slow, cf. Fig. 12 and further Fig. 15.

Kinetic energy tensor, in its nonrelativistic form, was determined in the Au + Au reactions on an event-by-event basis in Ref. [67]. The mean ratio R_λ was calculated of matrix elements associated with the direction out of the estimated reaction plane and the direction within the plane, perpendicular to main axis, as a function of participant proton multiplicity. Fluctuations of the estimated reaction plane about the true reaction plane generally reduce the possible differences between matrix elements in question [56]. (If not for fluctuations, R_λ would have been identical with the energy ratio $\langle E^y \rangle / \langle E^{x'} \rangle$.) For the Au + Au reaction at 400 MeV/nucleon, the average azimuthal angle between the two planes has been assessed within the experiment, and given in Ref. [67] as function of proton multiplicity. This makes possible a practical comparison of present calculations with these data. Ratio of the eigenvalues from the tensor with matrix elements modified on account of the fluctuations,[3] is compared to the data [67] in Fig. 15. As in the case of Fig. 13 a general agreement is found, although, quantitatively the calculations overestimate somewhat the data. The lowering of the ratio R_λ at high multiplicities stems from an increase in fluctuations. With regard to the flow angle θ_f, the position of a maximum in the experimental event distribution in the angle [68], for the highest multiplicity bin, appears to be in a rough accord with the conclusion on the impact parameter range, reached by examining F.

Physical reason behind larger energy values out of the reaction plane in simulations, than in a direction within the reaction plane, such as in the case of Fig. 15, is the same

---

[3]The difference $(\langle s^{xx} \rangle - \langle s^{yy} \rangle)$ is reduced by a factor $\langle \cos 2\delta\Phi \rangle$ and the element $\langle s^{xz} \rangle$ is reduced by $\langle \cos \delta\Phi \rangle$, where $\delta\Phi$ is azimuthal angle between the estimated and the true reaction plane [56,60].

as behind the different energies at $b = 0$. The expansion of largely equilibrated matter in the direction of motion of shock fronts is delayed, compared to the direction out of the reaction plane, by the time necessary for the shock fronts to traverse the normal matter. As matter is already being decompressed by the expansion developing in directions parallel to the shock-front surface, the expansion in the direction of shock motion does not acquire same strength. The fact that data [67] (also [12,60]) show different energy values associated with different directions demonstrates that, indeed, the equilibration occurs within a part of the system separated out from the cold matter. With motion being generally supersonic at a high energy, the interfaces between the hot and cold matter *must have* the nature of shock fronts. The sideward flow stronger than anticipated on the basis of a rotation of the $b = 0$ pattern, indicates the presence of a weak discontinuity (for the $b = 0$ pattern an extrapolated energy ratio from finite-b data such as in Fig. 15 could be used).

For other beam energies than 400 MeV/nucleon, azimuthal deviations between the estimated and true reaction planes were not given in [67], and, correspondingly, the measured and calculated energy ratios of interest in the Au + Au reactions cannot be directly compared. Comparisons to the theory would have been eased if energies associated with the directions relative to the *true* reaction plane were established, as was discussed. Unless one deals with some artifact of a strong variation of the fluctuations with beam energy, a considerable discrepancy between data and calculations, with regard to the energy ratios, may be arising at low beam energies. Specifically, the experimental squeeze-out ratio R_λ [67] maximizes at 250 MeV/nucleon in central reactions and rapidly decreases from there on with a lowering of the beam energy. On the other hand the ratio of calculated energies $\langle E^y \rangle / \langle E^{x'} \rangle$ (which may be obtained directly from Fig. 8), maximizes at 150 MeV/nucleon and continues as significantly larger than 1 down to 50 MeV/nucleon.

V. PION PRODUCTION

It is generally believed that, in comparison to baryons, pions are rather insensitive to the collective motion, due to their low mass and corresponding high thermal speeds. First, briefly, the possible effects of a collective expansion on energies and spectra of particles with different mass are investigated by considering a situation of the instantaneous freeze-out in the c.m.[4] of a locally equilibrated system at a constant temperature.

A. Collective Expansion and Mass

With inclusion of particle statistics, phase-space distributions in a locally equilibrated system are of the form

$$f_X = \frac{1}{\exp\left[(u^\sigma p_\sigma - \mu_X)/T\right] \mp 1} = \sum_{n=1}^{\infty} (\pm 1)^{n+1} \exp\left[n(\mu_X - u^\sigma p_\sigma)/T\right], \tag{31}$$

where the upper signs refer to Bose and the lower to Fermi statistics, respectively, $u^\sigma = (\gamma, \gamma \mathbf{v})$, $\mathbf{v}$ is velocity, and μ_X is chemical potential. The limit of a classical statistics corresponds to a large $(m_X - \mu_X)/T$. In that case the first term in (31) dominates,

$$f_X \simeq \exp\left[(\mu_X - u^\sigma p_\sigma)/T\right]. \tag{32}$$

The corrections on account of statistics in (31) correspond to an addition (for bosons) or subtraction (for fermions) of classical components corresponding to lower temperatures. Of a primary concern below will be the classical limit.

Nonrelativistically, a mean particle kinetic energy for a locally equilibrated system may be represented, following (32), as consisting of thermal and collective components in the form

$$\langle E_X^{kin} \rangle = \langle E_X^{kin} \rangle_{v=0} + \langle E_X^{coll} \rangle = 3T/2 + m_X \langle v^2 \rangle / 2. \tag{33}$$

---

[4]More elaborate freeze-out conditions are e.g. discussed in [69].

The collective energy component rises proportionally to particle mass, provided that $\langle v^2 \rangle$ is the same for different particle species. A relativistic extension of this result may be obtained by expanding the relativistic mean particle energy in powers of a collective velocity $\mathbf{v}$,

$$\langle E_X^{kin} \rangle = \langle E_X^{kin} \rangle_{\mathbf{v}=0} + \langle E_X^{coll} \rangle \approx \langle E_X^{kin} \rangle_{\mathbf{v}=0} + (\langle E_X \rangle_{\mathbf{v}=0} + 2T) \langle v^2 \rangle / 2 + \cdots \tag{34}$$

The mean kinetic energy of particle with mass m in a *globally* thermalized system, shown for reference in Fig. 16, is $\langle E^{kin} \rangle_{\mathbf{v}=0} = 3T + m(K_1 - K_2)/K_2$, where K_ν is a modified Bessel function of the argument m/T. Relativistically, the thermal agitation increases the coefficient in the collective energy component, which is a mass in (33), by the kinetic thermal energy plus twice the temperature (i.e. at least by $7T/2$). That is a large increase for pions, and can be significant even for protons or deuterons, at temperatures of interest such as displayed in Fig. 4.

The relativistic enhancement of the collective effect with thermal agitation, suggests the possibility of a light-particle distribution that is concave up on account of relativity, when the collective motion is present, and a logarithm of the distribution is plotted vs energy. On the other hand, a distribution of collective velocities peaked at finite velocity values might generate a particle spectrum at low temperatures or for large particle mass, that is concave down. The particle momentum distribution is given by

$$\frac{d^3 N_X}{dp^3} = \frac{g_X}{(2\pi)^3} \int d\mathbf{r} \, f_X \tag{35}$$

and the slope of the distribution is

$$\frac{1}{T_{eff}} = -\frac{\partial}{\partial E_X} \log \left(\frac{d^3 N_X}{dp^3} \right) = \frac{1}{T} \left(\langle \gamma \rangle_{\mathbf{p}} - \frac{E_X}{p} \langle \gamma \mathbf{n} \cdot \mathbf{v} \rangle_{\mathbf{p}} \right), \tag{36}$$

where $\mathbf{n}$ is a unit vector in the direction of $\mathbf{p}$ and

$$\langle \cdot \rangle_{\mathbf{p}} = \int d\mathbf{r} f_X \, (\cdot) \bigg/ \int d\mathbf{r} f_X \, . \tag{37}$$

The slope at $p = 0$ becomes

$$\frac{1}{T_{eff}} = \frac{1}{T}\left(\langle\gamma\rangle_{p=0} - \frac{m_X}{T}\langle(\gamma\mathbf{n}\cdot\mathbf{v})^2\rangle_{p=0}\right)$$
$$\approx \frac{1}{T}\left(1 + \frac{\langle v^2\rangle_{p=0}}{2} - \frac{m_X\langle(\mathbf{n}\cdot\mathbf{v})^2\rangle_{p=0}}{T}\right), \tag{38}$$

where the approximation leading to the last expression is for low v. Note that the slope (38) may be negative, which corresponds to a situation when the spectrum has a maximum at a finite p. For a high momentum p, the dominant contribution to the integrals in (37) would come from a velocity directed along $\mathbf{p}$ to an extent possible given a velocity distribution, on account of the strong dependence of (32) on $\mathbf{v}$ for large p, of a magnitude $v_m < p/E_X$ assuming a rapidly falling velocity-distribution. The slope may be then estimated as

$$\frac{1}{T_{eff}} \approx \frac{\gamma_m}{T}\left(1 - \frac{v_m E_x}{p}\right)$$
$$\approx \frac{1}{T}\sqrt{\frac{1-v_m}{1+v_m}} \approx \frac{1}{T}\left(1 - v_m + \frac{v_m^2}{2}\right) \tag{39}$$

where the second approximation is for $E_X \sim p$ and the last approximation is for small v_m. If (38) is larger than (39) then the the spectrum following from (32) is necessarily concave up within a certain range of energies; if (39) is larger then the spectrum is concave down (see also [69]). For example, if collective expansion has a cylindrical symmetry and collective speeds are sharply concentrated around a single value v, then the condition for the spectrum at 90° with respect to the symmetry axis to be concave down becomes

$$m_X > \frac{2T}{\gamma v}. \tag{40}$$

Clearly, we may have a situation when a heavy-particle spectrum is concave down, while a light-particle spectrum is concave up. For a spherically symmetric expansion, the factor of 2 on the r.h.s. of (40) gets replaced by 3. Explicit form of a distribution for a cylindrically symmetric expansion with a single value of v is (see also [69])

$$\frac{d^3 N_X}{dp^3} = \mathcal{N}\exp\left(-\frac{\gamma E_x}{T}\right)I_0\left(\frac{\gamma p v \sin\theta}{T}\right), \tag{41}$$

where $\mathcal{N}$ is a norm, I_0 - a modified Bessel function, and θ - an angle relative to the symmetry axis. For a spherically symmetric expansion with a single value of v, the distribution in momentum is

$$\frac{d^3N_X}{dp^3} = \mathcal{N} \exp\left(-\frac{\gamma E_X}{T}\right) \sinh\left(\frac{\gamma p v}{T}\right) \bigg/ \left(\frac{\gamma p v}{T}\right). \tag{42}$$

If a chemical potential μ_X is uniform throughout a volume V, then the normalization constant in (41) and (42) is $\mathcal{N} = g_X V \exp(\mu_X/T)/(2\pi)^3$. For smooth distributions of collective velocities, the sufficiently heavy particles (and in principle also possibly the sufficiently energetic) probe directly the collective velocity distribution

$$\begin{aligned}
\frac{d^3N_X}{dp^3} &= \frac{g_X}{(2\pi)^3} \int d\mathbf{r}\, f_X \\
&\approx \frac{g_X}{(2\pi)^3} \int d\mathbf{r}\, \exp\left[\frac{\mu_X - m}{T}\right] \exp\left[-\frac{E_X^4}{m_X^3 T}\left(\mathbf{v}(\mathbf{r}) - \frac{\mathbf{p}}{E_X}\right)^2\right] \\
&\approx \frac{1}{\gamma^6}\left(\frac{T}{\pi m_X}\right)^{3/2} \frac{g_X}{(2\pi)^3} \int d\mathbf{r}\, \exp\left[\frac{\mu_X - m}{T}\right] \delta\left(\frac{\mathbf{p}}{E_X} - \mathbf{v}(\mathbf{r})\right),
\end{aligned} \tag{43}$$

where the argument in the exponential in f_X was expanded around the maximum, as a function of $\mathbf{v}$, and it was assumed that the velocity distribution, nominally defined as

$$\begin{aligned}
\frac{\partial^3 \mathcal{P}_X}{\partial v^3} &= \int d\mathbf{r} d\mathbf{p}\, f_X\, \delta(\mathbf{v} - \mathbf{v}(\mathbf{r})) \bigg/ \int d\mathbf{r} d\mathbf{p}\, f_X \\
&= \gamma \mathcal{N}' \int d\mathbf{r}\, \exp\left[\frac{\mu_X - m}{T}\right] \delta(\mathbf{v} - \mathbf{v}(\mathbf{r})),
\end{aligned} \tag{44}$$

changes slowly over the range in v of a magnitude $\gamma^{-2}(T/m)^{1/2}$.

Besides collective motion, the spectra of different particles may be affected, at low momenta, by resonance decays and statistical effects. Following (31), corrections for statistics in the case of Eqs. (41) and (42) amount to adding or subtracting from the r.h.s. terms corresponding to lower temperatures. In order to assess a relative importance of different effects, it will be necessary to understand the dynamics of production. With pions not present in the initial state, an important pion observable that may be affected by collective expansion, besides spectra, is multiplicity.

B. Dynamics of Production

Production of pions in central La + La reactions at 800 MeV/nucleon will be considered. At different values of beam energy, pion multiplicities have been measured in La + La

reactions [9]. At 800 MeV/nucleon, both pion and proton spectra were determined at c.m. 90° in the very central reactions [70]. Using information in [70], these spectra may be conveniently normalized for comparisons with calculations.

Figure 17 shows the evolution of baryon-density profiles, along and perpendicular to the beam axis, in the La + La reaction at $b = 0$. The system goes through similar stages as Au + Au in Fig. 3. Figure 18 shows further baryon density at the center of the La + La system, net participant collective energy per nucleon calculated as in Eq. (21), and total entropy as functions of time. The collective energy saturates at about 76 MeV/nucleon, out of which ~ 56 MeV/nucleon is associated with transverse directions and ~ 20 MeV/nucleon with longitudinal. The difference in the energy per degree of freedom for different directions is not as large as in the 400 MeV/nucleon Au + Au reaction due to a smaller system size, combined with a larger Lorentz contraction and a reduced stopping at the higher beam energy.

One deficiency of the present model is that composites produced during the expansion do not participate in pion absorption and production, while in reality they would. To remedy this, some details relevant to pion production, such as variation with time of particle collision-rates and Δ decay rates in Fig. 19, are presented for a calculation with production of composites switched off. However, final pion spectra are given for a calculation with composite production switched on, as composites raise the freeze-out temperature, reducing to a certain degree the slopes of spectra. The final pion multiplicity does not depend in practise on composites as will become apparent later.

In Fig. 19 it is seen that the rise of Δ-decay rate is somewhat delayed relative to the rise of Δ-production rate in NN collisions. This is due to a finite Δ lifetime (see also [73]). The rise of the resonance formation rate in Nπ interactions follows very closely the rise of Δ decays, on account of a sizeable average Nπ cross section. With the exception of the Δ-production rate in NN interactions, that maximizes earlier, all rates maximize at $t \sim 13.5$ fm/c, when the shock waves in lanthanum nuclei reach the vacuum, see Fig. 17, and the system as a whole becomes excited and compressed. A later decrease of rates in Fig. 17 is associated

30

with expansion.

As pions (within the model) can only originate from nucleon-resonance decays, and pions can only be absorbed into nucleon resonances, the final pion number is equal to the difference in the total number of resonance decays and the number of resonance formations in πN interactions, i.e. the difference in areas under the curves in the bottom panel of Fig. 19. (The N^*'s of which the number at 800 MeV/nucleon at any one time never exceeds 4% of the total number of resonances, may be ignored in this discussion.) The rather small difference between the rates compared to the rates themselves at most times suggests a good kinetic equilibrium of pions and deltas with nucleons during the reaction. As, clearly, the number of deltas contributing a final pion is identical with the net number of deltas produced in nucleon interactions, the final pion number further coincides with the difference in areas under the curves in the center panel of Fig. 19. If one considers a chain starting with a delta production in an NN interaction followed by a delta decay with pion emission, followed by an absorption of this pion into a delta and so on, then such a chain terminates either with a pion in the final state, or with a delta absorbed in an interaction with a nucleon. The average number of pion absorptions within any such chain is equal to the ratio of an area under the dashed line in the bottom panel in Fig. 19, to an area under the solid line in the center panel, i.e. ~ 1.5. If only chains terminating with a final pion are considered, then the number of absorptions is found to exceed 2 in the simulation. One can say that a pion in the final state of the system has been, on the average, absorbed more than twice and reemitted before reaching the vacuum (see also recent papers [71,72]).

Pion multiplicity measured in central collisions is lower by nearly a factor of 2 than anticipated in the fireball model which assumes a complete global equilibration [9]. A naive expectation might be that within the reaction the time is too short to allow for a production of the number of pions and deltas expected in a global equilibrium. (The deltas left out towards the end of reaction would contribute to a final pion number.) Figure 20 shows the pion and delta number divided by total nucleon number, as a function of time in the La + La reaction at 800 MeV/nucleon. The number reaches a maximum right after the whole matter

has entered the hot compressed region. The ratio of the global-equilibrium number of pions and deltas to baryon number at this time, $t \sim 14$ fm/c, is indicated by the upper of two horizontal dashed lines in Fig. 20. The ratio is obtained using the equilibrium densities

$$\rho_\pi = 3 \int \frac{d\mathbf{p}}{(2\pi)^3} \frac{1}{\exp(E_\pi/T) - 1}, \qquad \rho_N = 4 \int \frac{d\mathbf{p}}{(2\pi)^3} \frac{1}{\exp((E_N - \mu_N)/T) + 1},$$

$$\rho_\Delta = 16 \int \frac{d\mathbf{p}}{(2\pi)^3} \int \frac{dm}{2\pi} \mathcal{A}_\Delta \frac{1}{\exp((E_\Delta - \mu_N)/T) + 1}, \tag{45}$$

where temperature and chemical potential are adjusted to reproduce the representative baryon density, $\rho = 2.25\rho_0$ at a respective time (cf. Fig. 17), and the energy per nucleon from simulation, excluding potential energy, of 1133 MeV/nucleon. (Isospin asymmetry is ignored for simplicity.) The equilibrium value, indicated by the upper dashed line in Fig. 20, is not reached, what appears to support an expectation that the time is too short to produce an adequate number of pions and deltas. In fact, as the system expands and baryon density drops, the global equilibrium value increases more and likewise the apparent deficit of pions and deltas. Towards the freeze-out, however, the number of pions and deltas behaves in an unexpected manner. Instead of straining towards the equilibrium value and settling once interactions stop, this number declines. The decline is seen in many other microscopic calculations of collisions, e.g. in [66,73–75]. (Incidentally, if a ratio of pion and delta density to baryon density is investigated locally, then the decline becomes even more pronounced; the total number represents the system as a whole with different parts going through different stages.) The rise and decline in the number of pions and deltas could be understood if somehow the number of pions and deltas were first below and later above the equilibrium number. The clue to an understanding of this situation is in collective motion ignored till now.

Collective motion within the system takes away energy available locally for particle production. Right after the whole matter in the La + La reaction has entered the hot region, at $t \sim 14$ fm/c, the collective energy within this system, as seen in Fig. 18,

32

is ~ 30 MeV/nucleon. If this energy is subtracted from the available energy and Eqs. (45) are used as before, then the equilibrium value for the ratio of pions and deltas to baryons is obtained which is indicated by the lower of two horizontal dashed lines in Fig. 20. It is apparent in this figure that the system approximately reaches an equilibrium with regard to the pion and delta number given the particular value of collective energy. As the system expands, though, more and more energy turns into collective. In Fig. 21 it is seen that if expansion were isentropic then the number of pions and deltas should decrease. (At low temperature, in an isentropic expansion the pion-to-baryon ratio behaves as $\rho_\pi/\rho \propto \exp(-m_\pi \rho_1^{2/3}/T_1 \rho^{2/3})$.) In Fig. 21, the state of the system at $t = 14$ fm/c is crudely (as in fact different parts of the system go through different stages) represented with crosses. To assess the situation further, the equilibrium number of pions and deltas is calculated at different times by evaluating the equilibrium density of particles throughout the space in local frames, given energy per baryon and baryon density in such a frame, and integrating the particle density over whole space. Results are represented with dots in Fig. 20. The obtained local-equilibrium number of pions and deltas is seen to increase when the mass of hot matter increases, and to decrease rapidly afterwards. The actual number of the particles closely follows the equilibrium number during compression. The local-equilibrium number crosses the actual number of pions and deltas at about the maximum of the latter number (as should be expected). While the number of pions and deltas decreases during the expansion, it freezes out, nonetheless, at a relatively high value. This is because a decrease of nucleon density in expansion effectively shuts off the processes $N + N \leftrightarrow N + \Delta$, see Fig. 19. The processes of pion absorption, with a larger cross section, and the Δ decays continue somewhat longer, preserving the thermal but not the chemical equilibrium of the pionic sector with nucleons. Portion of the chemical equilibrium path, with nonadiabaticity taken into account, is sketched with dashed lines in Fig. 21. At a freeze-out, at a density $\rho \sim 0.5 \rho_0$, the ratio of pions and deltas to baryons is larger by $\sim (1.4 - 1.8)$ than in the state of chemical equilibrium.

It has been conjectured in the past [9] that pion multiplicity in the central collisions is

low, because part of the energy in the center of mass is used up in compressing matter, and, correspondingly, is not available for production. Present results show that the role of energy not available for production within a heavy system is played by the collective energy. In fact, potential energy at the time when pion and delta number maximizes in the La + La reaction simulation, differs from the potential energy in a ground state by a mere 3 MeV/nucleon. (Momentum-dependent interactions might, though, have an effect on pion number.) With regard to another expectation, that the time in a reaction is too short for producing an equilibrium number of pions and deltas, it is seen that the number of pions and deltas actually freezes out not below, but above an equilibrium value.

C. Features of Single-Particle Observables

The left panel in Fig. 22 shows calculated momentum distributions of different particles (filled symbols) within a c.m. polar-angle range of 60-120° in the 800 MeV/nucleon La + La reaction at $b = 1$ fm, together with momentum distributions of protons and negative pions in the very central reactions deduced from experimental results of Ref. [70] (open symbols). The cross section for central reactions investigated in Ref. [70], needed for the normalization of distributions was estimated at 86 mb, using the integrated π^- yield stated in [70] and π multiplicities from Ref. [9]. The experimental π^- distribution agrees very well with the calculated distribution at all energies, and the proton distribution – up to an energy of ~ 450 MeV in the c.m.s. The pion distributions may be well approximated with straight lines (in the logarithmic plot), while baryon distributions are concave down. The slopes significantly decrease with increasing particle mass. If the calculated slopes were to be interpreted in terms of temperature, quite disparate values would be obtained, of 70, ~ 110, ~ 145, and ~ 175 MeV, for pions, protons, deuterons, and helions, respectively.

For the sake of understanding the momentum distributions from simulations, the left panel in Fig. 22, shows additionally baryon and neutral-pion distributions from an instantaneous freeze-out model (solid lines). In the case of an expansion with a single value of

34

velocity, the asymptotic collective energy in Fig. 18 would correspond to $v \approx 0.41c$. In the case of a uniform velocity distribution, adopted within the model for the display in Fig. 22, the collective energy corresponds to a cut-off velocity-value of $v_c \approx 0.51c$. The mean proton energy at a freeze-out of 196 MeV from simulation, corresponds then to a local temperature of $T \approx 55$ MeV. The baryon momentum distributions within the model take the form

$$\frac{d^3 N_X}{dp^3} = \frac{g_X V}{(2\pi)^3} \exp\left(\frac{\mu_X}{T}\right) \frac{3}{v_c^3} \int_0^{v_c} dv\, v^2 \exp\left(-\frac{\gamma E_X}{T}\right) \sinh\left(\frac{\gamma p v}{T}\right) \Big/ \left(\frac{\gamma p v}{T}\right), \qquad (46)$$

cf. (42). For pions the distribution is (see also [76,77])

$$\begin{aligned}
\frac{d^3 N_{\pi^0}}{dp_\pi^3} = \frac{V}{(2\pi)^3} \exp\left(\frac{\mu_{\pi^0}}{T}\right) \frac{3}{v_c^3} \int_0^{v_c} dv\, v^2 &\bigg\{ \exp\left(-\frac{\gamma E_\pi}{T}\right) \sinh\left(\frac{\gamma p_\pi v}{T}\right) \Big/ \left(\frac{\gamma p_\pi v}{T}\right) \\
&+ \exp\left(\frac{\mu_{\pi^0} - 2\gamma E_\pi}{T}\right) \sinh\left(\frac{2\gamma p_\pi v}{T}\right) \Big/ \left(\frac{2\gamma p_\pi v}{T}\right) \\
&+ \frac{16}{3} \exp\left(\frac{\mu_N}{T}\right) \frac{1}{2p_\pi E_\pi} \int \frac{dm}{2\pi} \mathcal{A}_\Delta \frac{m}{p_\pi^*} \\
&\times \int_{p_{\Delta 1}}^{p_{\Delta 2}} dp_\Delta\, p_\Delta \exp\left(-\frac{\gamma E_\Delta}{T}\right) \sinh\left(\frac{\gamma p_\Delta v}{T}\right) \Big/ \left(\frac{\gamma p_\Delta v}{T}\right) \bigg\}
\end{aligned} \qquad (47)$$

where the second and third term inside braces account, respectively, for the effects of Bose statistics in lowest order, and for the decays of Δ resonances left-out at a freeze-out. The minimum and maximum momenta of a Δ whose decay might yield a pion with a momentum p_π, are $(p_\Delta)_{1,2} = (m/m_\pi^2)|E_\pi^* p_\pi \mp E_\pi p_\pi^*|$. The subscript '*' indicates pion momentum and energy in a Δ-frame. Pions and deltas are assumed to be in a thermal but not in a chemical equilibrium with the rest of the system; the chosen value of a freeze-out density is $\rho = 0.6\rho_0$.

It is quite apparent in Fig. 22 that the instantaneous freeze-out model (with parameters taken from dynamics) describes, in a semi-quantitative manner, the shapes of spectra from simulations. The spectra of the lightest particles, pions and protons, with largest thermal dispersion of velocities, are, in fact, equally well described within a model with a single collective expansion velocity. Proton mass (and cluster masses) satisfies $m > 3T/\gamma v$ and the spectrum is concave down. For pion mass the opposite inequality is true. Long- and short-dashed lines in Fig. 22 show, respectively, contributions from free pions and from Δ decays within the instantaneous freeze-out model. The free-pion contribution is concave up, but in the overall distribution this concavity is partially filled up with pions from decays. Despite

the spread of the Δ resonance in mass, a major resonance contribution comes here (and at other temperatures of interest) from masses in the vicinity of resonance peak; the ratio of resonances to pions is $\rho_\Delta/\rho_\pi \propto \rho_N \exp(-(m_\Delta - m_N - m_\pi)/T)/T^{3/2}$.

Of a general interest is the degree of Bose enhancement or the proximity to a condensation for low-momentum pions. The excessive number of neutral pions at a freeze-out corresponds to a finite chemical potential $\mu_{\pi^0} \sim T\log(N_{\pi^0}/N_{\pi^0}^{eq}) \sim 25$ MeV. For negative pions, the isospin asymmetry within the system corresponds to an additional enhancement of the potential for negative pions, and a depletion for positive pions, $\mu_{\pi^-} - \mu_{\pi^0} = \mu_{\pi^0} - \mu_{\pi^+} \sim T\log(N/Z) \sim 20$ MeV. Overall, the potential at a freeze-out for negative pions may be as large as ~ 45 MeV, corresponding to a low-momentum enhancement of $\exp((\mu_{\pi^-} - m_{\pi^-})/T) \sim 18\%$. Possible enhancement for neutral pions is 13%. Beyond that, the Coulomb field in the final state enhances distribution of negative pions at low momentum and depletes that of positive pions and other particles. Lower limit on the magnitude of the effect on single-charged low-momentum particles follows from the formula obtained under an assumption of a dominating collective motion, 0.7 MeV·fm $\rho^{1/3} Z/A^{1/3} \langle E^{kin} \rangle \sim 5\%$, where Z and A are total charge and mass numbers, respectively, $\langle E^{kin} \rangle$ is mean kinetic energy of particle species in question, and ρ is freeze-out density. Inspection of spectra reveals that the actual effect of the Coulomb field in the La + La reaction is of the order of 30%.

Collective motion is generally characterized by a correlation between particle spatial positions and their momenta. In order to demonstrate explicitly that strong features in the calculated distributions, particularly slope-differences between different particle species, are associated with the collective expansion, calculations are further repeated with an interchange of particle positions during evolution. Interchanges are made within same species, when collisions are still frequent. (Particle momenta are not altered.) The procedure leaves density in configuration space and momentum distributions intact. Correspondingly, kinetic and potential energies stay the same. However, correlations between particle momenta and positions get destroyed. The final momentum distributions from calculations with the position interchange are shown in the right panel of Fig. 22. Straight parallel lines are drawn

to guide the eye. The distributions from the calculations turn out largely exponential with nearly the same slopes (some collective motion still develops due to the collisions, cf. Fig. 18). There is enough time within a reaction for a complete thermalization.

Figure 23 shows measured pion multiplicities in central symmetric reactions as a function of beam energy [9], together with multiplicities from standard calculations of central La + La reactions (solid line) and from calculations with positions interchanged (dashed line). The standard calculations, with the collective motion developed during evolution, describe reasonably the data. The calculations with the position interchange and the collective motion extinguished, on the other hand, lead to multiplicities larger by nearly a factor of 2 (essentially such as expected within the fireball model), in a dramatic disagreement with data.

Despite of the fact that the measured pion multiplicities point strongly towards the collective motion, in order to better assess this motion, it would be clearly highly desirable to have *normalized pion and proton* momentum distributions from central collisions of heavy nuclei, extending over a wider kinetic-energy range than in Fig. 22, possibly together with cluster distributions. Heavy systems are preferred over light systems [4]. In peripheral collisions of light systems, differences between pion and proton spectra may exceed differences arising from collective-energy considerations, on account of energy conservation in elementary collisions, with kinetic energy depleted due to the production of pions. In principle, with a decrease of impact parameters, the relative importance of conservation in individual collisions would decrease, while the importance of collective motion should increase. To test an interpretation in terms of collective energy, features of the cluster distributions could be examined [78]. In lightest systems, though, such an interpretation would be always hampered by the lack of a complete stopping even in most central collisions, at beam energies at which pions are abundant.

The actual distribution of collective velocities for baryons in the vicinity of last collisions from the simulation of the 800 MeV/nucleon La + La reaction is shown in Fig. 24. This distribution is not peaked at any large value of velocity (although $v^2(d^3\mathcal{P}/dv^3)$ is peaked,

however broadly, in the vicinity of $v \sim 0.4c$). Tests indicate that the high-velocity tail is associated with low temperatures. High temperatures, on the other hand, are particularly associated with the low-velocity portion of the distribution. Parametrization of particle spectra, such as from experiment, in terms of a single freeze-out temperature for any particle, will be always approximate. Also an approximation can generally arise from the use of same temperature and same velocity for different particles, as e.g. pions may be emitted earlier when temperatures are slightly higher and the collective energy lower, than when light baryons are emitted, and differences generally develop in the emission of different baryons, cf. Sec. VI. In any case, though, the use of a uniform distribution in collective velocity in parametrizing particle distributions would be more sensible than the use of a single velocity value. One possibility within an experiment is the use of a velocity distribution deduced from heavier fragments, of which distributions should approach that of the collective velocity, with increasing fragment mass, cf. Eq. (43). The use of a single velocity value and of a temperature treated as adjustable parameters in describing measured spectra of different particles, on the other hand, is expected to give absurd results. Reasonable temperatures would lead to excessively sharply-peaked distributions of heavy fragments. To make the fits acceptable, temperature parameters would then need to be raised making it appear that heavier fragments came from hotter regions than light fragments.

D. System Measured by Brockmann et al.

Before moving on to other issues, let me discuss data [5], that first stirred up interest in shapes of transverse spectra of pions from central reactions, from the Ar + KCl system at 1.8 GeV/nucleon, and further aspects of transport models. In [5] experimenters attempted to fit their data with a single exponential and concluded that this was not possible. Moreover, they compared results to those from a cascade model [73]. Due to the low mass of the system and high beam energy, and corresponding lack of stopping, the spectra from transport simulations are quite sensitive to the assumptions on elementary collisions; the experimenters

chose a cross section for $N + N \rightarrow N + \Delta$ processes that was exceedingly forward-peaked. Cascade results were not laid over data, but rather fitted with an exponential. The conclusion was that the cascade model cannot explain the *high*-momentum portion of a pion spectrum.

The data from [5] are shown in two panels of Fig. 25 (open circles). Insets show an asymmetry coefficient a obtained by fitting the double-differential distribution

$$\frac{d^2 N_{\pi^-}}{dE \, d\cos\theta} \propto (1 + a(E)\cos^2\theta). \tag{48}$$

The right panel shows further results from the cascade model [73] following assumptions in [5] (squares). It is seen that, indeed, the high-momentum tail of the measured pion distribution is underpredicted. Further, the asymmetry coefficient from the model is far too high at high pion kinetic energies. Discrepancy in this coefficient reveals part of the problem with the high-momentum tail. The left panel of Fig. 25 displays, in addition to data [5], results from the present model [35] with an angular dependence of the delta-production cross-section that was fitted to elementary data in Ref. [44] (filled circles). The model describes well the high-momentum tail of the pion spectrum, and it describes much better the asymmetry coefficient than the cascade model. This is associated both with the shape of elementary delta-production cross-section in the model and with respecting of the time-reversal invariance in absorption cross-sections (cf. Sec. II; high-energy pions are excessively absorbed in the original cascade model compared to the low-energy pions). For illustrative purposes (the involved assumption is too extreme), calculations were repeated within a version of the cascade model where Δ-production cross-section was isotropic; the results are shown in the right panel of Fig. 25 (diamonds). The description of the high-momentum tail and asymmetry coefficient is improved over the first cascade calculation.

Overlaying the calculations and data reveals a puzzle concerning the *low*-momentum part of pion spectrum. Already the cascade model underpredicts data [5] in this region and correcting the pion absorption cross-section, cf. Eq. (8) and associated text, increases discrepancy. Measured spectrum appears to have a low-momentum peak as though superimposed onto the spectrum such as from the calculation, of a similar height as the latter, see

left panel in Fig. 25, apparently pointing towards physics outside of the transport model. [5]

E. Shadowing

As impact parameter is increased in symmetric collisions at high beam energies, regions with spectator matter develop and grow in size. In strongly asymmetric systems, such as investigated in [80], the spectator matter is always present. The matter can shadow pions emitted from the hot participant region.

In Fig. 13 with mean momentum-components within the reaction plane of particles emitted from 1 GeV/nucleon Au + Au reactions, it is seen that, at low impact parameters $\sim$ 3 fm, pions moving forward and backward in the c.m.s. have momentum components of same sign as baryons. As the pion angular-distribution is forward-backward peaked at $b = 0$, cf. Fig. 7, the average deflection such as for baryons, within the reaction plane, must be associated with the weak discontinuity. The pion momentum components per mass are considerably lower than the baryon components, see Fig. 13, and pion velocity components even more so, by a factor of $\sim$ 5 in the forward and backward rapidity regions, than the baryon components. At higher impact parameters ($\sim$ 7 fm) in the reaction, pions have momentum components of an opposite sign than baryons, cf. Fig. 13. These components increase more than twofold if analysis is limited to pions emitted early, within the first 16 fm/c of the reaction. (The latter pions constitute about 1/3 of all.)

When pion emission is examined at a 90° c.m. polar-angle, it is found essentially isotropic in the azimuthal angle at low impact parameters such as $b \sim$ 3 fm. However, at higher

------

[5] Elsewhere, though, results well exceeding data in the low-momentum region were obtained [79], supposedly on the account of the nuclear mean field and Pauli principle. Here, little effect of these factors on spectra is found (as is apparent in Fig. 25) in accordance with the intuition, given the small system size, the high beam energy, and the momentum region. No attempts are made here to interpret unnormalized data in literature.

impact parameters, such as $b \sim 7$ fm, this emission is found peaked at 90° with respect to the reaction plane. The peaking is enhanced when analysis is limited to pions with high c.m. momenta, $p > 200$ MeV/c, see Fig. 26 ($\Theta = 0°$). The latter peaking was observed experimentally in events corresponding to intermediate impact parameters [81,82].

Figure 27 displays contour plots of baryon density (solid lines) within the reaction plane, in the 1 GeV/nucleon Au + Au reaction at $b = 7$ fm, at a time $t = 15$ fm/c. At the impact parameter equal to the half of the maximum possible value, the spectator regions are well developed. The spectator matter begins to detach from participant matter at the time at which the densities are displayed. Shocks have started out in the particular reaction at an angle of inclination relative to the beam axis of $\sim 65°$, cf. Eq. (25), and have rotated down to lower angles $\sim 55°$, compare Fig. 11. The last of what has become the participant matter has dived into the shocked region at a time $t \sim 10$ fm/c.

Figure 27 displays further contour plots of pion and delta density within the reaction plane. It is apparent in that figure that the spectator matter limits pion emission. An analysis of the emission in different directions, within the simulation, shows that the transmission coefficient for pions through the center of spectator matter does not exceed 5% during the first 16 fm/c of the evolution. With not very strong sideward-flow effects exhibited by pions in the absence or near absence of spectator matter at low impact parameters (at this and at other beam energies), the evidently strong shadowing at the higher impact parameters must generate sizeable average momenta per mass opposite, due to geometry, to the momenta of nucleons.

Early proton emission is affected by shadowing, too. In the proton case, though, the shadowing does not lead to such dramatic effects as in the pion case, because baryons exhibit generally stronger dynamic effects and because baryon emission is overall somewhat delayed relative to pion emission. Thus, the mean momenta within the reaction plane of protons decoupling from the 1 GeV/nucleon $b = 7$ fm Au + Au, within the first 16 fm/c, are nearly zero. These protons constitute a smaller fraction of particles emitted at all times than pions (about 10% as compared to 1/3 for pions; pions get ahead of the bulk of the matter on

account of larger thermal velocities).

While the effect of shadowing on the mean momenta is opposite to that of dynamics, both type of effects act to suppress the emission within the reaction plane at midrapidity as compared to the emission out of the reaction plane. Figure 26 with calculational results illustrates the fact that the issue as to which of the above two effects dominates in generating an azimuthal pattern at midrapidity, may be resolved at a qualitative level within an experiment. Thus, one needs to examine an emission pattern within a plane $p^{z'} = 0$ where axis $p^{z'}$ points at an angle Θ measured counterclockwise within the p^x-p^z plane, from the beam. When shadowing dominates, an azimuthal anisotropy should persist or increase compared to that at $\Theta = 0$ (within a plane perpendicular to the beam), when axis $p^{z'}$ is rotated to negative Θ-values, making the plane of analysis more aligned with spectator pieces when latter are close to the participant matter, at a time when many particles are emitted, cf. Figs. 27 and 2. On the other hand, an anisotropy solely due to shadowing should decrease or disappear when axis $p^{z'}$ is rotated to positive Θ-angles (case of pions in Fig. 26). When anisotropy is primarily associated with a stronger collective motion in the directions parallel to shock-front surfaces, in particular in the direction out-of-the-reaction-plane, in comparison to the direction perpendicular to shock surfaces, then the anisotropy within the plane $p^{z'} = 0$ should increase when axis $p^{z'}$ is rotated to positive Θ-angles (case of protons in Fig. 26 and baryons in Refs. [13,67]).

With regard to the transverse-momentum dependence of azimuthal anisotropies [81,82], any anisotropy must disappear when $p^{\perp} \rightarrow 0$ (but see [71]), provided that particle momentum distribution, denoted below as

$$\mathcal{N}(\mathbf{p}^{\perp}) \equiv \frac{d^3 N_X}{dp^3}(\mathbf{p}^{\perp}, p^z),$$

is smooth at $p^{\perp} = 0$. Expansion of the distribution up to the second order in transverse momenta yields

$$\mathcal{N}(\mathbf{p}^{\perp}) \simeq \mathcal{N}(0) + \frac{1}{2}\left[\left.\frac{\partial^2 \mathcal{N}}{\partial p^{x2}}\right|_{p^{\perp}=0} + \left.\frac{\partial^2 \mathcal{N}}{\partial p^{y2}}\right|_{p^{\perp}=0}\right] p^{\perp 2} + \left.\frac{\partial \mathcal{N}}{\partial p^x}\right|_{p^{\perp}=0} p^{\perp} \cos\phi$$

42

$$+\frac{1}{2}\left[\frac{\partial^2 \mathcal{N}}{\partial p^{x2}}\bigg|_{p^\perp=0} - \frac{\partial^2 \mathcal{N}}{\partial p^{y2}}\bigg|_{p^\perp=0}\right] p^{\perp 2}\cos 2\phi, \tag{49}$$

where ϕ is azimuthal angle relative to the reaction plane and x and y denote directions perpendicular to the beam axis in– and out–of–the–reaction–plane, respectively. The coefficient in front of $\cos\phi$ vanishes at midrapidity in a symmetric system. The coefficient in front of $\cos 2\phi$ is proportional to momentum squared. (These features of the coefficients would be retained if third axis were rotated away from the beam.) The azimuthal asymmetry at midrapidity may be e.g. quantified with a ratio of out-of-plane to in-plane momentum distribution minus 1. This quantity is proportional to the coefficient in front of $\cos 2\phi$ in Eq. (49) and, correspondingly, vanishes quadratically with momentum as $p^\perp \to 0$. (That is also true for other measures of asymmetry such as $\langle\cos 2\phi\rangle$.) In the case of pions the asymmetry would grow with an increase of pion velocity at midrapidity, as pions would move out to the sides in a reaction and encounter spectator matter in the vicinity of the reaction plane. At lower impact parameters, when layers of spectator matter are thin and semi-transparent to pions, some dependence of the asymmetry on pion momentum can be expected, related to the energy-dependence of pion-nucleon cross-sections. At high impact parameters in heavy systems, when layers of spectator matter are thick and intransparent to pions even for low pion-nucleon cross-sections, the asymmetry should saturate once pion velocities get close to c. When this paper was under completion, an extended study of pion shadowing by Li has appeared [83], with calculational results exhibiting these features. Data [81,82] are suggestive of the rise of asymmetry at high momenta, but corresponding errors are large. Other recent theoretic references on pion shadowing in symmetric systems are [71,84,85].

VI. BARYON OBSERVABLES

A. Entropy and Fragment Yields

Experimentally yields of different fragments are used to determine entropy produced in reactions. Specifically, at low densities when effects of statistics and interactions between fragments can be ignored, thermodynamic entropy per baryon can be expressed as

$$\frac{S_B}{A} = \sum_X \frac{M_X}{A} \left(\frac{5}{2} - \frac{\mu_X + B_X}{T}\right) \approx \frac{5}{2}\frac{M}{A} - \frac{Z}{A}\frac{\mu_p}{T} - \frac{N}{A}\frac{\mu_n}{T} \tag{50}$$

where M_X is multiplicity of fragment X, B_X (> 0) is fragment binding energy, and $\mu_X = Z_X \mu_p + N_X \mu_n$ is chemical potential. The approximation in (50) is for small binding energies per nucleon in comparison to nucleon chemical potentials μ_n and μ_p. The ratios of nucleon chemical potentials to temperature can be obtained from fragment yield ratios, thus e.g. $\mu_n/T = \log(g_p m_p^{3/2} M_d / g_d m_d^{3/2} M_p) = \log(M_d/3\sqrt{2}M_p)$, and $\mu_p/T = \log(\sqrt{2/3}M_h/M_d)$. High entropy values correspond to large negative values of μ_N/T and to a rapid drop of yield with fragment mass. In data analysis [20,19], theoretic models are used, such as QSM [86], to extend the relation (50) between entropy and fragment yields to situations when e.g. fragment phase-space overlap becomes of a concern.

Entropy per nucleon determined from measured yields of light fragments at large c.m. angles in the Au + Au reaction at 400 MeV/nucleon [20], is shown in the left panel of Fig. 28 as a function of reduced participant-proton multiplicity. The right panel of Fig. 28 shows entropy per nucleon associated with fragments emitted at large angles [35] (circles), determined from calculated fragment phase-space distributions, as a function of b. An agreement is found with regard to the value of entropy produced in the very central reactions and with regard to the general behavior of entropy with the reaction centrality at the particular beam energy; see further Ref. [35].

In order to understand the production of entropy in collisions it is convenient to consider first the case of $b = 0$. In that case, at high energies, most of the entropy is produced in

shock fronts, cf. Figs. 3 and 4. Further production takes place during expansion. The hydrodynamic Navier-Stokes equations yield for the rate of change of entropy per baryon with time [50]

$$\frac{\partial}{\partial t}\left(\frac{S}{A}\right) + \mathbf{v} \cdot \nabla \left(\frac{S}{A}\right) = \frac{1}{\rho T}\text{div}\,(\kappa \nabla T) + \frac{\eta}{2\rho T}\left(\frac{\partial v_i}{\partial r_k} + \frac{\partial v_k}{\partial r_i} - \frac{2}{3}\delta_{ik}\frac{\partial v_l}{\partial r_l}\right)^2, \qquad (51)$$

where κ is heat capacity coefficient and η is viscosity coefficient. In the classical limit, cf. e.g. [53], the coefficients are approximately given by $\kappa \approx (75\sqrt{\pi}/64\sigma_{NN})\sqrt{T/m}$ and $\eta \approx (5\sqrt{\pi}/16)\sqrt{mT}/\sigma_{NN}$. However limited, an insight into the entropy production during the expansion may be obtained by substituting into (51) results for velocity, density, and temperature from the simplified consideration in Sec. III B, involving assumptions of cylindrical symmetry, self-similar expansion, and ideal-gas equation of state. An examination of the r.h.s. of Eq. (51) shows that the heat conduction can cause a drop of local entropy with time when temperatures on the average decrease with moving away from a given point, whereas the viscosity always leads to a rise in the local entropy per particle. Substitution of the results from Sec. III B yields a net drop of entropy at the center of the system with time, quantitatively consistent with what is observed in Fig. 3; temperatures decrease in the surroundings due to the expansion into the vacuum. The substitution further yields a divergence of entropy production-rate towards the edges of density distribution; in the net entropy production-rate the viscous contribution is integrable while the conduction contribution is nonintegrable. If a cut-off density is adopted for the validity of hydrodynamics, then the net increase of entropy per nucleon on the account of heat conduction in expansion, may be estimated with the formula

$$\delta\left(\frac{S}{A}\right) \simeq \frac{3(\gamma - 1)^{1/2}}{\sigma_{NN}\,\rho(0,0)\,R(0)}\left(\frac{\rho(0,0)}{\rho_f}\right)^{\gamma/2}, \qquad (52)$$

cf. Eq. (17). The increase due to viscosity turns out to be given by a similar formula but with a numerical coefficient in front smaller by one order of magnitude. Rise of the entropy production-rate towards the edges of density distribution is quite consistent with what is observed in Fig. 3. The results indicate that most entropy in expansion at $b = 0$ is produced

45

within an interface between the hot matter and the vacuum and that the production is associated with the equalization of temperature. Quantitatively, Eq. (52) gives an increase of the entropy during an expansion in the 400 MeV/nucleon reaction by $\delta(S/A) \sim 1$, while the simulation yields $\delta(S/A) \sim 0.6$.

Some limitation of the above consideration becomes apparent when a *self-consistent* solution of the viscous hydrodynamic equations is confronted with simulations. While finding that the consistency in the solution moderates an increase of the entropy, Kapusta [87] obtained a near independence of the entropy generated in expansion on the mass of an expanding nuclear system, $\delta(S/A) \sim 0.3$ for $\rho_1 \sim 2\rho_0$. By contrast, in the simulations the generated entropy increases when A decreases, actually in nearly such a manner as predicted by Eq. (52), $\delta(S/A) \propto A^{-1/3}$. The increase appears, in fact, consistent with the central data for different systems [89,20].

Following (20) or more detailed considerations, generation of entropy during expansion in the considered $b = 0$ Au + Au reaction, increases *local* kinetic energy towards freeze-out by $\sim 50\%$, limiting the rise of collective energy. In principle, the dissipation could have been so strong that no collective energy would have been generated at all. Then, correspondingly, cluster yields would have been lower also. The correlation between cluster yields and collective motion is illustrated in Fig. 29 which shows the beam-energy dependence of yield ratios from standard calculations and from calculations with the collective motion extinguished by particle-position interchange, together with data [20]. The beam-energy dependence of the ratios of measured $A = 3$ cluster yields to proton yield is not well reproduced within the standard calculations; the quality of the description is about the same as within the QSM model [20]. Unambiguously, though, the data favor the results from the standard calculations with a significant collective motion developed, over the results from calculations with the motion extinguished.

Dissipation heating the edges of matter distribution and cooling off the center of a colliding system at $b = 0$ as in Fig. 3, beyond what actually can be seen there, together with some emission before equilibration, lead to quite a spread of entropy values per baryon

in the vicinity of particle emission points, cf. Fig. 30. As, generally, more clusters are emitted when entropy is low than when it is high, the average entropy in the vicinity of cluster emission-points may be expected lower than in the vicinity of nucleon emission-points. Specifically, if the distribution such as in Fig. 30 were approximated in a gaussian form $d\mathcal{P}/d(S/A) \sim \exp\left[-(S/A - \overline{S/A})^2/2\Delta^2(S/A)\right]$, and a complete equilibrium were assumed with $M_X/M_N \sim \exp\left[-(A_X - 1)(S/A)\right]$ for a given entropy, then the average entropy in the vicinity of emission points of baryons with different masses would be expected to decrease with a decrement per unit mass $\langle S/A \rangle_{A+1} - \langle S/A \rangle_A \lesssim -\Delta(S/A)/2$. In the 400 MeV/nucleon Au + Au reaction the dispersion is $\Delta(S/A) \sim 0.40$, and the expected decrement would then be $\langle S/A \rangle_{A+1} - \langle S/A \rangle_A \lesssim -0.20$. In the simulation, the entropy in the vicinity of last collision points is found to decrease by about 0.14 per mass unit for light baryons. With an increase of the beam energy, the entropy generated in expansion increases, just as does the entropy generated within shock fronts. Likewise, the dispersion of entropy values increases, and the mean entropy in the vicinity of emission points is found to decrease faster with baryon mass. E.g. in the 1 GeV/nucleon $b = 0$ Au + Au reaction-simulation the decrease is about 0.20 per mass unit. The entropy differences diminish, on the other hand, when the beam energy is lowered (though, they become then increasingly more difficult to assess reliably within the calculation).

In the analysis [19] of intermediate-mass fragment yields from central Au + Au reactions, in particular at 400 MeV/nucleon, a gradual decrease of entropy with charge was observed, however slower than in the present calculation. For heavy fragments the decrease might be moderated by size effects. In the analysis [19] the entropy values at the low-Z end were further found lower than in [20], by 0.5 at 400 MeV/nucleon, which could become clarified once masses get resolved and angular coverage extended within that experiment.

At a finite b, generally, more variation of entropy values throughout the system is expected than at $b = 0$, as spectator regions are characterized by $S/A \sim (1$-$2)$. With regard to the participant region, a shock at a finite b would lead to a lower entropy than a shock at $b = 0$, see Eq. (25) and Fig. 4. If one assumed that about the same amount of entropy

were produced in an expansion at a finite b, as at $b = 0$, then one would expect, on the basis of the RH equation, a change of entropy with b to follow

$$\left(\frac{S}{A}\right)_b - \left(\frac{S}{A}\right)_{b=0} = \frac{S}{A}\left(\rho_1\left(0, E'_{beam}\right), E'\right) - \frac{S}{A}\left(\rho_1\left(0, E_{beam}\right), E\right), \tag{53}$$

where entropy on the r.h.s. is written as a function of local baryon density and of net local energy per nucleon. The density ρ_1 is from Eq. (26) and energies E and E' are related, respectively, to E_{beam} and E'_{beam}, cf. Eq. (25), according to $E = m_N - 16\,\text{MeV} + E_{beam}/2(1 + \sqrt{1 + E_{beam}/2m_N})$. The result for the entropy as a function of b from (53) is shown in the right panel of Fig. 28 with a dashed line. The decrease is clearly in contradiction with the simulation and with data. Note that the experimental entropy [20] is determined from fragments emitted into wide angles, i.e. stemming from the participant region. The consideration, though, ignored till now the weak discontinuity. As the latter spreads, the viscosity slows down the nuclear matter, generating entropy. If one assumed that kinetic energy were completely thermalized for a given density, then one would expect for the matter stemming from the center, instead of (53),

$$\left(\frac{S}{A}\right)_b - \left(\frac{S}{A}\right)_{b=0} = \frac{S}{A}\left(\rho_1\left(0, E'_{beam}\right), E\right) - \frac{S}{A}\left(\rho_1\left(0, E_{beam}\right), E\right). \tag{54}$$

This now leads to an increase of the entropy with an increase of b as the thermalization for a given energy occurs at a lower density. The increase is quadratic in b/b_{max} for low values of the reduced impact parameter, cf. (26), in a qualitative agreement with the data. The difference in entropy between high and low b increases with an increasing beam energy, as seems to be the case with data [20]. Quantitatively, though, the entropy from (54) is still too low compared to the large-multiplicity data displayed in Fig. 28 or the simulation at large b. (Although at a maximum compression at finite b the entropy gets, indeed, as close to $(S/A)\left(\rho_1\left(0, E'_{beam}\right), E\right)$ as at $b = 0$.) The result from (54) is shown by a solid line in Fig. 28 and only the difference between the solid and dashed lines can be attributed to the viscosity. The additional entropy at large b is associated with the rise in the entropy generated during expansion, when the size of participant region diminishes. For b close to

maximum the participant mass is [88] $A_{part} \simeq 3\sqrt{2}\,A\,(1 - b/b_{max})^2$, where $A\,(= 197)$ is the mass of one nucleus. With the scaling in the simulations such as in (52), the generated entropy behaves then as $\delta(S/a) \propto (1 - b/b_{max})^{-2/3}$ for large b.

Summing up the discussion on entropy production, most entropy at $b = 0$ is due to shock waves and some is generated in expansion. As b increases, the shock contribution to the entropy in the participant region decreases, and the contribution of the spreading weak discontinuity rises from 0. Given that the density at the center approaches ρ_1 from Eq. (26) and entropy approaches $(S/A)\,(\rho_1\,(0, E'_{beam})\,, E)$, it is apparent that properties of matter in the compressed state at the center can be regulated by selecting impact parameters and changing the beam energy. The entropy per nucleon generated in expansion increases with b. Even at $b = 0$ and a high energy, the entropy in the vicinity of particle emission points is spread out around the mean entropy in a reaction, because of the dissipation.

B. Collective Energy

Very recently, values of mean baryon energies [15–18] and shapes of spectra [17,18,21] have been used to extract the magnitude of collective energy in collisions. (Procedures followed, in particular, Eq. (33) and nonrelativistic versions of Eqs. (42) and (46), with Coulomb corrections; see also [22].) It is then worthwhile to discuss the experimental results on the energy and compare them to calculations.

The collective-energy values of about 18, 31, and 51 MeV/nucleon, deduced by the FOPI collaboration using intermediate mass fragments (IMF) [17] from central Au + Au reactions at beam energies of 150, 250, and 400 MeV/nucleon, come close to the values of collective energy at freeze-out in present simulations, of 21, 35, and 55 MeV/nucleon at the respective beam energies, see Fig. 9. Revision [18] of the result for 150 MeV/nucleon, with a lower bound on collective energy put at 10 MeV/nucleon, stemmed from a concern that studied events were not exactly central, and the value of collective energy was inflated due to a persistence of longitudinal motion and a particular angular range of the detector setup.

It is argued below that latter bound is likely too cautious.

As the separation of kinetic energy into collective and thermal or excitation components occurs at freeze-out, this separation should not depend very strongly on impact parameter (cf. discussions in Sec. III and Ref. [22]; excitation energy is not expected to vary rapidly). The collective energy per nucleon for light baryons from simulations, as a function of impact parameter, is illustrated in Fig. 31. Between $b = 0$ and $b = 12$ fm the energy rises only by 20%. For heavier particles, and if statistical decays of spectator fragments were taken into account, the rise would be generally faster. Nonetheless, in the $(p^\perp\text{-}y)$ distribution presented in [18] no traces of any spectator decay can be seen. An average impact parameter is $\langle b \rangle \lesssim 3$ fm, and particle charge is $3 \leq Z \leq 8$. Relative to $b = 0$, for such charges and impact parameters, still only a small change of collective energy would be expected. What definitely changes with the impact parameter is the division of collective energy between the longitudinal and transverse degrees of freedom. If simulations adequately described the situation in reactions, then, at representative impact parameters, the energy per transverse degree of freedom would be close to the longitudinal energy, and the angular cuts in [17,18] would not affect the deduced value. (Note, that the equality of energies per degree of freedom does not contradict azimuthal anisotropies [18], cf. Sec. IV B.) Given an unfavorable situation for the determination of collective energy, with an anisotropy similar to that in the simulation at $b = 0$, but with more collective energy associated with the longitudinal degree of freedom than with one transverse, one could still put a more stringent lower bound on the collective energy than in [18], at 14 MeV/nucleon, taking into account angular cuts and a behavior of particle energies with Z, and assuming smooth momentum-distributions. Analogous lower bounds, about 25% below the initially deduced values [17], at 27 and 40 MeV/nucleon, respectively, could be put on the collective energy in the central Au + Au collisions at the two other beam energies of 250 and 400 MeV/nucleon.

At $b \sim 0$, or when examining transverse directions [22], one might expect a gradual decrease of collective energy with mass. Thus, in Fig. 3 it can be seen that regions with a high entropy, from which few heavy particles would originate, freeze-out early and are

associated with relatively high collective velocities. Regions with low entropy, on the other hand, would freeze-out late and would be associated with lower than average collective velocities. Spectra of IMF, corresponding to wide angles in the c.m., from Au + Au reactions at 100 MeV/nucleon and $b \lesssim 4$ fm, were analysed in [21], and collective energy per nucleon gradually decreasing with fragment mass was deduced. The mean collective energy at the low mass end was ~ 9 MeV/nucleon, which should be compared to (cf. [22]) $(3/2)E_{coll}^{\perp} \sim 11.5$ MeV/nucleon in the simulations of that system at the respective impact parameters.

VII. DEPENDENCE ON INTERACTIONS

A. Collective Energy

Judging from Fig. 31, little sensitivity of the collective energy to nuclear compressibility might be expected, as the latter generally brings less change to nuclear collisions than wide variations of impact parameter. In fact, e.g. in the head-on 400 MeV/nucleon Au + Au reaction, the net collective energy per nucleon is found the same, within ~ 1 MeV, for $K = 200$ MeV and $K = 380$ MeV. On the other hand, the division of kinetic energy into collective and excitation energy should be sensitive to particle interaction cross-sections which directly affect the freeze-out, see text below Eq. (21). In the aforementioned Au + Au reaction, the reduction of interaction cross-sections throughout the system by 30%, and the reduction following a parametrization [90] $\sigma_{NN}^{med} = \sigma_{NN} \exp(-\nu\rho/\rho_0)$, with $\nu = 0.3$, lead to a drop in the collective energy by 16%, and 10%, respectively, compared to a standard calculation.

On the other hand, a sensitivity to the nuclear compressibility can be expected for the anisotropy of collective energy which is associated with a delay in the start of longitudinal expansion compared to transverse. The delay time is of the order of

$$t_{sh} = \frac{2R - W}{\gamma_0(v_0 + v_1^{sh})} = \frac{(2R - W)(\rho_1 - \gamma_0\rho_0)}{\gamma_0 v_0 \rho_1}, \tag{55}$$

where W is shock width in terms of a distance in normal matter, introduced in an attempt to account for the mean-free-path effects, and v_1^{sh} is shock speed with respect to compressed matter. Relative to the characteristic time scale for transverse expansion $t_{exp} = R/c_s$ (characteristic generally [50,51], beyond the consideration in Sec. III B), where c_s refers to compressed matter, the delay time is

$$\frac{t_{sh}}{t_{exp}} = \frac{(2 - W/R)\, c_s}{\gamma_0(v_0 + v_1^{sh})}.\tag{56}$$

Small changes in the relative delay time lead to finite changes in the energy components, affecting anisotropy. At any one intermediate beam energy, the ratio (56) is typically larger by $\sim 17\%$ for the stiff equation of state than for the soft, and, correspondingly, the difference between transverse energy per degree of freedom and longitudinal energy is larger for the stiff equation than for the soft. At intermediate energies the shock width in (56) may be expected, on the basis of Navier-Stokes equations [53], to be of a magnitude $W \simeq 2\tilde{\lambda}$, where $\tilde{\lambda} = 1/(\tilde{\sigma}\rho_0)$, and where $\tilde{\sigma} \simeq 30$ mb is an isotropic cross-section that yields the same transport properties as the differential NN cross-section [53]. This roughly conforms with $W \sim 5$ fm seen in Fig. 3. For the stiff equation of state in the 400 MeV/nucleon Au + Au collision, the ratio (56) is then estimated at about 1 ($c_s \sim 0.6c$ for the state from RH equation), and for the soft equation at about 0.85 ($c_s \sim 0.45c$). The reduction in the relative delay time with the change of compressibility leads to an increase of longitudinal energy at the cost of transverse energy by ~ 2 MeV/nucleon in the Au + Au simulation (see Fig. 9 for energy values), decreasing the anisotropy of the *collective* energy at freeze-out, $\chi_{coll} = (E_{col}^{\perp}/2 - E_{coll}^{\parallel})/E_{coll}^{\parallel}$, from $\chi_{coll} \simeq 0.8$ to $\chi_{coll} \simeq 0.45$.

Following (56), a reduction in cross sections (or, more generally, interaction rates) compared to free space by $\sim 20\%$ may lead to a similar decrease in the delay time and in collective-energy anisotropy, as the change in the compressibility above. Indeed, in a simulation of the Au + Au reaction using a stiff equation of state, the reduction of cross section by 20% gives $\chi_{coll} \simeq 0.40$. A near-isotropy in collective energy could be expected, following (56), for a 40-50% reduction in cross sections. In a simulation the collective energy

52

components per degree of freedom become identical when cross sections are reduced by 40%.

On the basis of (56) and more generally, one might expect similar results from the dynamics when varying the size of a system by a factor, as when varying cross sections by the same factor. Results would need, in fact, to be the same, up to a general rescaling of multiplicities, if nuclei were sharp-edged spheres. (It would not matter whether r.h.s. of Eqs. (1) and (6) were multiplied by some factor, or l.h.s. were divided by the same factor; see also [91].) On the basis of the tests above, one might specifically expect that an isotropy of collective energy would be obtained if nuclear radius were reduced by 40%, i.e. mass reduced to $A \sim 40$. Simulation of a head-on 400 MeV/nucleon Ca + Ca reaction yields a result in a disagreement with this expectation, $\chi_{coll} \simeq -0.25$, demonstrating the importance of corona effects for a light system as compared to heavy [66], given a similar width of the nuclear surface region.

The corona effects play a lesser role when only directions pointing away from the beam axis are examined. Consequently, scalings expected on the basis of (56) may be followed to a larger extent at a finite b/b_{max}, than at $b = 0$. The ratio (56), without any modifications, is relevant for dynamics at $b/b_{max} \lesssim 1/3$. At $b/b_{max} \sim 0.25$ and at the beam energy of 400 MeV/nucleon, the anisotropy of *particle* energies $\chi = \langle E^y \rangle / \langle E^{x'} \rangle - 1$, generally somewhat lower than χ_{coll}, is $\chi \simeq 0.65$ in a Au + Au simulation when using stiff equation of state, and $\chi \simeq 0.40$, 0.45, and 0.40, respectively, when using soft equation, when reducing collision rates by 20%, and when turning to a Nb + Nb system with nuclei of a $\sim 20\%$ lesser radius than Au.

The 400 MeV/nucleon data [67] displayed in Fig. 15(b) rule out the soft equation of state with momentum dependence in the optical potential missing, in a combination with free-space or lesser cross-sections. After modifying the elements of calculated kinetic-energy tensor on the account of the fluctuations of estimated reaction-plane direction in the Au + Au reaction, the anisotropy of particle energies for the soft equation of state would continue to be about 0.6 of the anistropy for the stiff equation as above. A corresponding maximum value of $R_\lambda \sim 1.26$ for the soft equation, as a function of the centrality, would fall below the

data. On the other hand, the data would allow for the stiff equation of state in a combination with cross sections reduced by 10% at the particular beam energy compared to free space.

B. Hollow Structures

In transport simulations of head-on Mo + Mo collisions at 60 and 100 MeV/nucleon, Moretto *et al.* [30] noted a formation of disk structures perpendicular to beam axis, which fragmented with time. Further analyses [31,32] revealed openings at disk centers. In the simulations [33] of central collisions of heavy nuclei at 30 MeV/nucleon, bubble structures were observed. Hollows were attributed in [31] to a rarefaction wave reaching the center of a system, while in [33] the issues of Coulomb stability were stressed. The structures generated some experimental interest. Below, the mechanism of the formation of hollow structures is critically reassessed; the particular issues might not be of a grave importance, but the different arguments are being repeated in the literature.

Despite of some increase in their width [53], shock-like interfaces continue to develop in the simulations of central reactions of heavy nuclei, down to beam energies per nucleon of few tens of MeV. Differences between maximum density in the simulations and the RH expectations at the lower beam energies in Fig. 4, are partially associated with a Coulomb repulsion [22]. Between the shocks in reactions, an expansion develops in the directions parallel to shock surfaces, what gives a planarity to transient structures. At energies less than 35 MeV/nucleon, or for cross-sections reduced as compared to free space, and/or for lighter nuclei, the shock width becomes as large as the nuclear diameter and a reacting system equilibrates then as a whole.

The onset of transient structures is marked in Fig. 6 with some increase of density in the vicinity of last particle collisions, towards low beam energies. The fact that structures persist in simulations up to the energies in excess of 100 MeV/nucleon is necessarily conditioned on a massive emission of rapid particles early on in reactions (if few particles were emitted, then structure formation would be limited to the beam energies less than 4 times the binding

54

energy, i.e. ~ 30 MeV/nucleon). The simulations of a Mo + Mo system with a total mass of 196, within the present model, e.g. yield residues of a mass ~ 56, ~ 105, and ~ 177, at the beam energies of 110, 60, and 20 MeV/nucleon, respectively. Figure 32 displays baryon density, radial velocity, and entropy along and perpendicular to the beam axis from the 60 MeV/nucleon $b = 0$ Mo + Mo simulations with and without Coulomb interactions. Emission is evidenced in extended density tails at times $t \gtrsim 50$ fm/c.

The argumentation in [31] implicitly attributes hollow formation to details in a density distribution after equilibration, and specifically to a sharp-edged surface. Following the arguments there, one would find it difficult to understand why hollows do not develop within the simple solution from Sec. III B, or within solutions in Refs. [51,52], or in reaction simulations at $E_{beam} > 150$ MeV/nucleon, or, with reference to everyday experience, why rings do not usually form when spattering water on a tabletop or a wall. An edge in the density distribution might be built onto such a solution as in Sec. III B as a perturbation. A perturbation would satisfy a classical wave equation. With time the initial pulse would move inwards at a speed of sound relative to remaining matter, and emerge from the center as a wiggle in the case of a cylindrical symmetry, with a peak in front followed by a dip, and as as a dip in the case of a spherical symmetry. (Phase shift at the center for the Fourier components of the pulse is $\pi/2$ in the case of a cylindrical symmetry and π in the case of a spherical symmetry.) As can be seen in Fig. 32, the expansion in simulations develops past the maximum in dv/dr in transverse direction, at $t \sim 36$ fm/c, without any noticable depletion in the central density relative to outer regions. This is due to a continuous behavior of parameters of nuclear matter after equilibration. A depletion appears later and is associated with the changes in outer regions of an expanding system.

As the nuclear system expands at a low entropy $S/A \sim 1$, see Fig. 32, down to subnormal densities, a negative pressure develops, cf. Fig. 33. As a result, outer edges of the expanding matter begin to decelerate (the vacuum pressure is zero); see the plateau in transverse velocity in Fig. 32 developing after central density falls below $0.9\,\rho_0$. In consequence, with time the density becomes enhanced at the outer edges as compared to the center. As the

system is driven in the meantime into a region of adiabatic instability within thermodynamic parameters (see also [55,92]), characterized by $(\partial P/\partial \rho)_{S/A} < 0$, the pressure becomes more negative at the outskirts with a higher density, than at the center. From the center then the matter continues to move out and accumulate in the outer regions. The system is being cooled off all the time by emission. Until $t \sim 70$ fm/c from the Mo + Mo system displayed in Fig. 32, particles with a total mass of ~ 35 are emitted. At time $t \sim 100$ fm/c the total mass of emitted particles rises to ~ 60. Apart from the pressure within the system, effects of which are local, Coulomb interactions act. With time, these render a stability to a hollow structure that forms as the matter contracts at the outskirts of the system. When the Coulomb interactions are missing or are weak, the matter having first contracted at the outskirts, gradually collapses onto the center, see Fig. 32(b). This is the case in simulations of such light systems as Ca + Ca.

Deficiency of the single-particle models is the lack of fluctuations. Because of the fluctuations, a system might, in reality, not condense into a ring or a bubble, but into a number of clusters. If a structure were formed, it would later break, due to fluctuations, into clusters of which diameter would be likely commensurate with the minor diameter of a ring, or the thickness of a bubble. In any of these cases a large number of IMF would be produced, slow in the c.m.s. on a scale of collective velocities characterizing the early emission. The total mass of these IMF, e.g. at the beam energy above, could near half of the mass of the system. The unusual abundance of these fragments, already indicated in [34], might thus serve as a signature of the development of an adiabatic instability over a macroscopic region in reactions. The latter underlies both of the scenarios outlined above. Evidence for a planarity in the emission of the slow IMF would additionally show that the instability sets in on a dynamic path for the system. Search for signatures of transient structures in light particles might, on the other hand, be hopeless. These particles are primarily emitted when the fate of matter left behind has not yet been decided.

VIII. CONCLUSIONS

Dynamics of energetic symmetric heavy-ion reactions has been analyzed at a qualitative level, with an attention directed at the collective behavior of nuclear matter. The analysis relied on transport-model reaction-simulations, analytic and near-analytic considerations, and measurements.

In the simulations of head-on reactions, nearly completely developed shock-fronts may be identified, propagating into the projectile and target, and separating the hot matter from normal. In-between the shocks, at finite impact parameters, a tangential discontinuity develops, that spreads with time. Because of small nuclear sizes and finite widths of the discontinuities, they strongly overlap. Hot matter exposed to the vacuum in sidewards directions begins to expand into these directions. Expansion in the shock direction is delayed and does not acquire same strength. The collective expansion affects angular distributions, mean-energy components, shapes of spectra and mean energies of different particles emitted into any one direction, and particle yields.

The stronger expansion perpendicular to the shock direction leads to a c.m. 90° peaking in the polar angle in head-on collisions of heavy nuclei, and to a peaking in the azimuthal angle out of the reaction plane in semicentral collisions. These effects contrast with the naive expectations regarding shocks, where one expects an enhancement of the emission in shock direction. Unambiguous experimental evidence exists only for peaking of the emission in azimuthal angle. Evidence for a motion of matter behind shocks, as characteristic for the weak discontinuity, exists in the strength of the sideward flow in collisions. The strong overlap of the discontinuities dampens this motion, nonetheless, to the extent that spectator pieces can emerge in the high-energy collisions.

The maximum density in reactions falls somewhat below the RH expectations. As a function of the impact parameter, this density follows well the scaling relation (26), falling off quadratically with the impact parameter, while the entropy at the center gets close to that characteristic for stopped matter. It follows then that the thermodynamic parameters of

57

matter in the central region of reactions can be regulated by changing the beam energy and selecting impact parameter. With regard to expansion, its relative strength along and perpendicular to the shock front motion depends on the magnitude of time necessary for a shock propagation through a nucleus, relative to the time necessary for the development of expansion. The relative delay time is larger for the stiff equation of state than for the soft, and the anisotropies in emission, as quantified e.g. using collective-energy or particle-energy components, are larger for the stiff equation of state than for the soft. The delay time depends, moreover, on the interaction cross sections that determine the width of the shock front and the size of a region within which original equilibration occurs. The division of the energy into collective and thermal for a given system at low b, occurring at freeze-out, depends solely on the cross sections.

The effects of expansion on particle spectra at any one c.m. angle in central reactions, are the slopes decreasing with increasing particle mass and downward concavities in baryon spectra. The effect on pion spectra is stronger than following from naive nonrelativistic considerations. A pion spectrum is overall flatter than could be expected from latter considerations and an upward concavity can develop. Resonance decays may, however, fill up this concavity. With regard to pion yields, the missing energy considered by Stock *et al.* when analysing data, may be identified with the collective energy not available locally for pion production. The number of pions and deltas actually decreases within a reacting system towards freeze-out, as the collective motion with participant region acquires strength. Overall, the effect of expansion reduces pion yields by $\sim 50\%$ compared to the situation without expansion.

Collective expansion is not fully isentropic towards freeze-out, with produced entropy being associated with the heat conduction. Besides, in reactions the entropy is produced in shock fronts and within a weak discontinuity on account of the shear viscosity. The shock contribution to the net entropy maximizes in head-on reactions. In low-energy collisions, collective expansion initiates the formation of hollow structures. The process further involves negative pressure and adiabatic instability, and finally Coulomb interactions.

As may be apparent, a wealth of physical phenomena is associated with the collective behavior of matter in central collisions. This is in stark contrast with early conclusions on heavy-ion collisions based on limited inclusive data which, dominated by peripheral collisions, appeared consistent with a featureless global equilibrium within the participant region.

ACKNOWLEDGMENTS

REFERENCES

[1] G. F. Chapline, M. H. Johnson, E. Teller, and M. S. Weiss, Phys. Rev. **D8**, 4302 (1973).

[2] W. Scheid, B. Müller, and W. Greiner, Phys. Rev. Lett. **32**, 741 (1974).

[3] M. I. Sobel *et al.*, Nucl. Phys. **A251**, 502 (1975).

[4] P. J. Siemens and J. O. Rasmussen, Phys. Rev. Lett. **42**, 880 (1979).

[5] R. Brockmann *et al.*, Phys. Rev. Lett. **53**, 2012 (1984).

[6] R. Stock *et al.*, Phys. Rev. Lett. **44**, 1243 (1980).

[7] R. Madey *et al.*, Phys. Rev. **C34**, 1342 (1986).

[8] O. Scholten, H. Kruse, and W. F. Friedman, Phys. Rev. C **26**, 1339 (1982).

[9] R. Stock *et al.*, Phys. Rev. Lett. **49**, 1236 (1982); J. W. Harris *et al.*, Phys. Rev. Lett. **58**, 463 (1987).

[10] G. F. Bertsch, S. Das Gupta, and H. Kruse, Phys. Rev. C **29**, 673 (1984).

[11] H. Å. Gustafsson *et al.*, Phys. Rev. Lett. **52**, 1590 (1984); R. E. Renfordt *et al.*, *ibid.* **53**, 763 (1984).

[12] P. Danielewicz *et al.*, in *Proc. XV Workshop on Gross Properties of Nuclei and Nuclear Excitations*, Hirschegg, 1987, ed. H. Feldmeier, p. 91; Phys. Rev. C **38**, 120 (1988).

[13] H. H. Gutbrod *et al.*, Phys. Lett. B **216**, 267 (1989).

[14] W. K. Wilson *et al.*, Phys. Rev. C **41**, R1881, (1990).

[15] H. W. Barz *et al.*, Nucl. Phys. **A531**, 453 (1991).

[16] W. Bauer *et al.*, Phys. Rev. **C47**, R1838 (1993).

[17] W. Reisdorf *et al.*, in *Proc. XXIII Mazurian Summer School on Nuclear Physics*, Piaski, 1993, Acta Phys. Pol. **B25**, 443 (1994); in *Proc. XXII Workshop on Gross Properties*

of Nuclei and Nuclear Excitations, Hirschegg, 1994, ed. H. Feldmeier, p. 93.

[18] S.C. Jeong *et al.*, Phys. Rev. Lett. **22**, 3468 (1994).

[19] C. Kuhn *et al.*, Phys. Rev. **C48**, 1232 (1993); J. P. Coffin *et al.*, Centre de Recherches Nucleaires Strasbourg Report CRN 93-50 (1993), and in *Proc. NATO ASI on Hot and Dense Nuclear Matter*, Bodrum, 1993.

[20] K. G. R. Doss *et al.*, Phys. Rev. **C37**, 163 (1988).

[21] W. C. Hsi *et al.*, report MSUCL-930, 1994.

[22] P. Danielewicz and Q. Pan, Phys. Rev. **C46**, 2002 (1992).

[23] K. G. R. Doss *et al.*, Mod. Phys. Lett. A **3**, 849 (1988).

[24] G. Poggi *et al.*, in *Proc. NATO ASI on Hot and Dense Nuclear Matter*, Bodrum, 1993.

[25] V. Koch *et al.*, Nucl. Phys. **A532**, 715 (1991).

[26] C. Hartnack, Gesellschaft für Schwerionenforschung Report GSI-93-5 (1993).

[27] R. Lacey, private communication.

[28] G. Rai *et al.*, in *Proc. Int. Workshop on the Dynamical Features of Nuclei and Finite Fermi Systems*, Sitges, 1993.

[29] P. Danielewicz and Q. Pan, in *Proc. Int. Workshop on the Dynamical Features of Nuclei and Finite Fermi Systems*, Sitges, 1993, and National Superconducting Cyclotron Laboratory Report MSUCL-911 (1993).

[30] L. Moretto *et al.*, Nucl. Phys. **A545**, 237c (1992); Phys. Rev. Lett. **69**, 1884 (1992).

[31] W. Bauer, G.F. Bertsch, and H. Schulz, Phys. Rev. Lett. **69**, 1888 (1992).

[32] D. H. E. Gross, B.-A. Li, and A. R. DeAngelis, Ann. Phys. **1**, 467 (1992); B.-A. Li and D. H. E. Gross, Nucl. Phys. **A554**, 257 (1993).

[33] B. Borderie et al., Phys. Lett. B **302**, 15 (1992).

[34] H. M. Xu et al., Phys. Rev. **C48**, 933 (1993).

[35] P. Danielewicz and G. F. Bertsch, Nucl. Phys. **A533**, 712 (1991).

[36] P. Danielewicz, Nucl. Phys. **A545**, 21c (1992).

[37] M. Gyulassy, K. Frankel, and E. A. Remler, Nucl. Phys. **A402**, 596 (1983).

[38] G. Röpke and H. Schulz, Nucl. Phys. **A477**, 472 (1988).

[39] S. Nagamiya and M. Gyulassy, in *Advances in Nuclear Physics*, edited by J. W. Negele and E. Vogt (Plenum, 1984), vol. 13, p. 201.

[40] Y. Yariv and Z. Fraenkel, Phys. Rev. **C20**, 2227 (1979).

[41] B. J. VerWest and R. A. Arndt, Phys. Rev. **C25**, 1979 (1982).

[42] H. M. Pilkuhn, *Relativistic Particle Physics* (Springer-Verlag, New York, 1979).

[43] B.-A. Li, Nucl. Phys. **A552**, 605 (1993).

[44] Gy. Wolf, W. Cassing, and U. Mosel, Nucl. Phys. **A552**, 549 (1993).

[45] C. W. de Jager, H. de Vries, and C. de Vries, Atomic Data and Nuclear Data Tables **14**, 479 (1974).

[46] R. J. Lenk and V. R. Pandharipande, Phys. Rev. **C39**, 2242 (1989).

[47] P. Ring and P. Schuck, *The Nuclear Many-Body Problem* (Springer-Verlag, New York, 1980).

[48] H. Feldmeier and P. Danielewicz, National Superconducting Cyclotron Laboratory Report MSUCL-833 (1992).

[49] A. Lang et al., J. Comp. Phys. **106**, 391 (1994).

[50] L. D. Landau and E. M. Lifschitz, *Fluid Mechanics* (Pergamon Press, London, 1959).

[51] Ya. B. Zeldovich and Yu. P. Raizer, *Physics of Shock Waves and High-Temperature Hydrodynamic Phenomena* (Academic Press, New York, 1966) p. 104.

[52] J. P. Bondorf, S. I. A. Garpman, and J. Zimànyí, Nucl. Phys. **A296**, 320 (1978).

[53] P. Danielewicz, Phys. Lett. 146B, 168 (1984).

[54] W. Cassing and U. Mosel, Prog. Part. Nucl. Phys. **25**, 235 (1990).

[55] P. Danielewicz, Nucl. Phys. **A314**, 465 (1979).

[56] P. Danielewicz and G. Odyniec, Phys. Lett. B **157**, 146 (1985); Lawrence Berkeley Laboratory Report LBL-18600 (1984).

[57] B. Średniawa, *Hydrodynamika i Teoria Sprężystości* (Państwowe Wydawnictwo Naukowe, Warszawa, 1977) p. 320; D. J. Acheson, *Elementary Fluid Dynamics* (Oxford University Press, 1990) p. 35.

[58] A. A. Amsden, F. H. Harlow, and J. R. Nix, Phys. Rev. **C15**, 2059 (1977).

[59] P. Danielewicz, in *Proc. Workshop on Physics of Intermediate and High Energy Heavy Ion Reactions*, Kraków, 1987, ed. M. Kutschera (World Scientific, Singapore, 1988) p. 141.

[60] M. Demoulins, Ph. D. Thesis, University Paris Sud, 1989 (Report CEA-N-2628, CEN Saclay, 1990).

[61] H. Å. Gustafsson *et al.*, Mod. Phys. Lett. A **3**, 1323 (1988).

[62] B. Schürmann and W. Zwermann, Phys. Rev. Lett. **59**, 2848 (1987).

[63] C. Gale *et al.*, Phys. Rev. C **35**, 1666 (1987); J. Aichelin *et al.*, Phys. Rev. Lett. **58**, 1926 (1987); Q. Pan and P. Danielewicz, Phys. Rev. Lett. **70**, 2062, 3523 (1993).

[64] M. Gyulassy, K. A. Frankel, and H. Stöcker, Phys. Lett. B **110**, 185 (1982).

[65] M. B. Tsang *et al.*, Phys. Rev. **C44**, 2065 (1991).

[66] H. Stöcker and W. Greiner, Phys. Reports **137**, 277 (1986).

[67] H. H. Gutbrod *et al.*, Phys. Rev. **C42**, 640 (1990).

[68] H. H. Gutbrod, A. M. Poskanzer, and H. G. Ritter, Rep. Prog. Phys. **52**, 1267 (1989).

[69] E. Schnedermann, J. Sollfrank, and U. Heinz, Phys. Rev. **C48**, 2462 (1993).

[70] S. Hayashi *et al.*, Phys. Rev. **C38**, 1229 (1988).

[71] S. A. Bass *et al.*, Phys. Rev. Lett. **71**, 1144 (1993).

[72] S. A. Bass *et al.*, Gesellschaft für Schwerionenforschung Report GSI-94-03 (1994).

[73] J. Cugnon, D. Kinet, and J. Vandermeulen, Nucl. Phys. **A379**, 553 (1982).

[74] Gy. Wolf *et al.*, Nucl. Phys. **A517**, 615, (1990).

[75] C. Fuchs *et al.*, in *Proc. Int. Workshop on the Dynamical Features of Nuclei and Finite Fermi Systems*, Sitges, 1993.

[76] H. W. Barz *et al.*, Zeit. f. Phys. **A302**, 73 (1981).

[77] D. Hahn and N. K. Glendenning, Phys. Rev. **C37**, 1053 (1988).

[78] V. I. Manko and S. Nagamiya, Nucl. Phys. **A384**, 475 (1982).

[79] B.-A. Li and W. Bauer, Phys. Rev. **C44**, 450 (1991).

[80] J. Gosset *et al.*, Phys. Rev. Lett. **62**, 2095 (1991).

[81] D. Brill *et al.*, Phys. Rev. Lett. **71**, 336 (1993).

[82] L. B. Venema *et al.*, Phys. Rev. Lett. **71**, 835 (1993).

[83] B.-A. Li, Nucl. Phys. **A570**, 797 (1994).

[84] S. A. Bass, C. Hartnack, H. Stöcker, and W. Greiner, Phys. Lett. B **302**, 381 (1993).

[85] B.-A. Li, Phys. Lett. B **319**, 412 (1993).

[86] P. R. Subramanian *et al.*, J. Phys. **G7**, L241 (1981); H. Stöcker *et al.*, Nucl. Phys. **A400**, 63c (1983).

[87] J. Kapusta, Phys. Rev. **C24**, 2545 (1981).

[88] J. Gosset, J. I. Kapusta, and G. D. Westfall, Phys. Rev. **C18**, 844 (1978).

[89] L. P. Csernai *et al.*, Phys. Rev. **C35**, 1297 (1987).

[90] D. Klakow, G. Welke, and W. Bauer, Phys. Rev. **C48**, 1982 (1993).

[91] A. Bonasera, L. P. Csernai, and B. Schürmann, Nucl. Phys. **A476**, 159 (1988).

[92] G. F. Bertsch and S. Das Gupta, Phys. Reports **160**, 189 (1988).

FIGURES

FIG. 1. Proton (solid lines) and neutron (dashed lines) density profiles from solving the TF equations, together with the empirical charge density profiles (dotted lines) [45] for ^{40}Ca and ^{208}Pb.

FIG. 2. Contour plots of baryon density in the reaction plane in Au + Au collisions at 400 MeV/nucleon. The displayed contour lines are for the densities $\rho/\rho_0 = 0.1, 0.5, 1, 1.5$, and 2.

FIG. 3. Baryon density (top panels), radial velocity (center panels), and entropy per baryon along (solid lines) and perpendicular (dashed lines) to the beam axis at different indicated times, in the $b = 0$ collision at a beam energy of 400 MeV/nucleon.

FIG. 4. Lines show the baryon density (top panel), temperature (center panel), and total entropy per baryon (bottom panel) expected behind a developed shock front at $b = 0$, as a function of beam energy, from Eq. (16). Filled circles indicate the maximum density from the simulations of $b = 0$ Au + Au collisions at different beam energies. Crosses indicate the maximum density, scaled by a γ-factor according to Eq. (26), from the simulations of 1 GeV/nucleon Au + Au collisions at b = 3, 6, 8, 9, 10, 11, and 12 fm, plotted against the equivalent beam energy following from Eq. (26).

FIG. 5. Time dependence of the baryon density at $r = 0$ (top panel) and the participant transverse collective energy per nucleon (bottom panel) in the $b = 0$ Au + Au reaction at 400 MeV/nucleon.

FIG. 6. Mean baryon densities in units of normal density in the vicinity of last collisions of emitted particles from the head-on Au + Au reactions (solid line), and in the vicinity of collisions from which the final light-clusters originate (dashed line), as a function of beam energy.

FIG. 7. Distribution in the spherical angle of protons (circles), deuterons (triangles), tritons (inverted triangles), pions (diamonds), and pions emitted within first 14 fm/c (stars), as a function of polar angle from the simulation of a $b = 0$ Au + Au collision at 1 GeV/nucleon. The solid line indicates the distribution of tritons expected on the basis of the formula (23).

FIG. 8. Transverse and longitudinal components of the mean energies of particles emitted from $b = 0$ Au + Au reactions, as a function of beam energy.

FIG. 9. Transverse and longitudinal components of the mean collective energy per nucleon at the time of last collision of baryons stemming from $b = 0$ Au + Au reactions, as a function of beam energy.

FIG. 10. The initial discontinuity between the projectile and target velocities breaks at a finite b into two shock fronts propagating into the projectile P and target T (thick solid lines), and a weak tangential discontinuity in-between (dotted line). Shock-front position *within* projectile at a later time is indicated with a dashed line.

FIG. 11. Baryon density ρ (top panel), normal and tangential velocity-components v_n and v_t to the discontinuities in nuclear-matter (center panel), coinciding with radial and polar velocity-components, and entropy per baryon (bottom panel) as a function of the distance from the center of a 400 MeV/nucleon Au + Au system at $b = 7$ fm, along the normal to the discontinuities. At the given time $t = 13.5$ fm/c the discontinuities (at their centers) are inclined at an angle $\alpha \sim 52°$ relative to the beam axis.

FIG. 12. Mean energy component out of the reaction plane at $y = 0$ (top panel), and at all rapidities (center panel), and a lower of the eigenvalues of a relativistic tensor $\langle s^{ij} \rangle$, associated with a direction within the reaction plane (bottom panel), for protons (circles), deuterons (squares), tritons (triangles), and helions (diamonds), emitted from 400 MeV/nucleon Au + Au reactions, as a function of the impact parameter.

FIG. 13. Mean transverse momentum component within the reaction plane, divided by mass, as a function of rapidity for protons (circles), deuterons (triangles), tritons (inverted triangles), and pions (diamonds) from 1 GeV/nucleon Au + Au collisions at $b = 3$ fm (top panel) and $b = 7$ fm (bottom) panel. For collisions at $b = 7$ fm, also the mean momentum for pions emitted within first 16 fm/c is shown (stars).

FIG. 14. Left panel shows the flow parameter (28) in Au + Au reactions at 250 and 400 MeV/nucleons, from the measurements of Ref. [61], as a function of the reduced participant proton multiplicity. Right panel shows the flow parameter from the simulations of Au + Au reactions at 400 MeV/nucleon, as a function of impact parameter.

FIG. 15. Parameters associated with the kinetic-energy tensor in symmetric reactions at 400 MeV/nucleon. (a) Flow angle from the calculated mean kinetic-energy tensor, as a function of reduced impact parameter in Au + Au (stars) and Ca + Ca (diamonds) reactions. (b) Ratio of the out-of-reaction-plane matrix-element to the lower in-plane eigenvalue (crosses), as a function of the normalized participant proton multiplicity in Au + Au reactions, from measurements of Ref. [67], compared to the ratio of eigenvalues (stars) from a calculated tensor with matrix elements modified on account of fluctuations of the estimated reaction plane about the true plane.

FIG. 16. Mean kinetic energy divided by temperature in thermal equilibrium, as a function of temperature divided by mass.

FIG. 17. Baryon density along (solid lines) and perpendicular (dashed lines) to the beam axis at different indicated times, in the $b = 0$ La + La collision at a beam energy of 800 MeV/nucleon.

FIG. 18. Time dependence of baryon density at $r = 0$ (top panel), participant collective energy per nucleon (center panel), and total entropy in the $b = 0$ La + La reaction at 800 MeV/nucleon from the standard calculation (solid line) and from the calculation with an interchange of particle positions (short-dashed lines).

FIG. 19. Time dependence of elastic NN collision-rate (top panel), rates of Δ production in NN collisions and of absorption in ΔN collisions (center panel), and rates of Δ formation in πN collisions and of Δ decay (bottom panel).

FIG. 20. Time dependence of the number of pions and deltas normalized using the baryon number, in the $b = 0$ La+La reaction at 800 MeV/nucleon, from a standard calculation (solid line) and from a calculation with an interchange of particle positions (short-dashed line). The two horizontal long-dashed lines show the equilibrium number of pions and deltas for a baryon density $\rho = 2.25\rho_0$ and an energy per baryon of 1133 MeV and 1103 MeV, respectively. Dots show the number obtained by integrating over space the local equilibrium values of pion and delta density in a standard calculation.

FIG. 21. Isentropes in the plane of the ratio of pion-and-delta density to baryon density vs the baryon density (top panel), and in the plane of the temperature vs the baryon density (bottom panel). Approximate locations of the 800 MeV/nucleon $b = 0$ La+La system at $t = 14$ fm/c in the two planes are marked with crosses. Dashed lines show a portion of a chemical equilibrium path with regard to the pion and delta number.

FIG. 22. Momentum distribution of protons (circles), deuterons (triangles), helions (inverted triangles), negative (squares) and neutral (diamonds) pions from central 800 MeV/nucleon La + La reaction, in the vicinity of 90° in the c.m. Left panel shows the results of calculations at $b = 1$ fm (filled symbols) and data of Ref. [70] (open symbols). Right panel shows the results of calculations with particle positions interchanged during evolution. Solid lines in the left panel indicate results of the instantaneous freeze-out model, for baryons and neutral pions. Long- and short-dashed lines for neutral pions indicate a contribution of free pions at freeze-out and a contribution from Δ decays, respectively. Straight parallel lines in the right panel serve to guide the eye.

FIG. 23. Ratio of the mean pion multiplicity to the number of participant nucleons in central symmetric reactions, as a function of laboratory energy. The solid and dashed lines represent, respectively, the results of standard calculations and of calculations with particle positions interchanged, for the La+La $b = 0$ reactions. The circles represent data of Ref. [9].

FIG. 24. Distribution of collective velocities for baryons from 800 MeV/nucleon La + La reaction at $b = 1$ fm, calculated in the vicinity of last collisions, within an angular range of velocities $\theta = 60 - 120°$.

FIG. 25. Negative-pion distribution in the vicinity of c.m. 90° in the central 1.8 GeV/nucleon Ar + KCl reaction. Insets show pion asymmetry-coefficient defined in Eq. (48). Open circles in both panels indicate data of Ref. [5]; distributions are normalized using event cross-section given there. Filled circles in the left panel indicate results of the present model at $b = 1.7$ fm. Squares and diamonds in the right panel indicate, respectively, the results obtained using the cascade code [73] with anisotropic and isotropic $N + N \leftrightarrow N + \Delta$ cross-sections. It may be mentioned that the present model yields results indistinguishable from those from the cascade code [73], when optical potential is switched off and same assumptions on scattering are adopted.

FIG. 26. Distribution of neutral pions with c.m. momenta $p > 200$ MeV/c (top panel) and protons (bottom panel) in the azimuthal angle ϕ' with respect to the reaction plane, at a momentum component within the reaction plane $p^{z'} = 0$. The angle Θ is the angle of rotation of the $p^{z'}$-axis from the p^{z}-axis in the direction of p^{x}.

FIG. 27. Contour lines (solid) for baryon density in the reaction plane in 1 GeV/nucleon Au + Au collision at $b = 7$ fm and $t = 15$ fm/c, with overlaid contour lines (dashed) for pion and delta density. Baryon contour lines are for density values $\rho/\rho_0 = 0.1, 0.5, 1, 1.5$, and 2. Pion and delta lines are for density values $(\rho_\pi + \rho_\Delta)/\rho_0 = 0.02, 0.1$, and 0.2.

FIG. 28. Left panel shows entropy per nucleon as a function of reduced participant proton multiplicity, determined from 400 MeV/nucleon Au + Au wide-angle data of Ref. [20]. Right panel shows, as a function of impact parameter, the entropy per nucleon associated with nucleons emitted into wide angles from reaction simulations (circles), cf. [35], and predictions for the entropy from Eq. (53) (dashed line) and from Eq. (54) (solid line).

FIG. 29. Ratios of cluster yields to proton yields at wide angles, cf. [35], as a function of bombarding energy in the head-on Au+Au reactions. The solid and dashed lines represent, respectively, the results from standard calculations and from calculations with particle positions interchanged. The dots represent data of Ref. [20].

FIG. 30. Distribution of entropy per baryon in the vicinity of last collision points in the 400 MeV/nucleon $b = 0$ Au + Au reaction simulation.

FIG. 31. Impact-parameter dependence of the mean participant collective energy per nucleon (stars) and transverse collective energy per nucleon (diamonds), calculated as in Eq. (21), in Au + Au reactions at 400 MeV/nucleon.

FIG. 32. Baryon density (top panels), radial velocity (center panels), and entropy per baryon along (solid lines) and perpendicular (dashed lines) to the beam axis at different indicated times, in the head-on Mo + Mo reaction at 60 MeV/nucleon, from a simulation with (a) and without (b) Coulomb interactions.

FIG. 33. Isentropes in the plane of pressure vs density for the stiff equation of state.
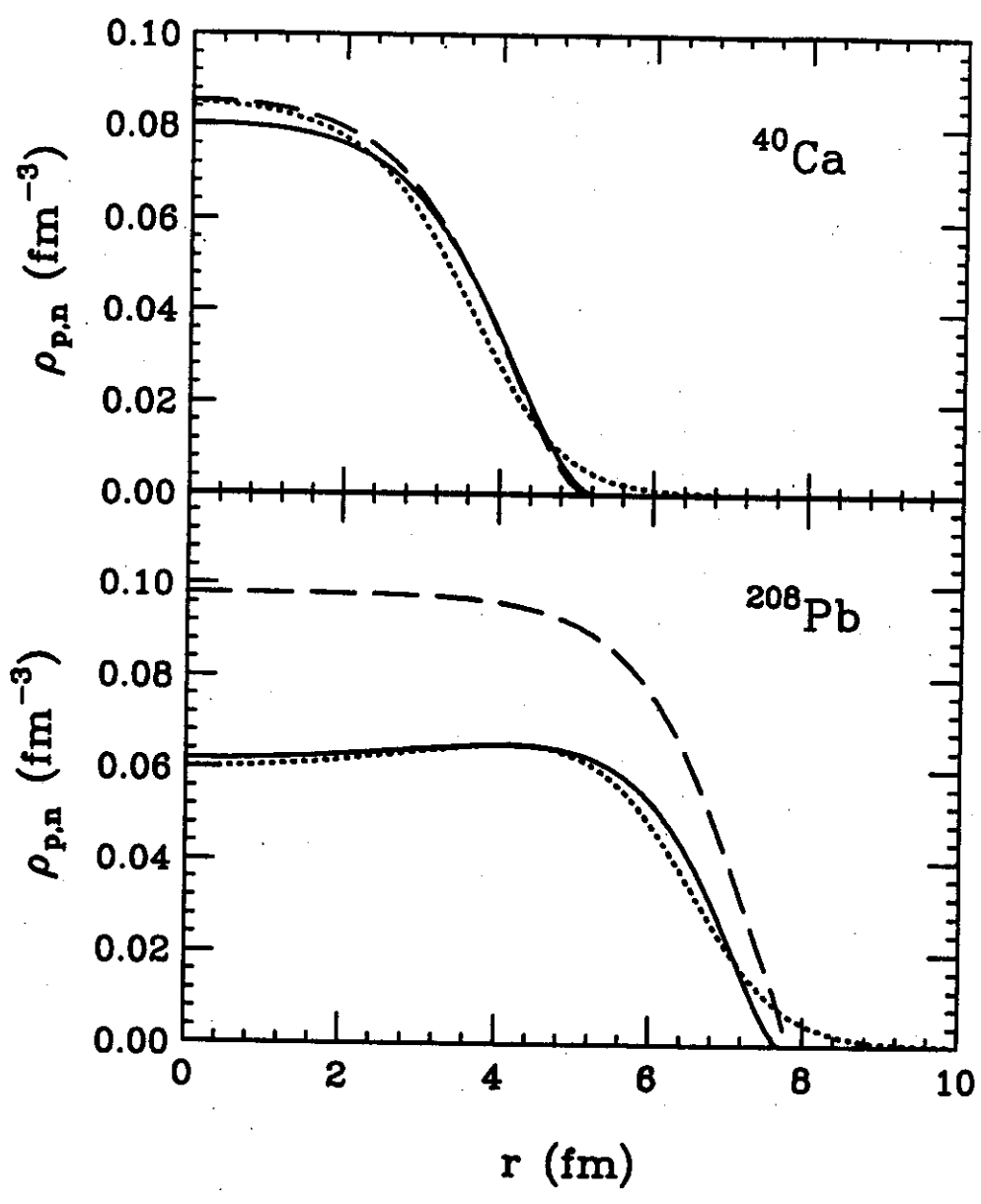
Fig. 1

Au + Au (400 MeV/nucleon)
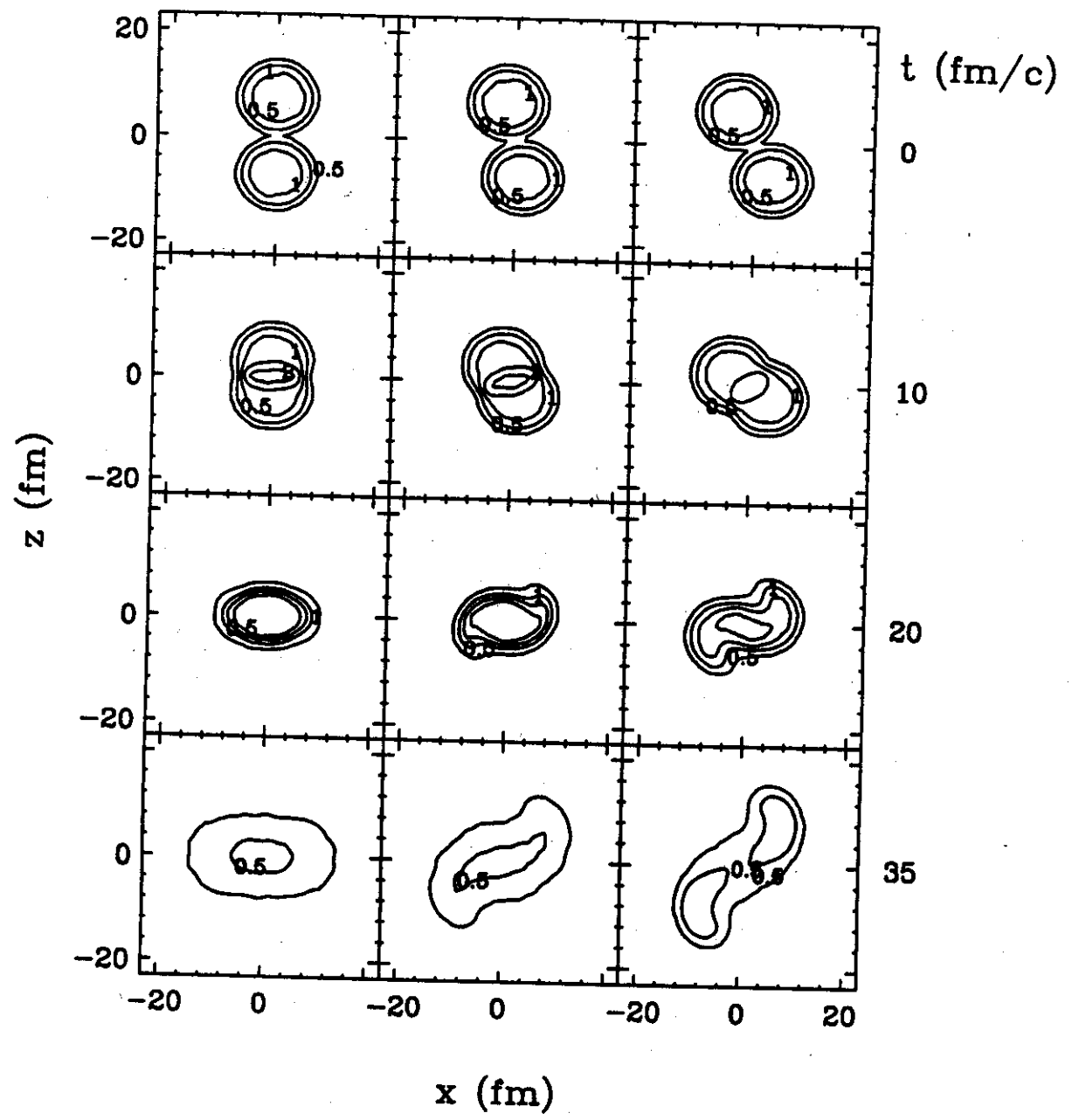
Fig. 2

Au + Au   400 MeV/nucleon   b = 0
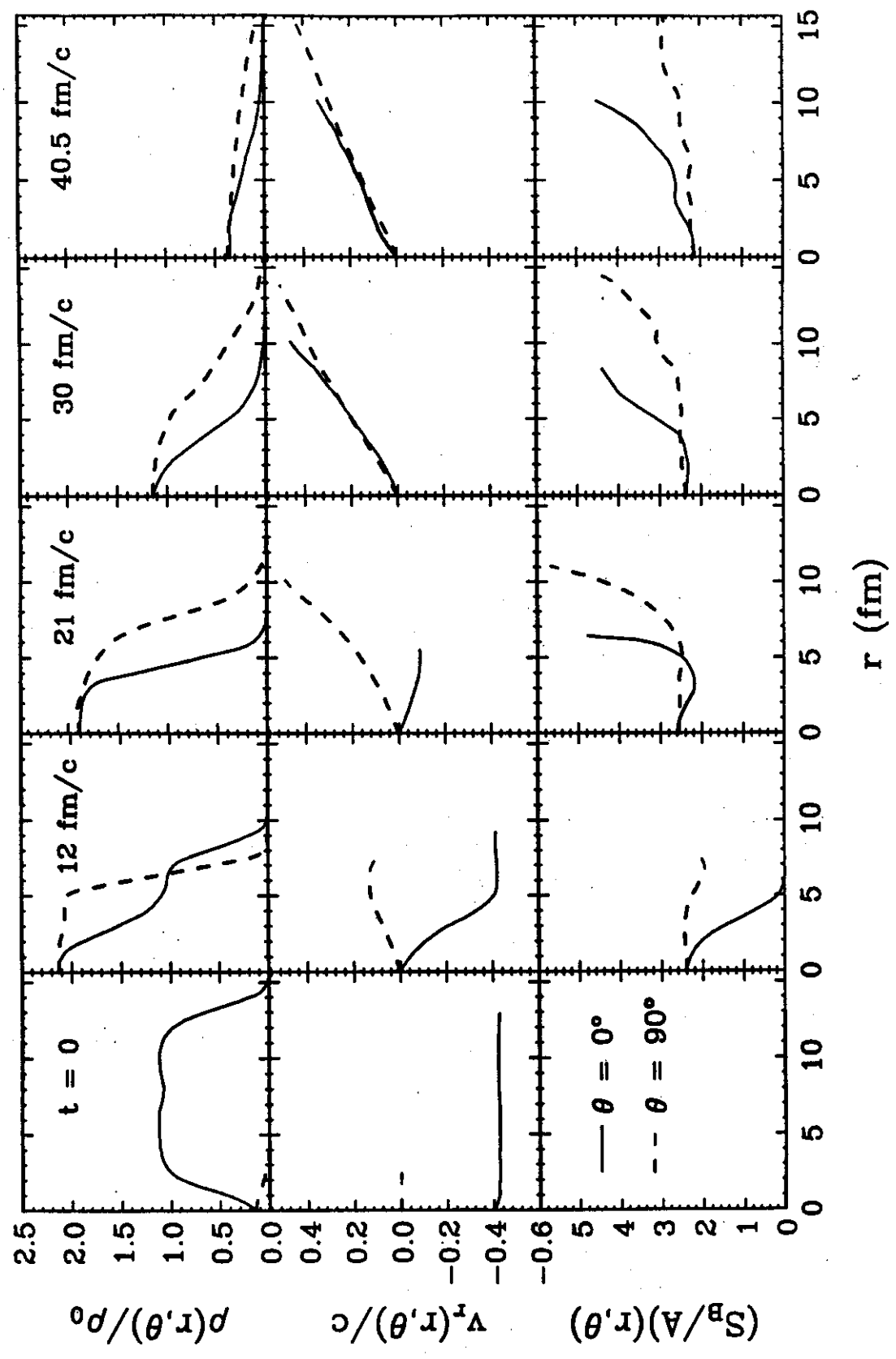
Fig. 3

Rankine–Hugoniot

Fig. 4
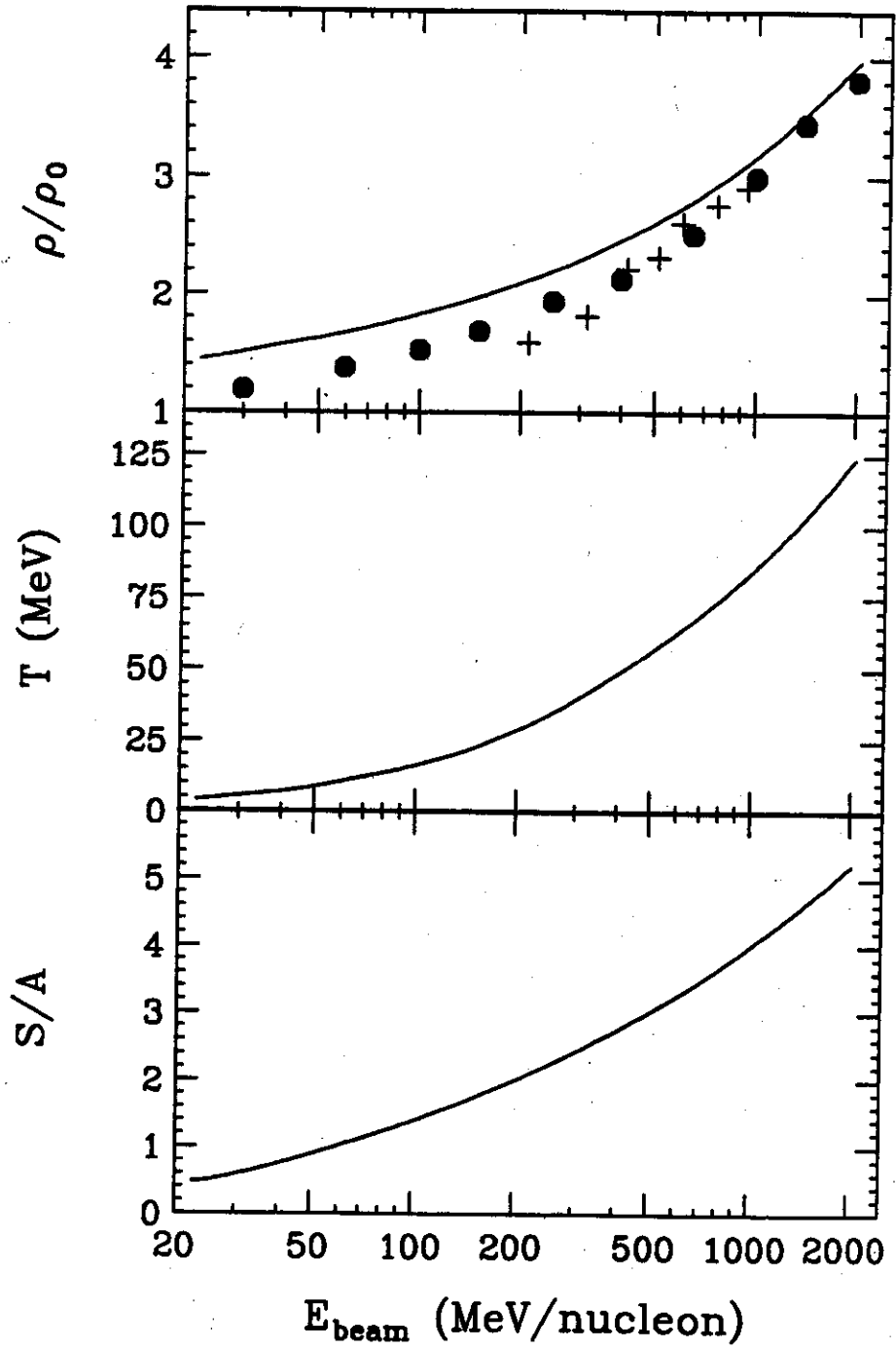
Au+Au 400 MeV/nucleon b=0
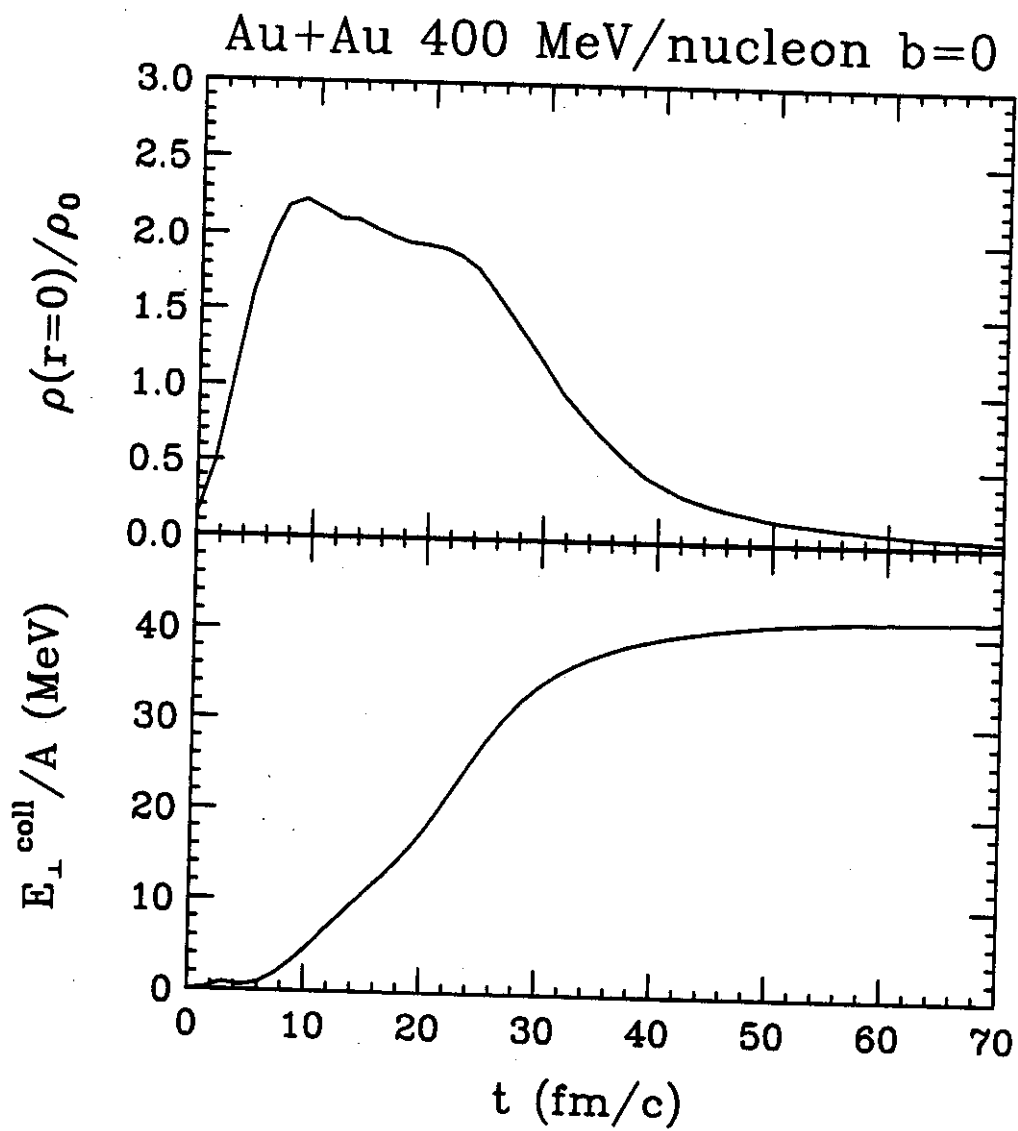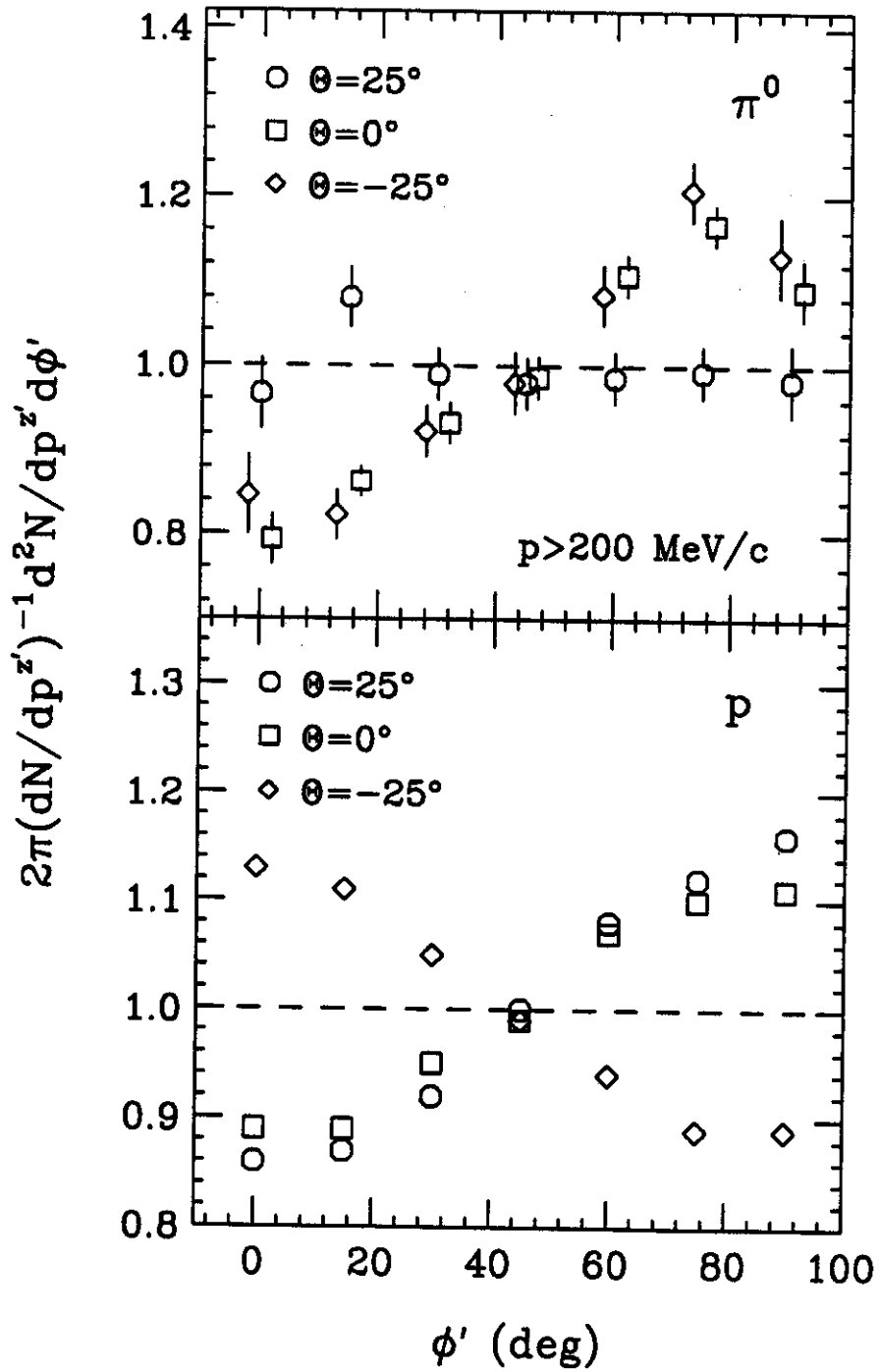
Fig. 5
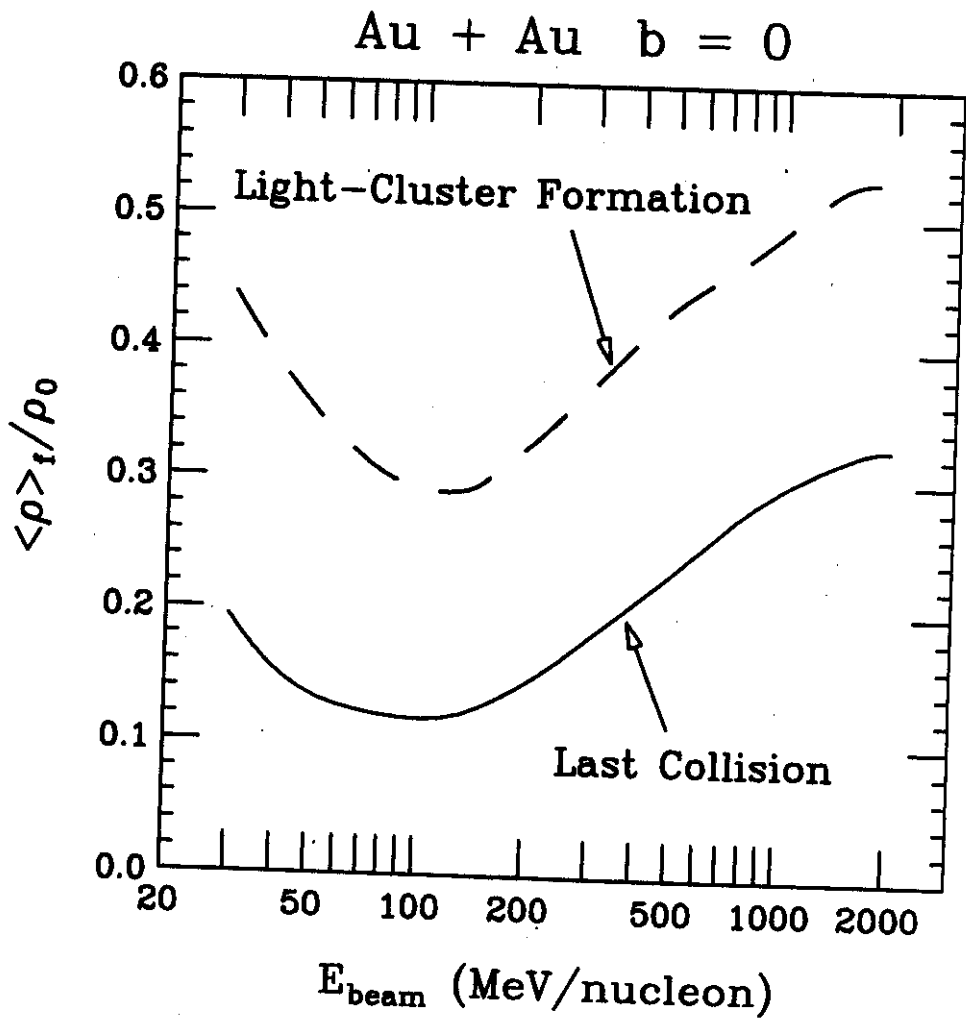
Fig. 6

Au + Au   b = 0
1 GeV/nucleon
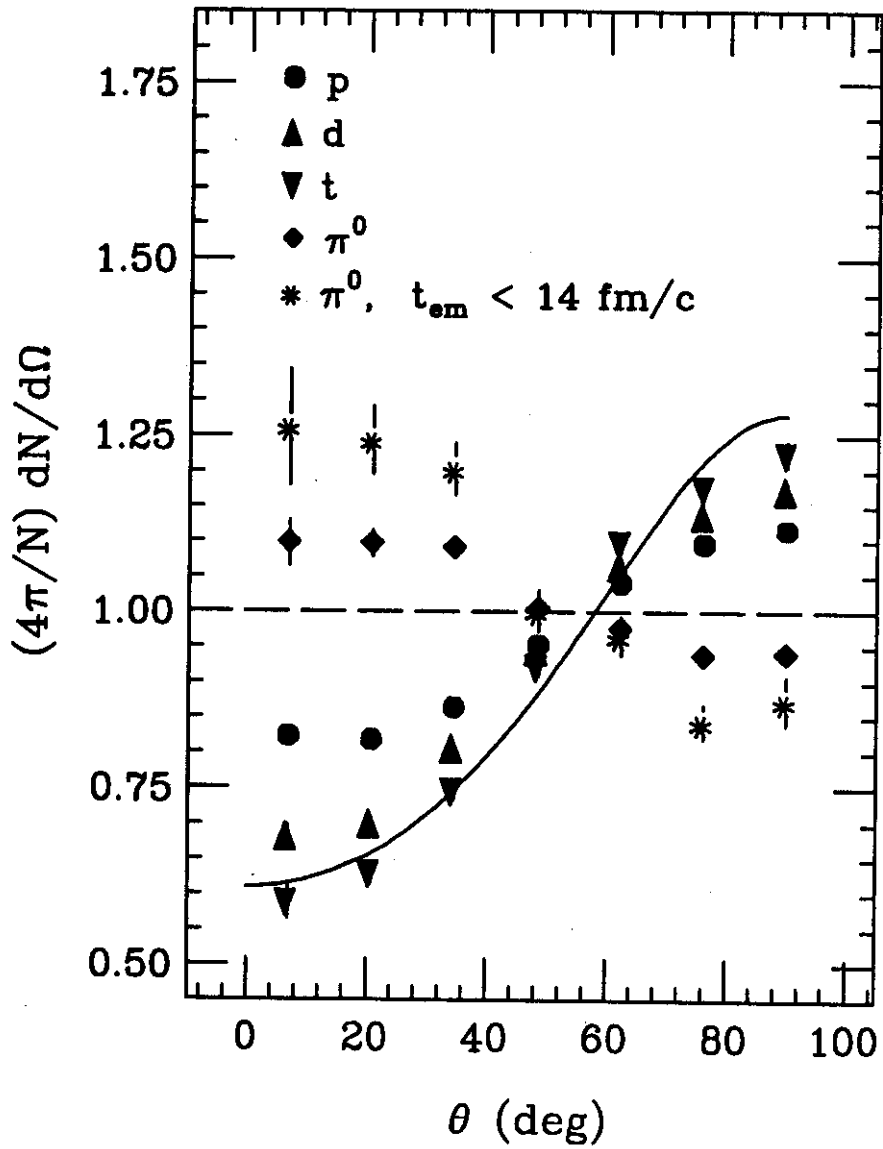
Fig. 7
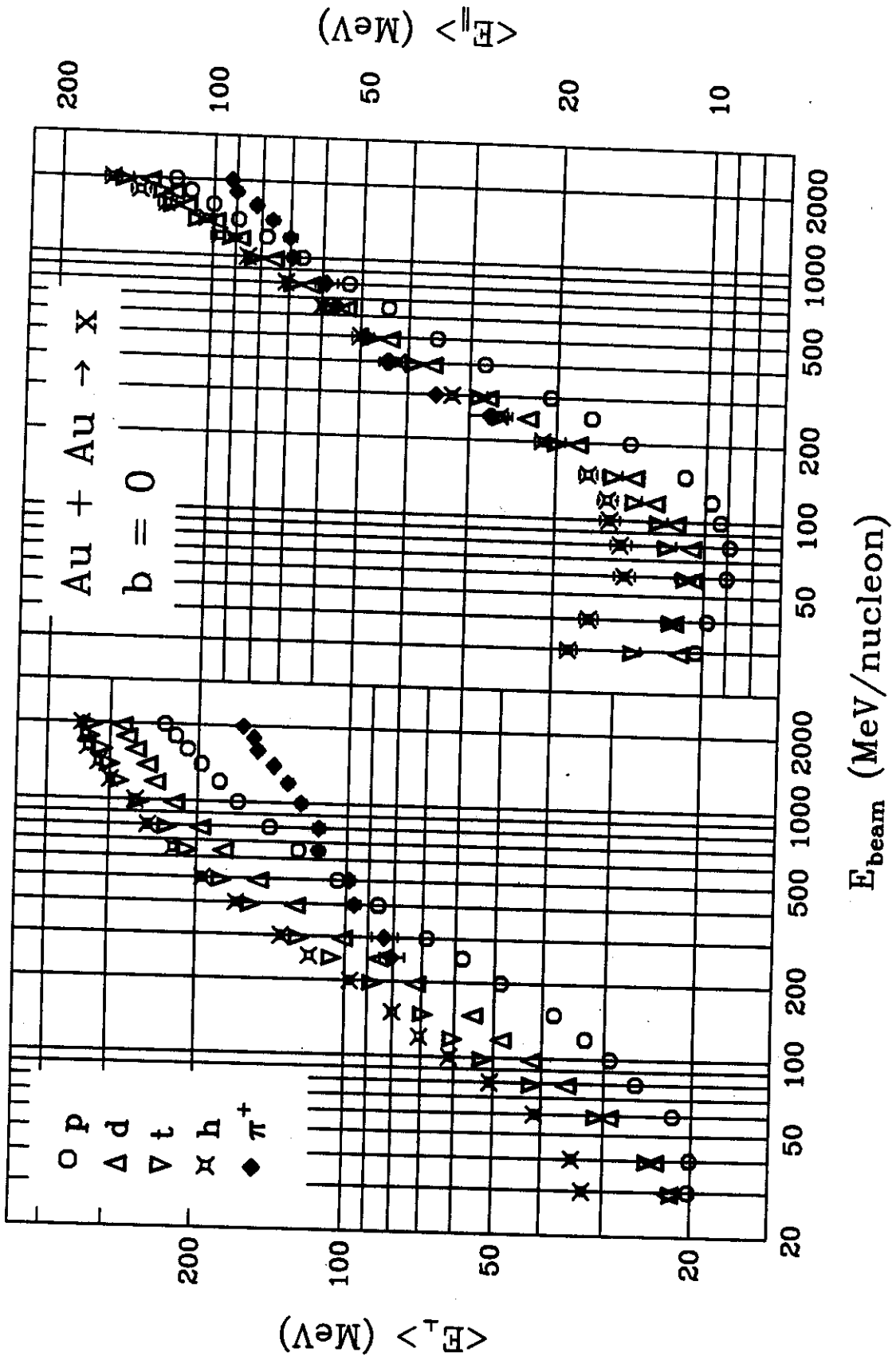
Fig. 8
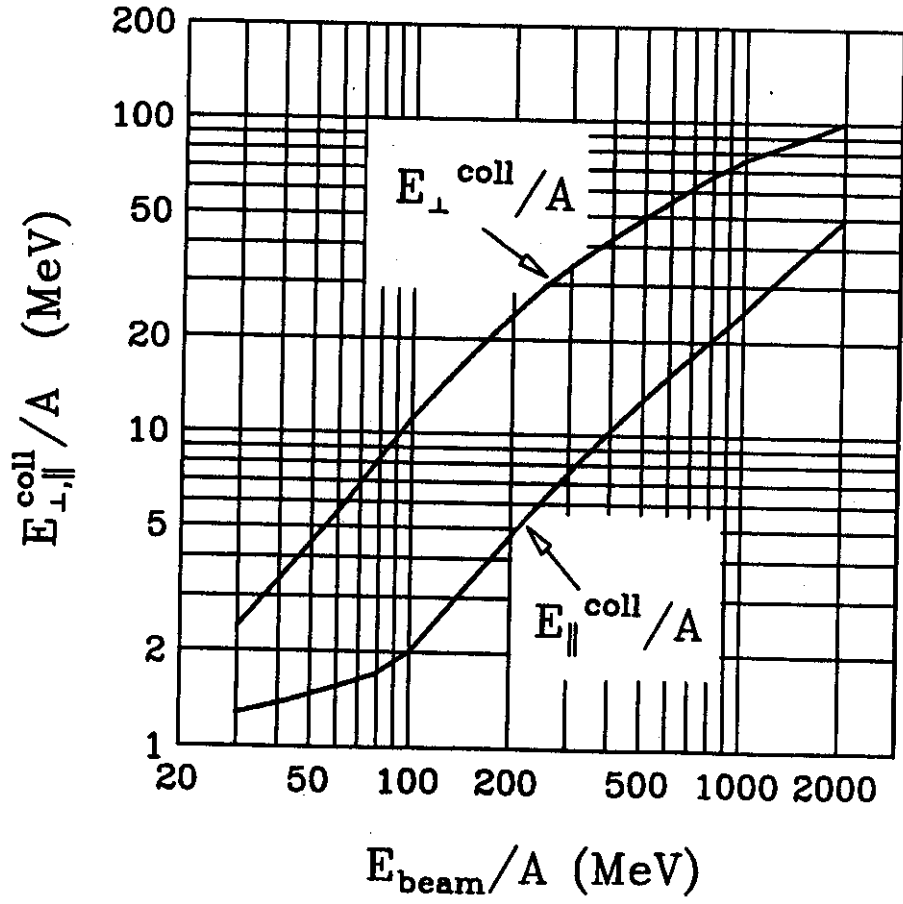
Fig. 9
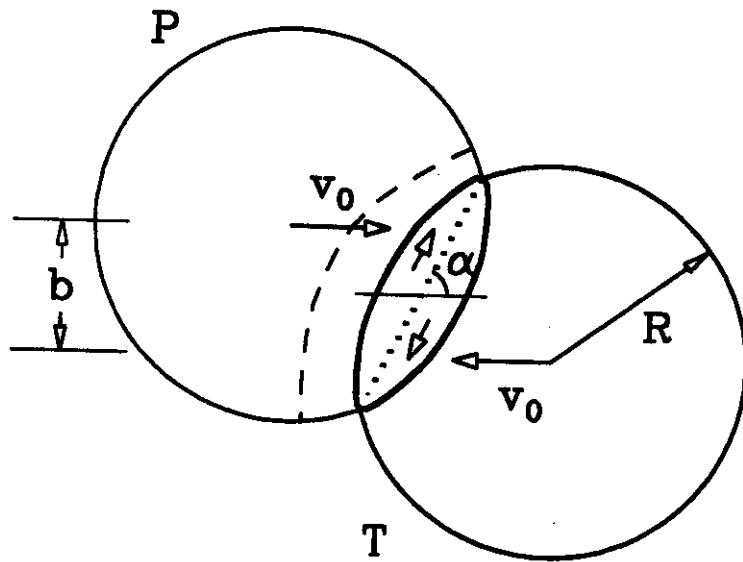
Fig. 10

400 MeV/nucleon
Au + Au   b = 7 fm

t = 13.5 fm/c

ϕ = 180°
θ = 38°
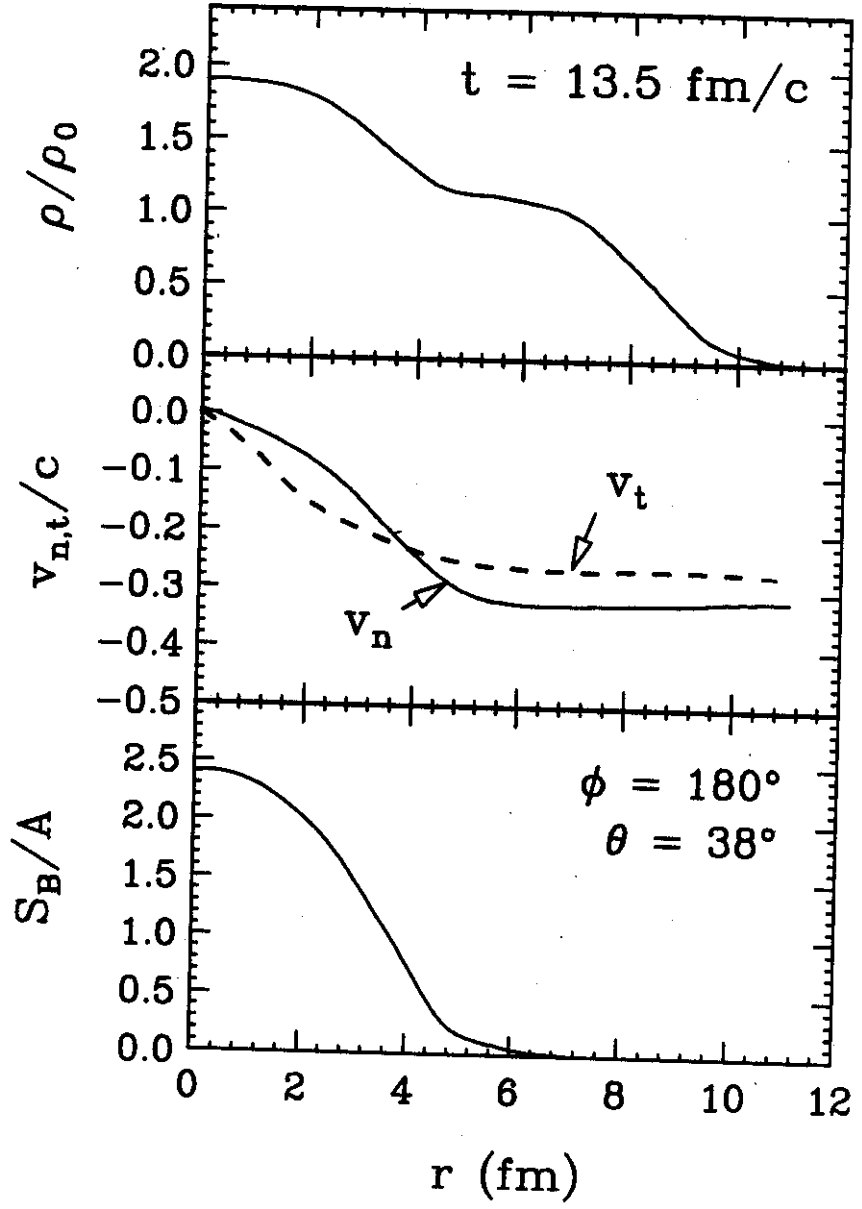
Fig. 11

400 MeV/nucleon Au + Au
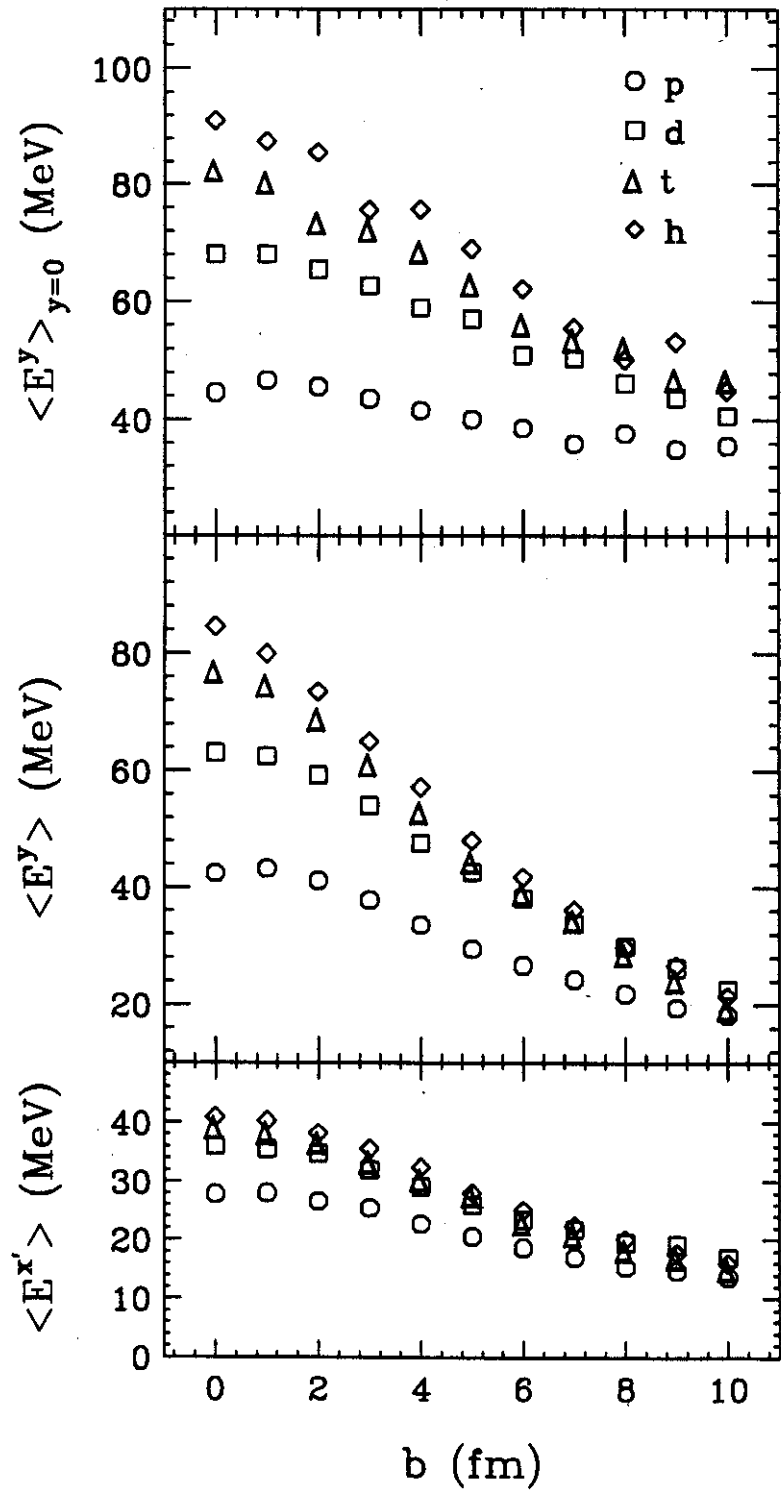
Fig. 12
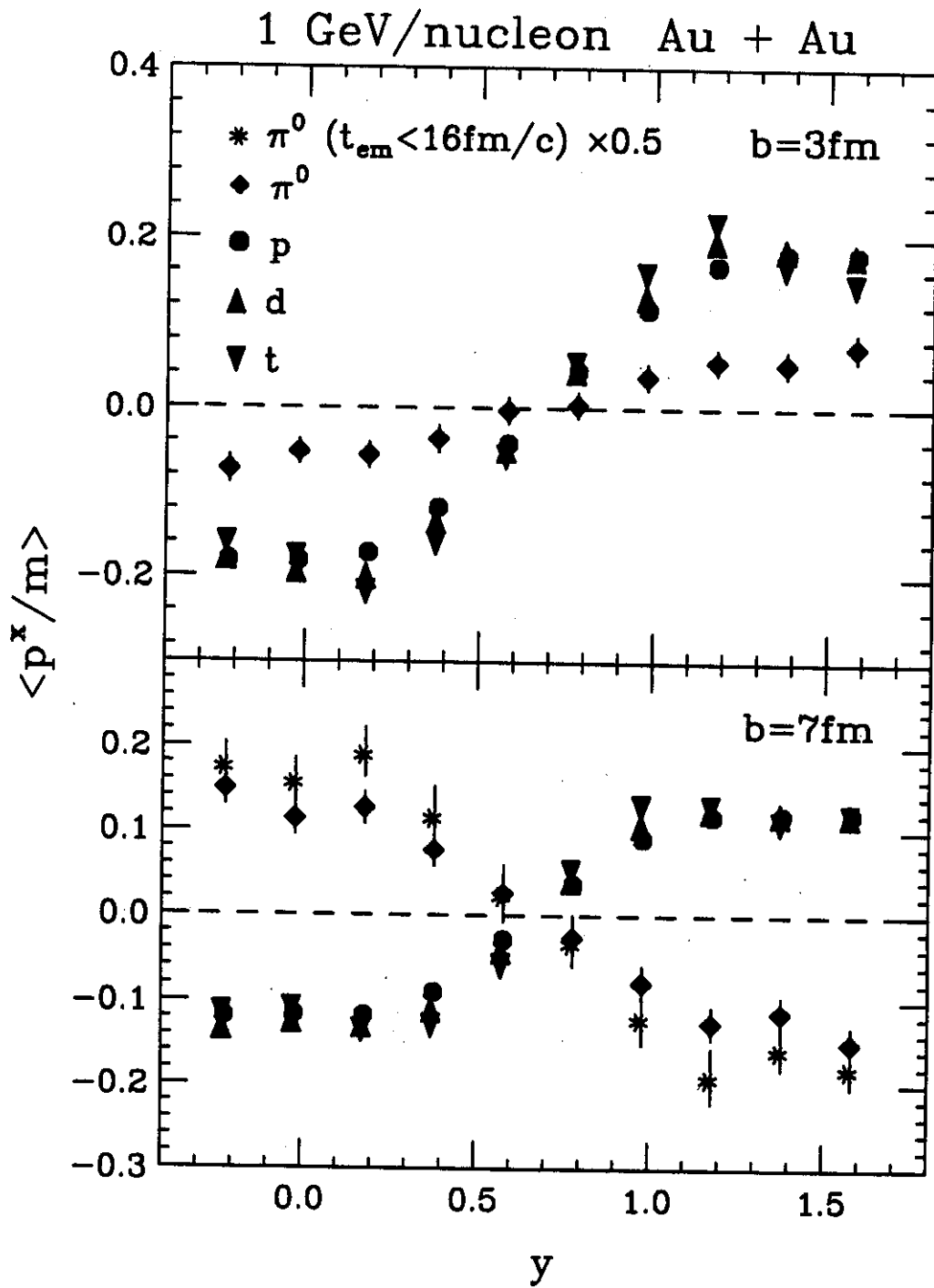
Fig. 13
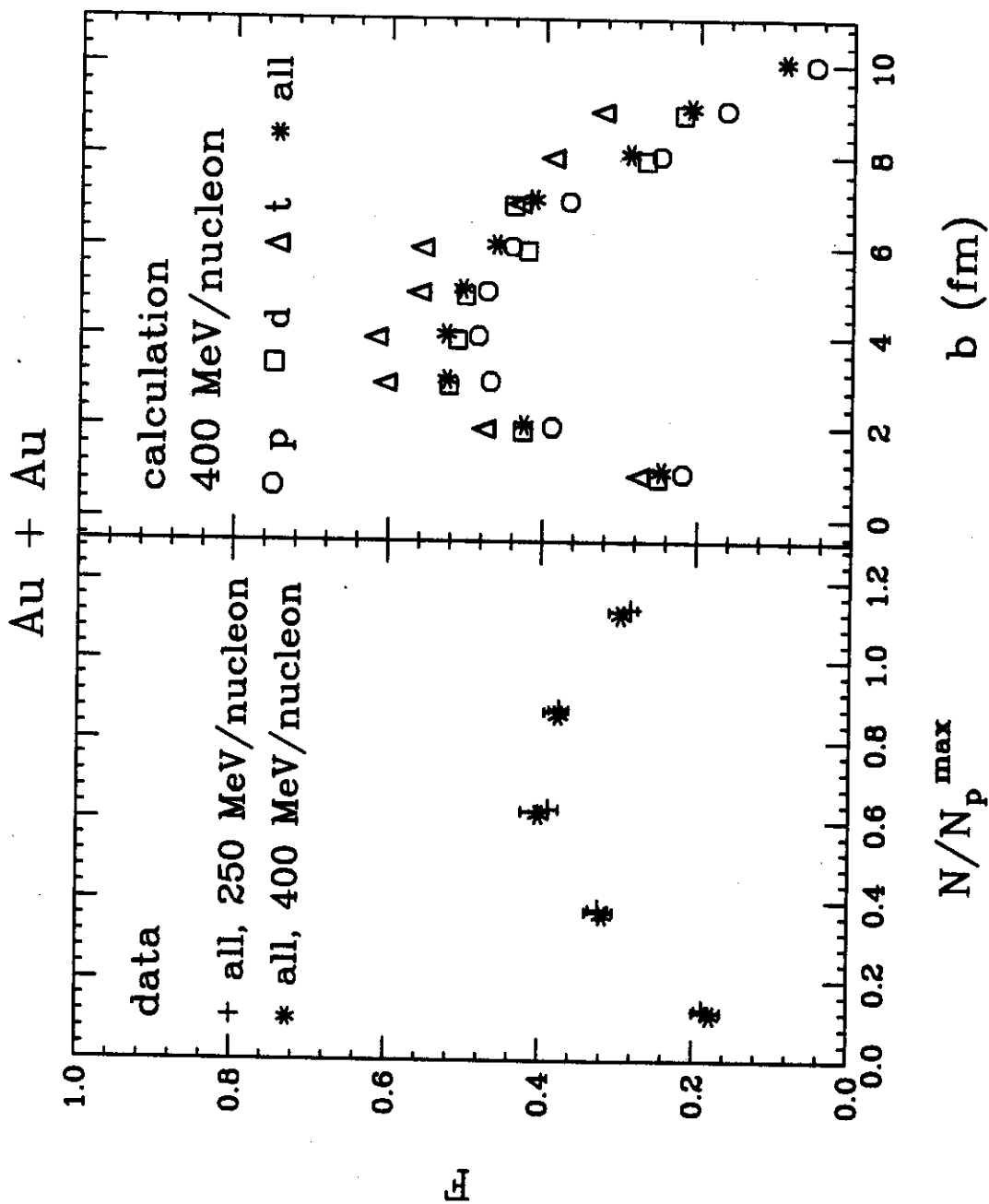
Au + Au

Fig. 14
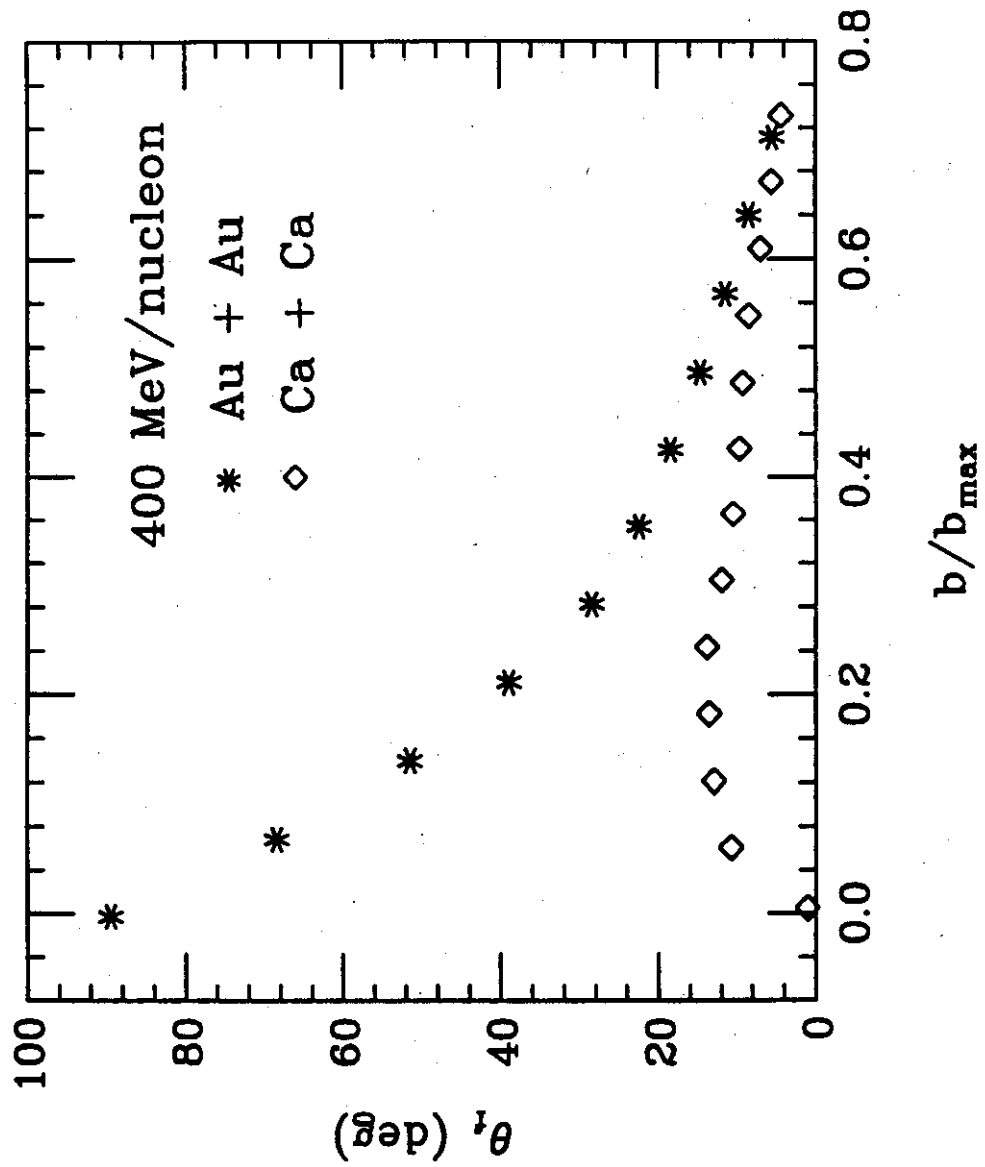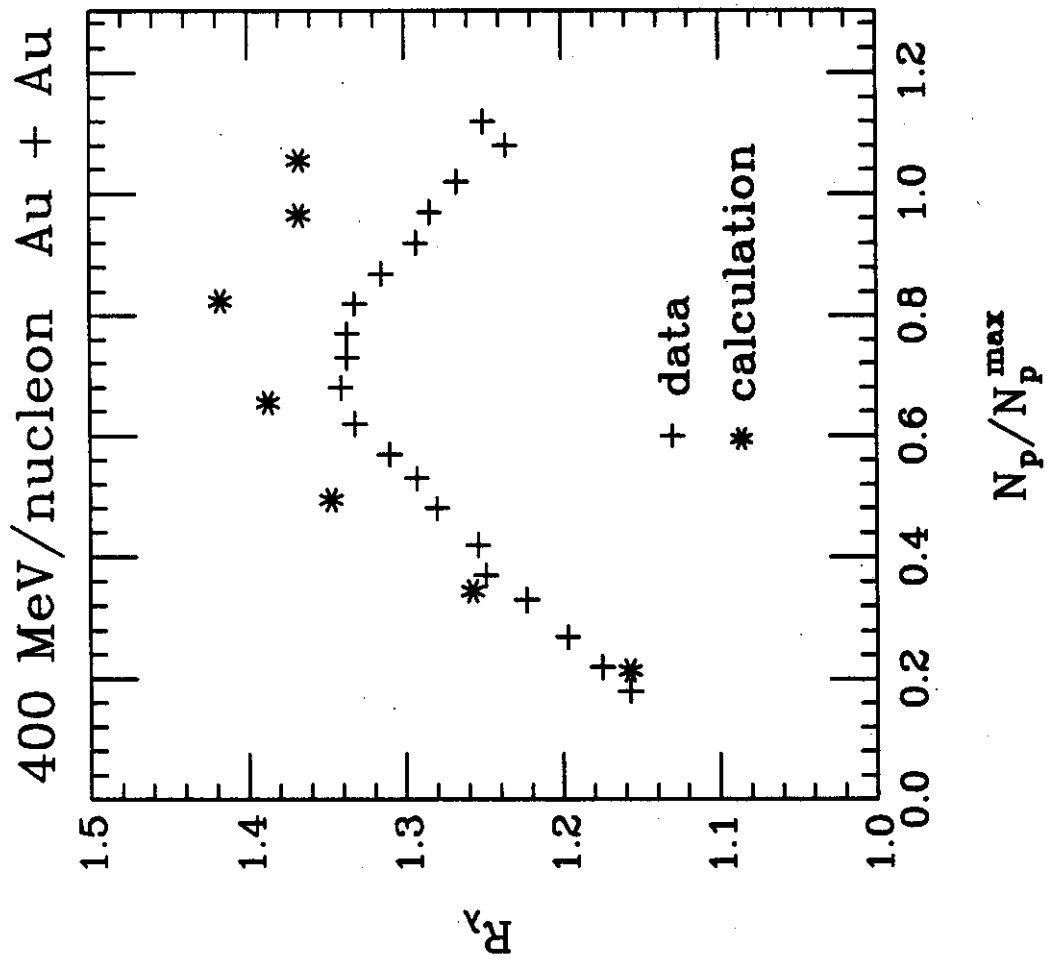
Fig. 15(a)

Fig. 15(b)
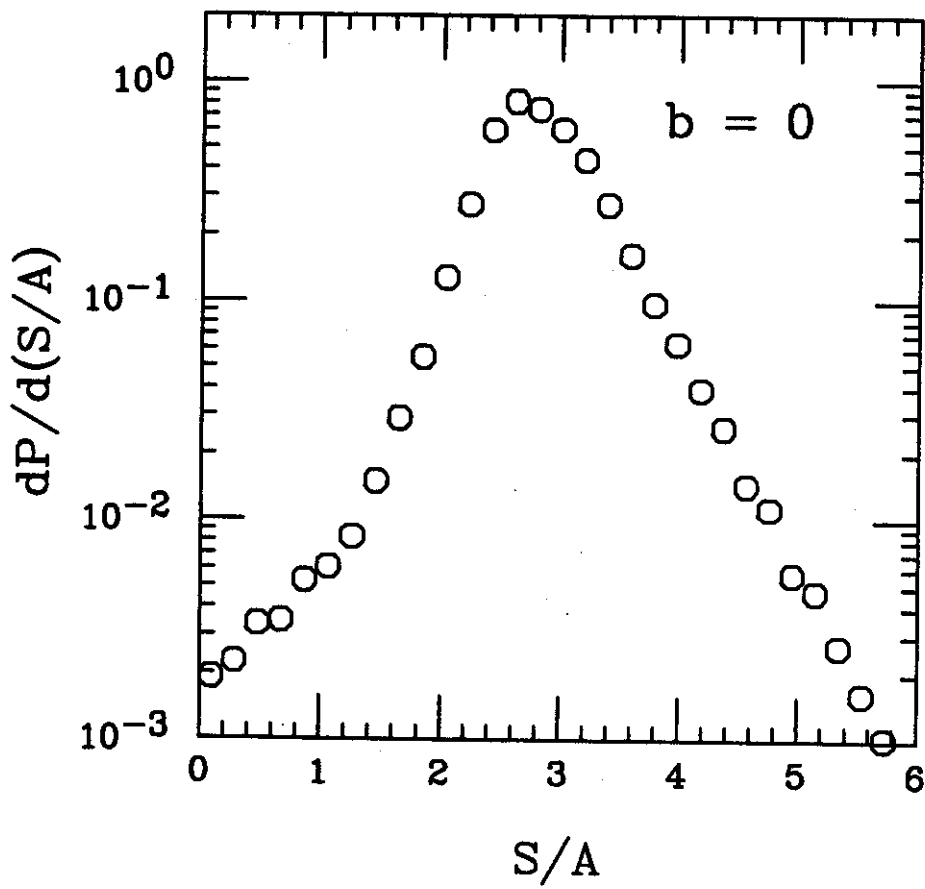
RELATIVISTIC BOLTZMANN GAS

Fig. 16

La + La   800 MeV/nucleon   b = 0
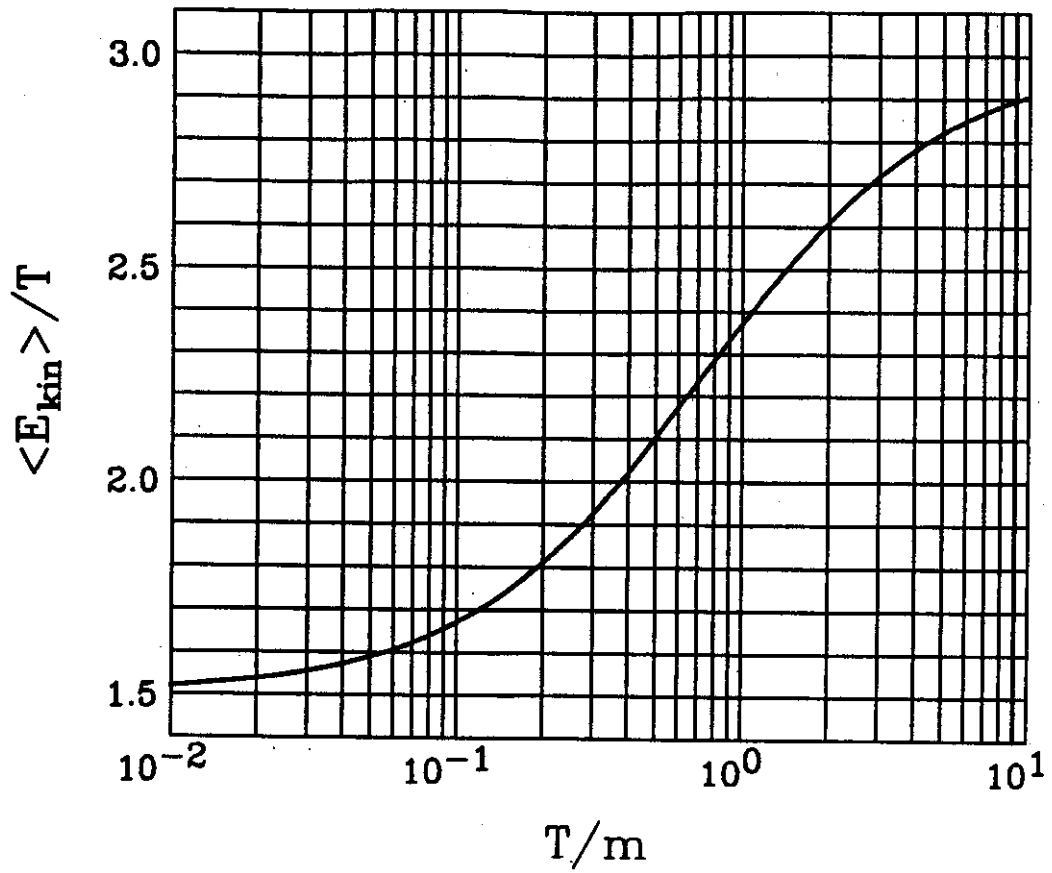
Fig. 17
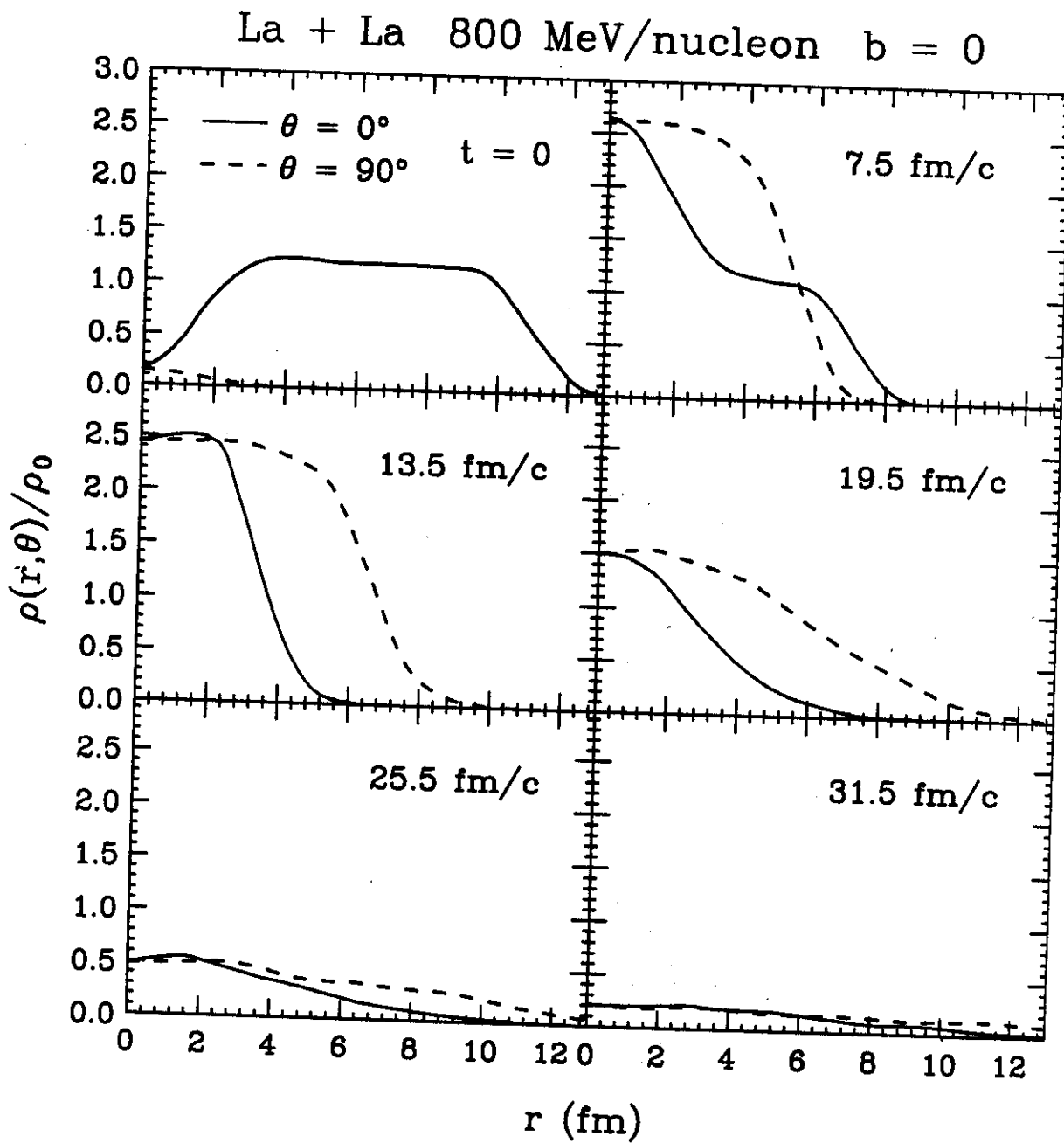
La + La   800 MeV/nucleon
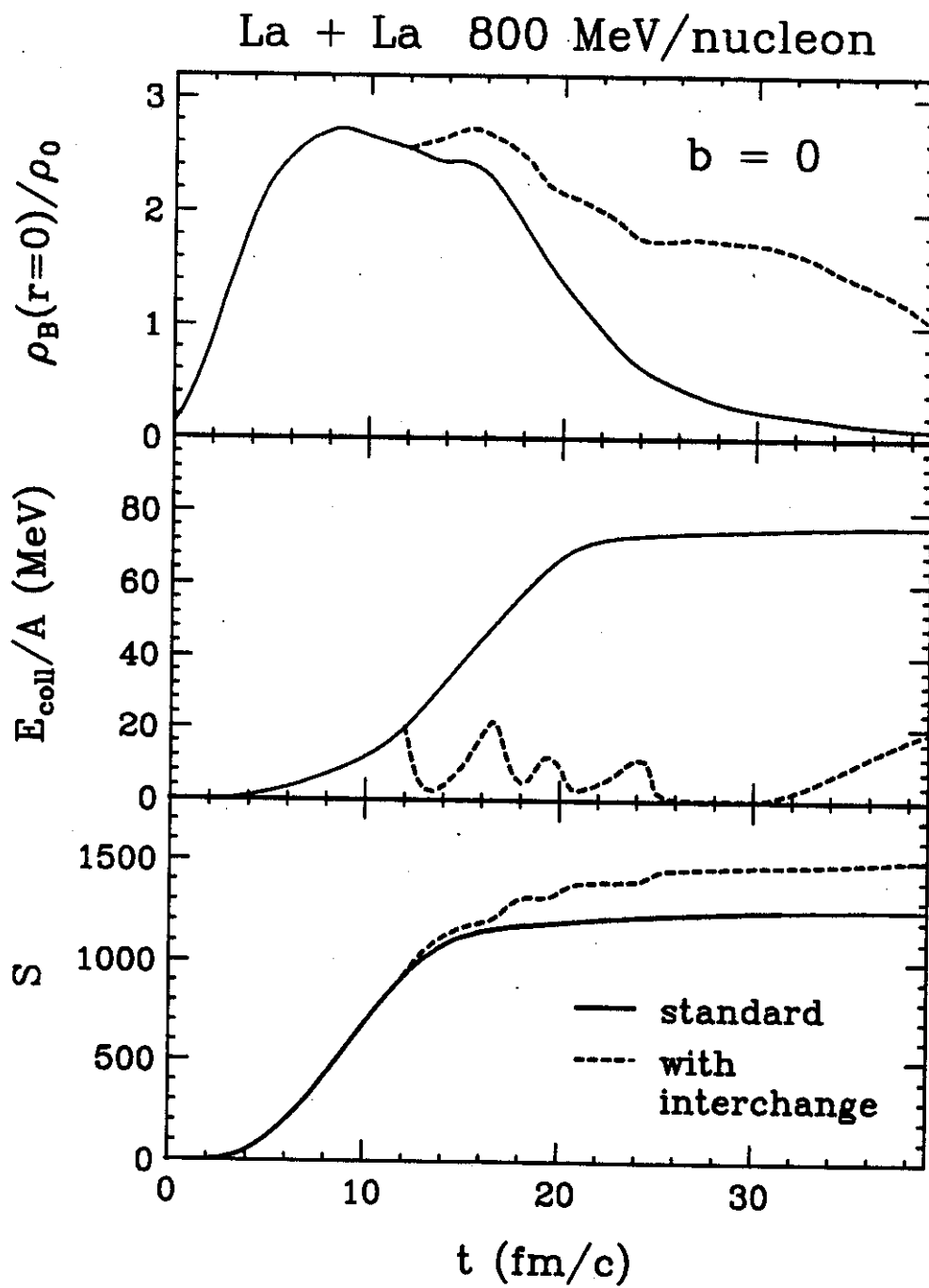
Fig. 18
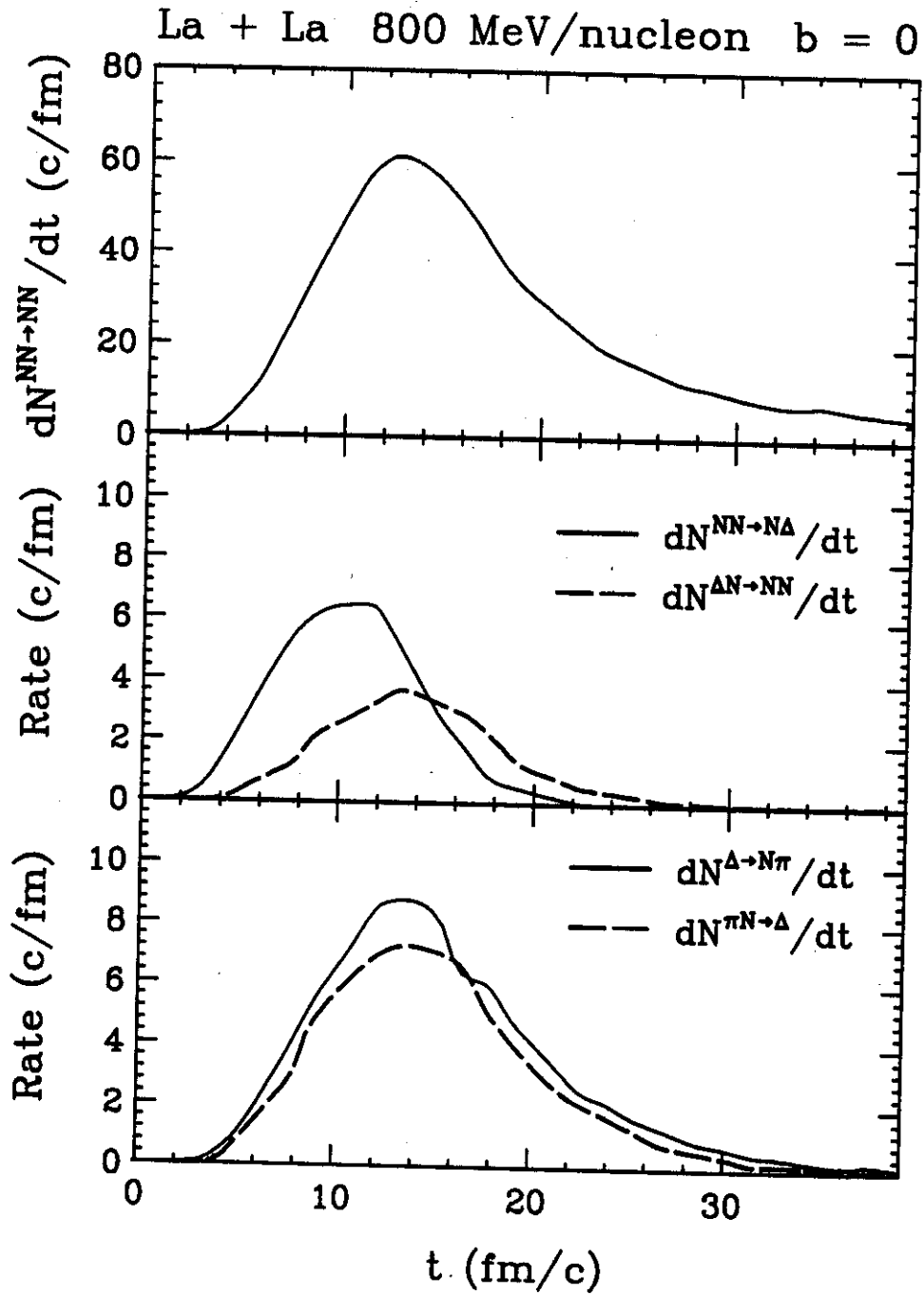
Fig. 19

La + La   800 MeV/nucleon   b = 0

Fig. 20

Fig. 21

800 MeV/nucleon   b = 1 fm   La + La

$\theta_{c.m.} = 60° - 120°$

$E^{c.m.}_{kin}$ (MeV)

d^3N/dp^3 (c^3/MeV^3)

p

d

t

π^-

$\pi^- \times 10^{-3}$

$\pi^0 \times 10^{-4}$

$\pi^0 \times 10^{-4}$

with interchange
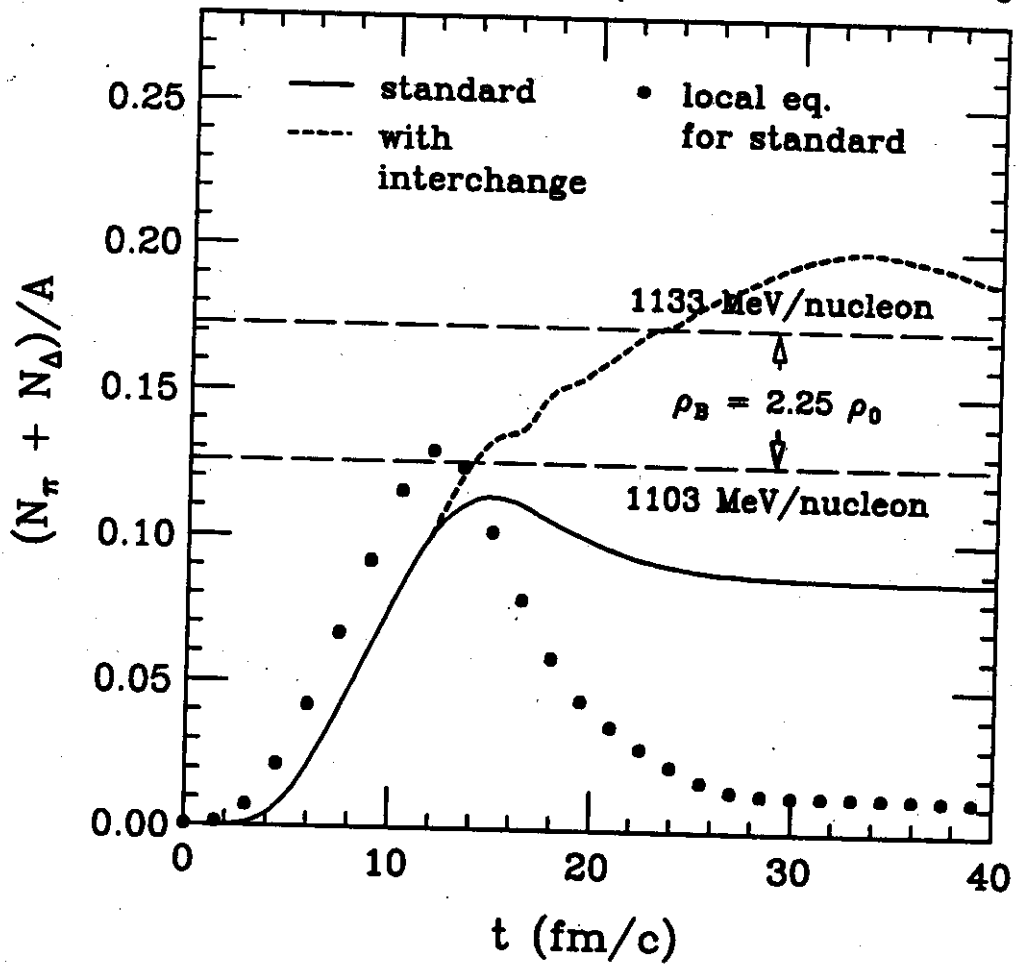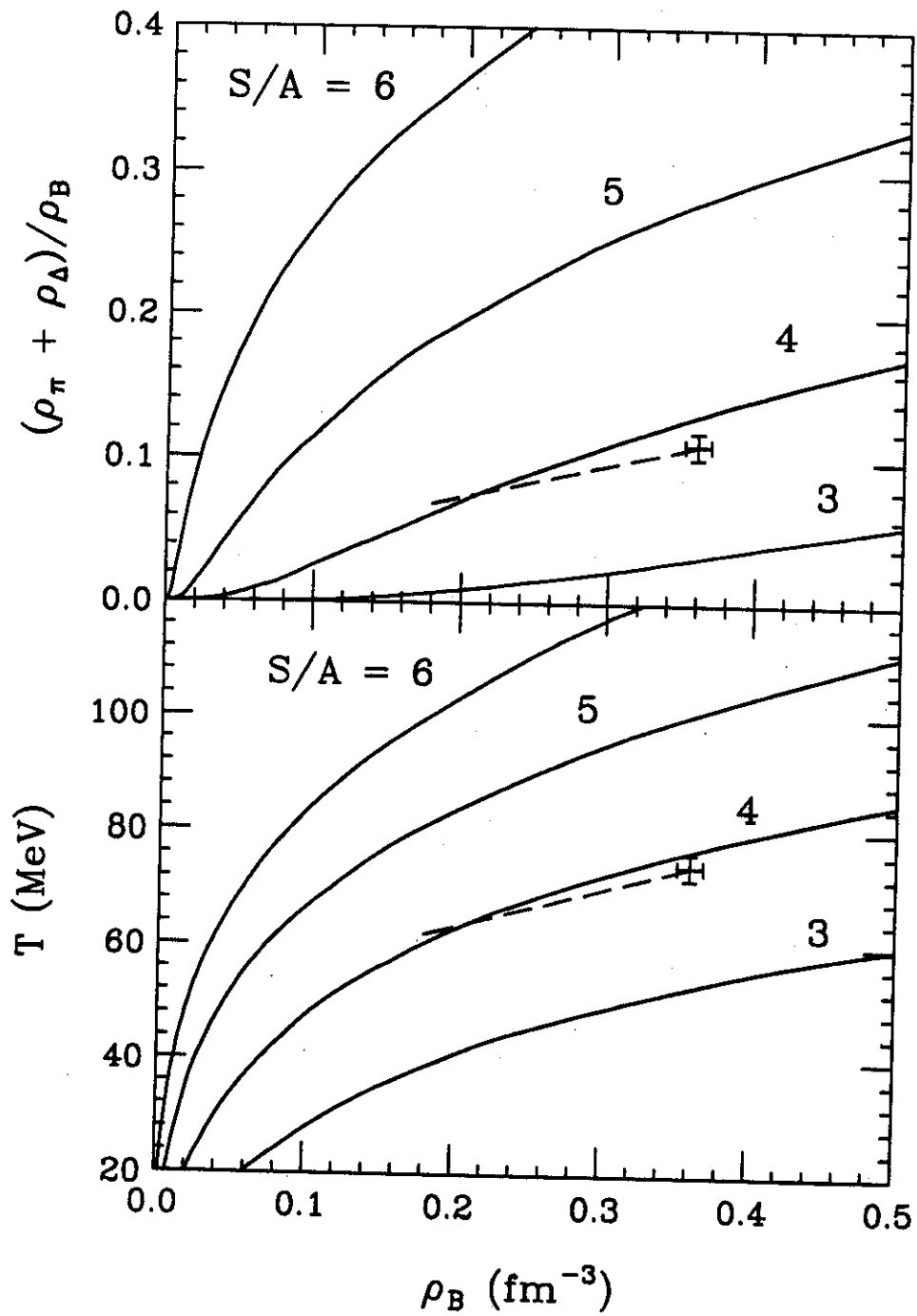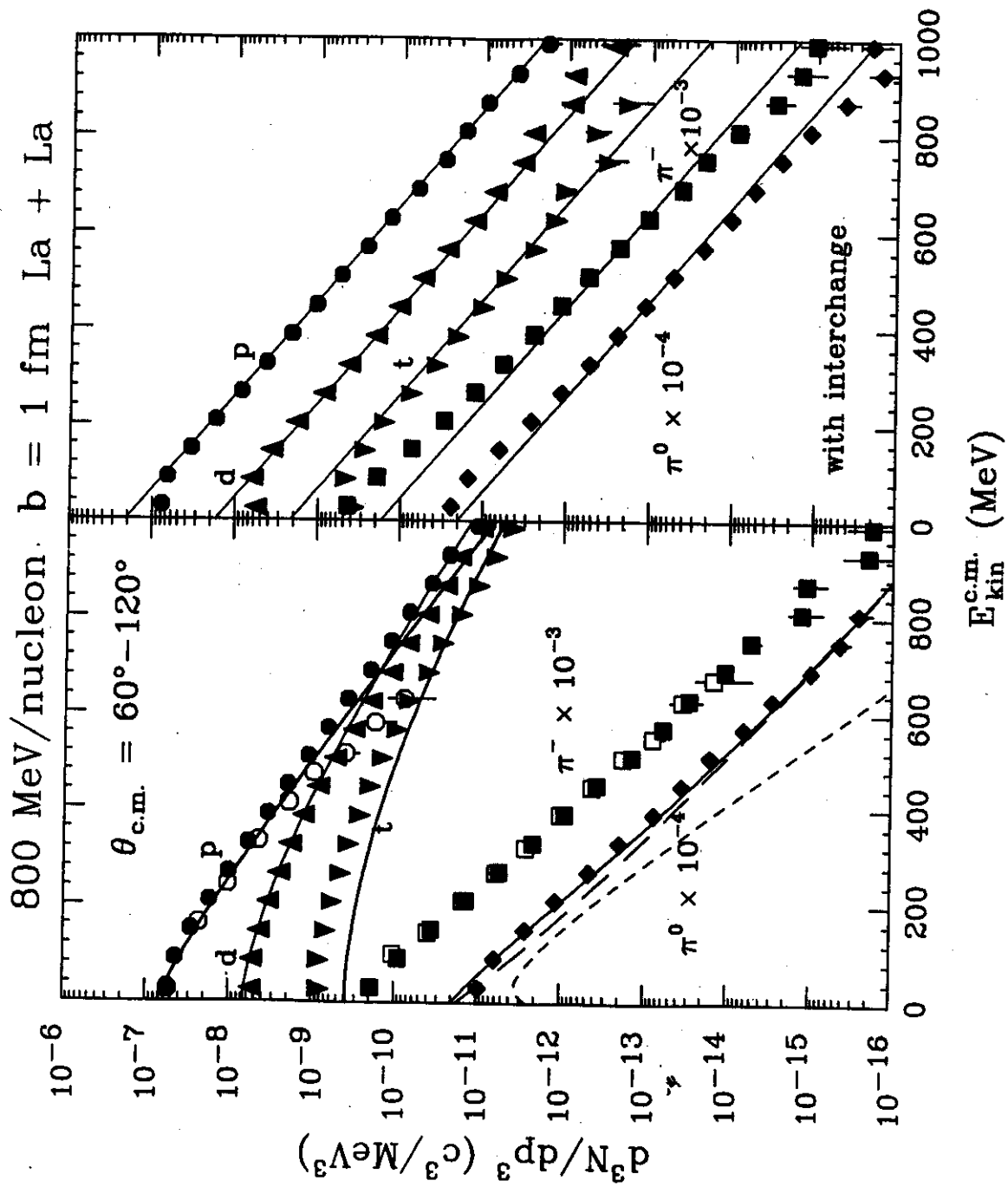
Fig. 22
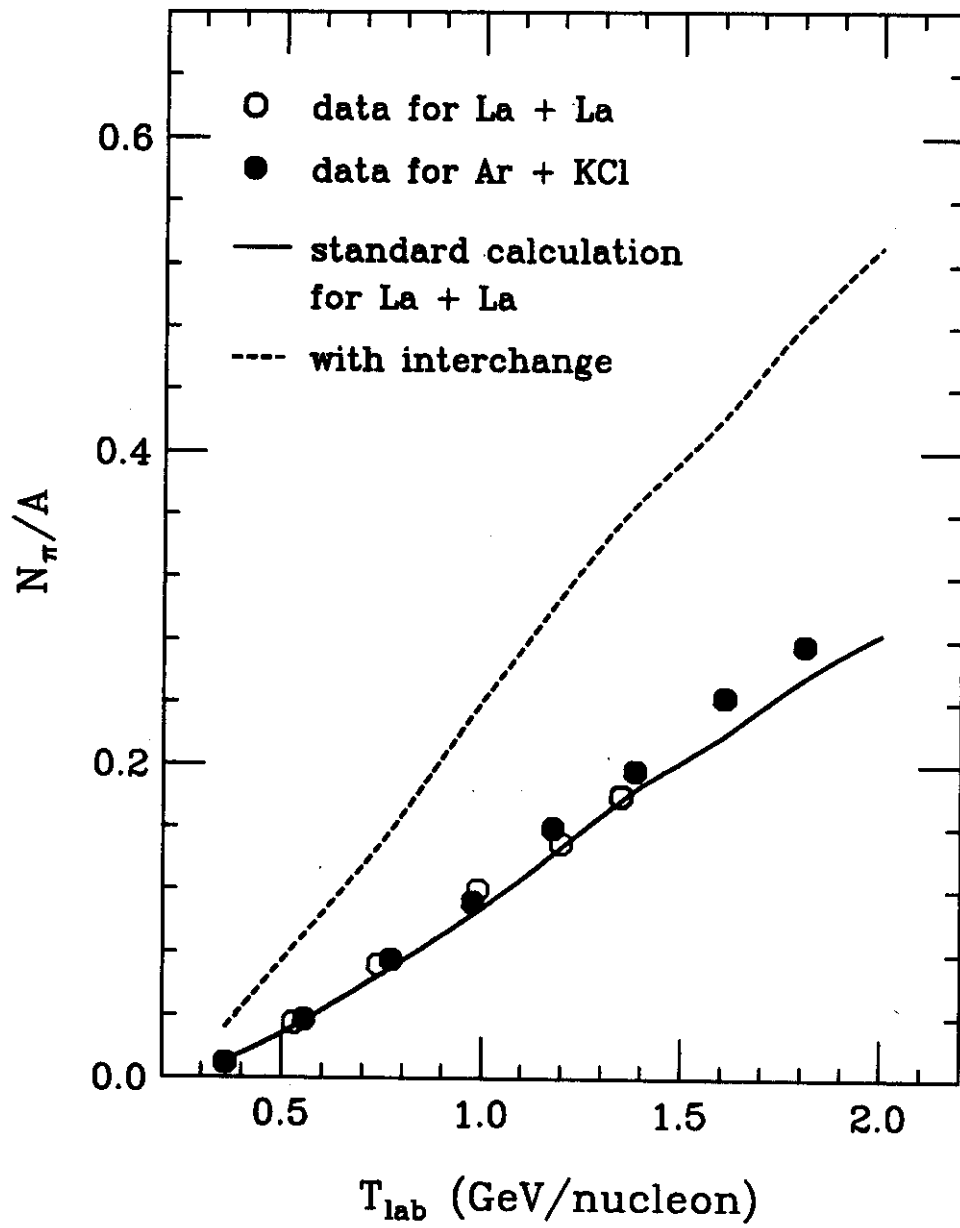
Fig. 23
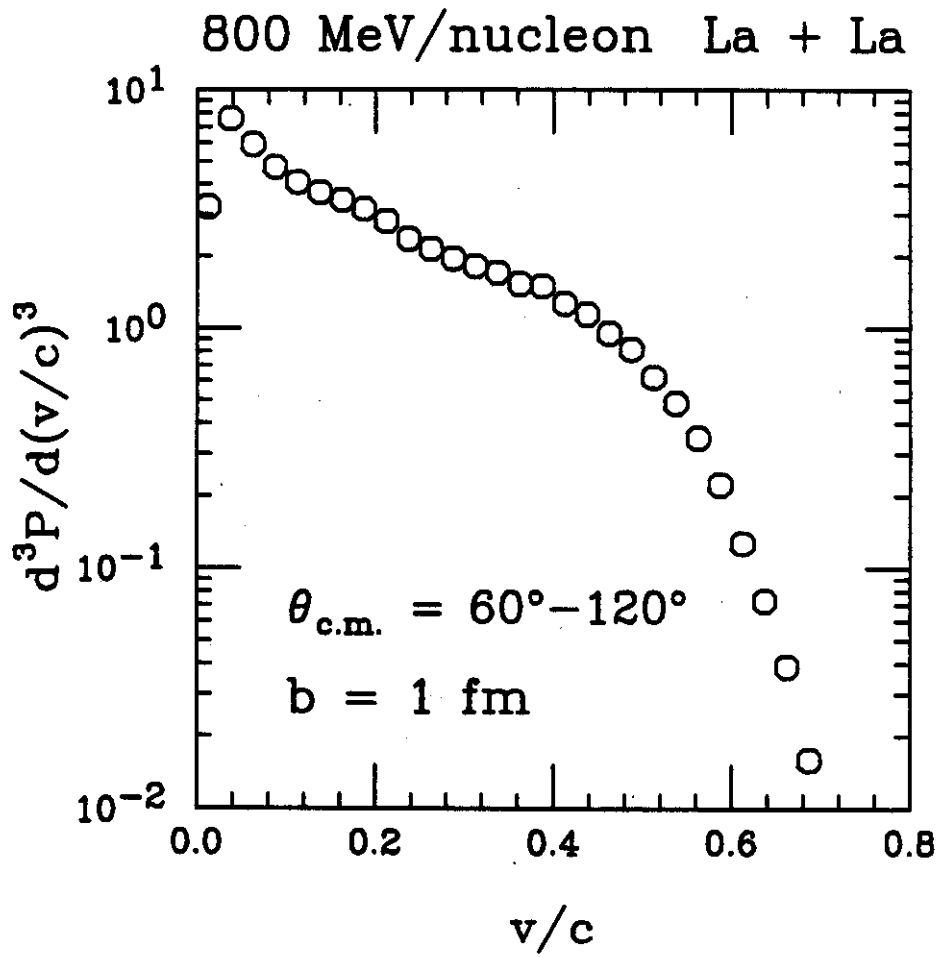
Fig. 24

1.8 GeV/nucleon Ar + KCl → π⁻

Fig. 25

1 GeV/nucleon
Au + Au   b = 7 fm

$2\pi(dN/dp^{z'})^{-1}d^2N/dp^{z'}d\phi'$

π^0

○ θ=25°
□ θ=0°
◇ θ=−25°

p>200 MeV/c

1.4
1.2
1.0
0.8

p

○ θ=25°
□ θ=0°
◇ θ=−25°

1.3
1.2
1.1
1.0
0.9
0.8

0   20   40   60   80   100

ϕ' (deg)

Fig. 26

1 GeV/nucleon   Au + Au

b = 7 fm

15 fm/c
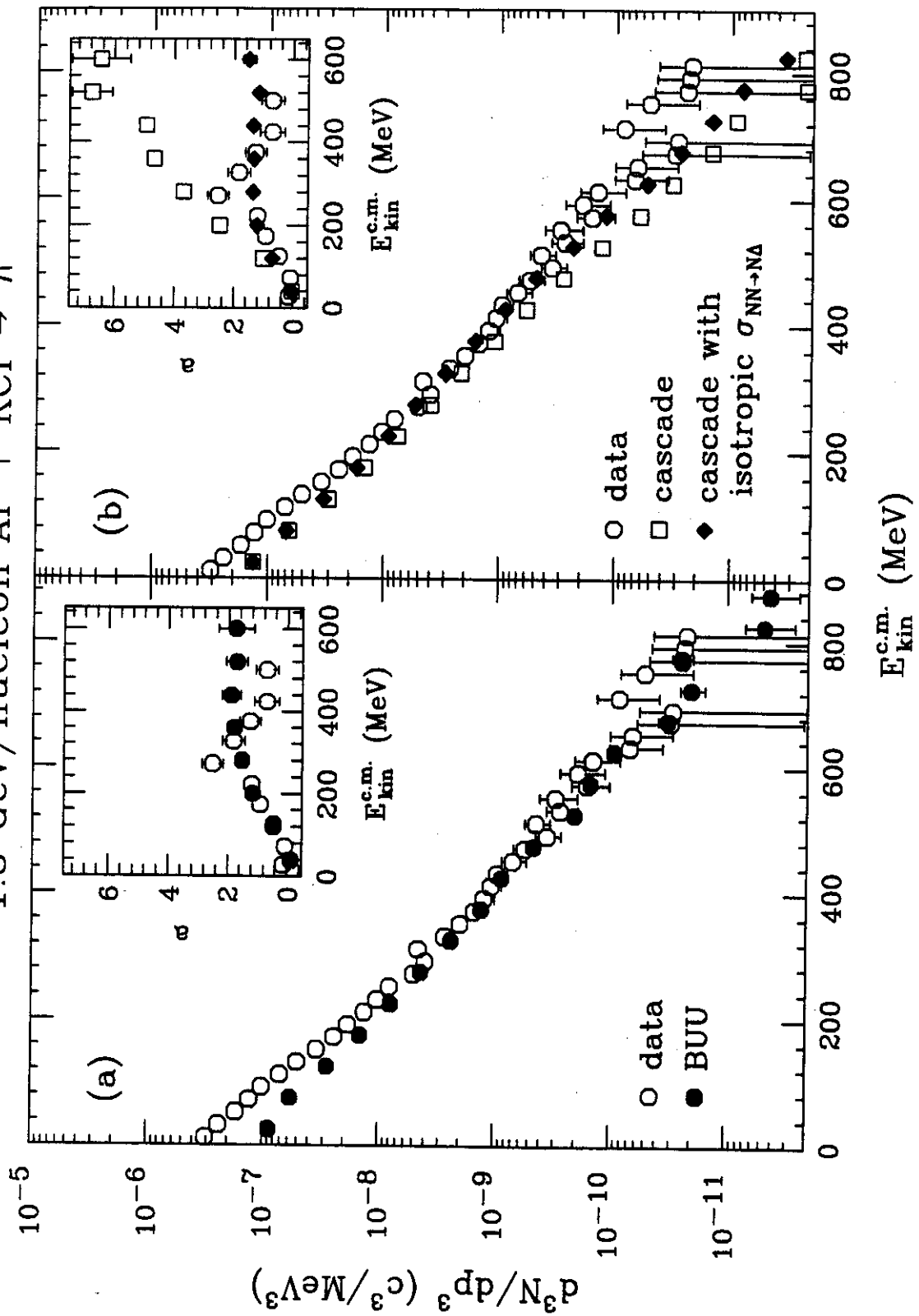
Fig. 27
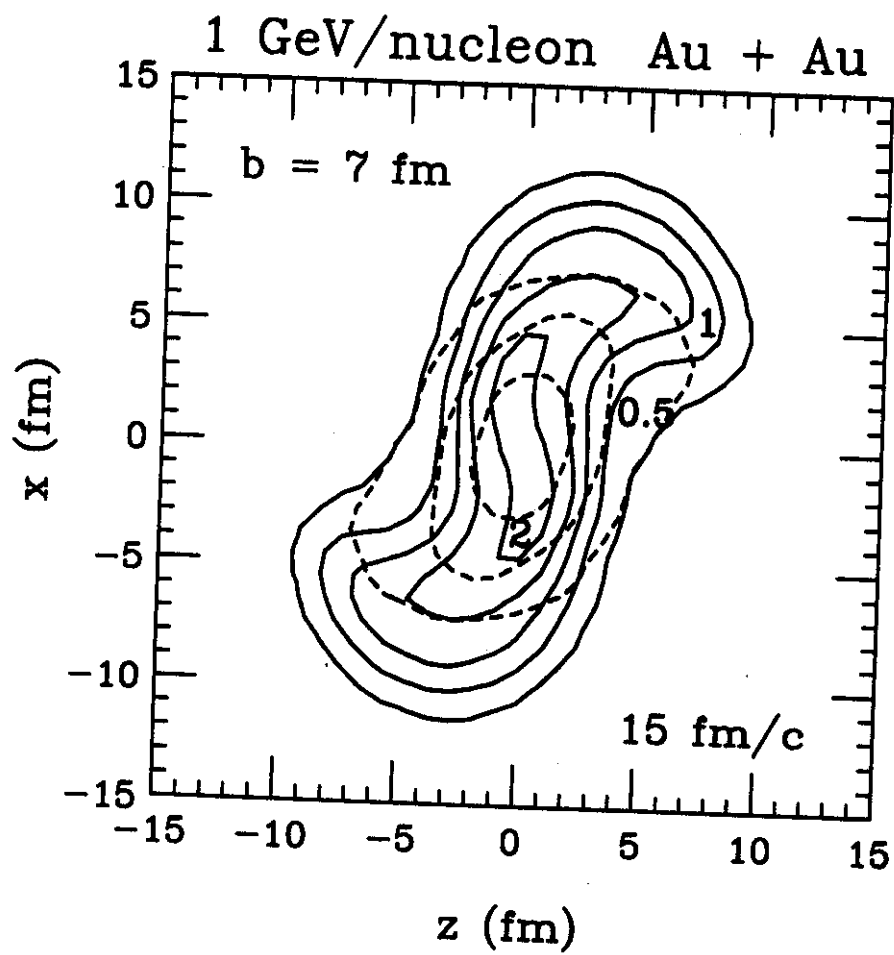
400 MeV/nucleon Au + Au
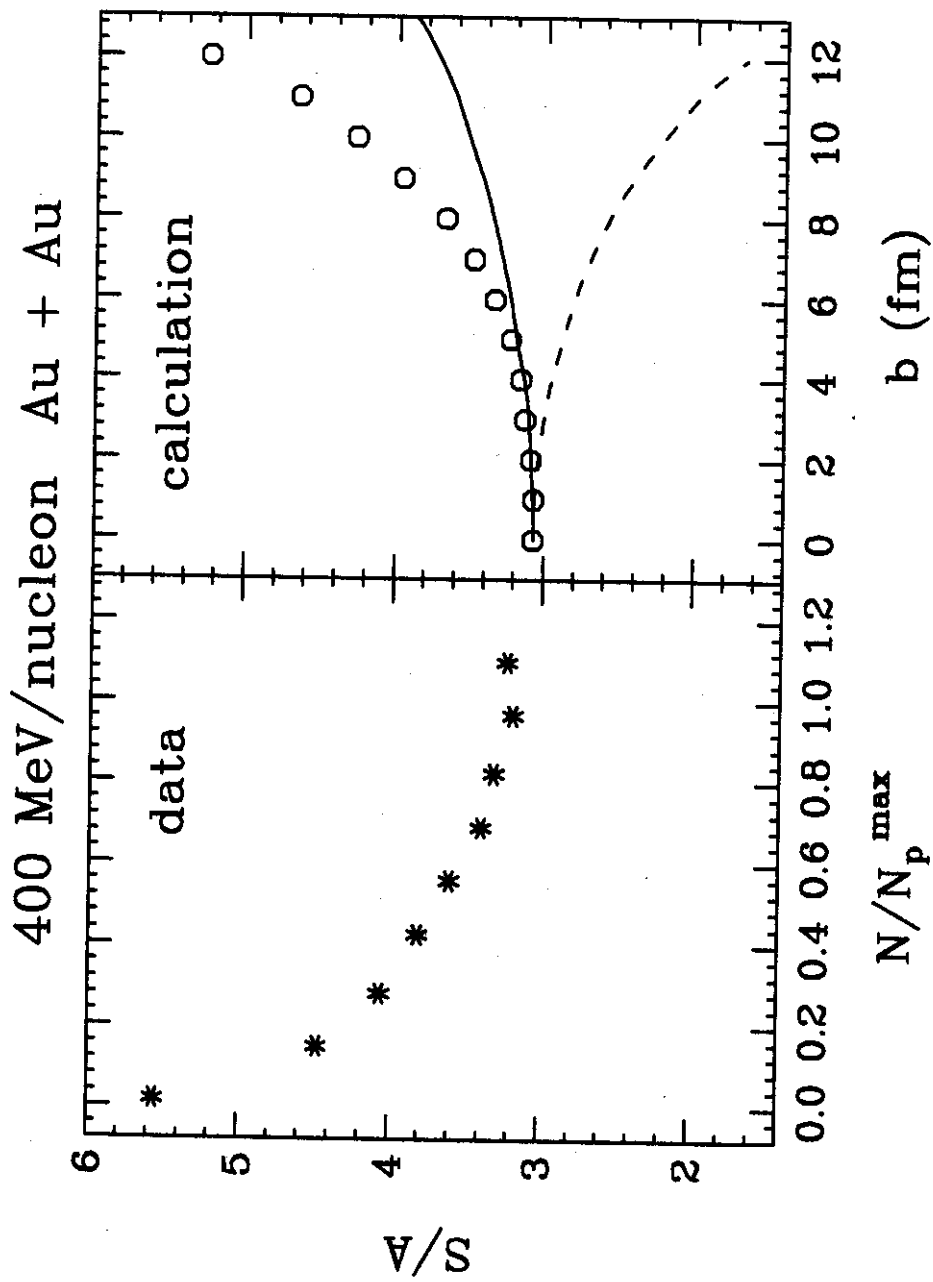
Fig. 28
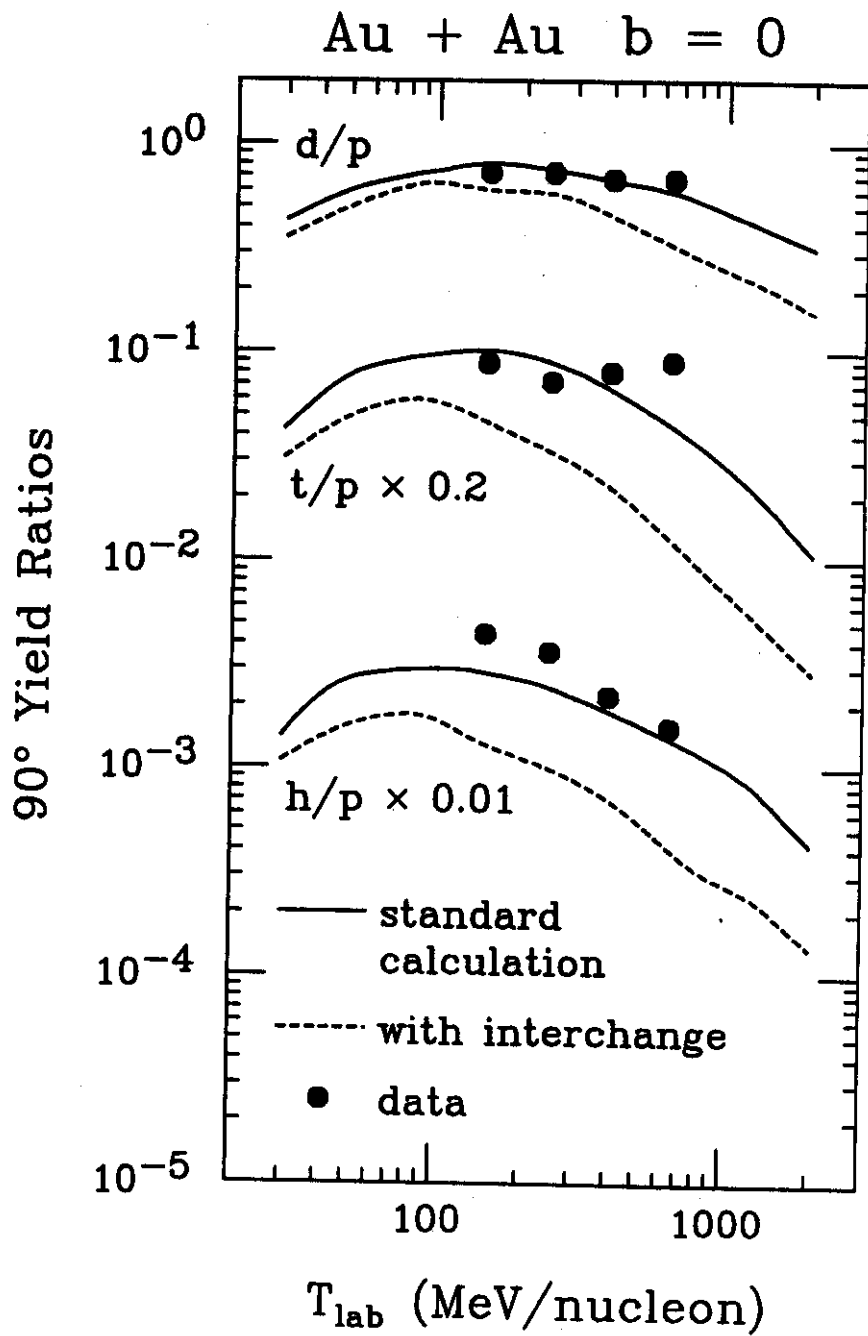
Fig. 29

400 MeV/nucleon   Au + Au

b = 0

dP/d(S/A)

S/A

Fig. 30

400 MeV/nucleon Au + Au
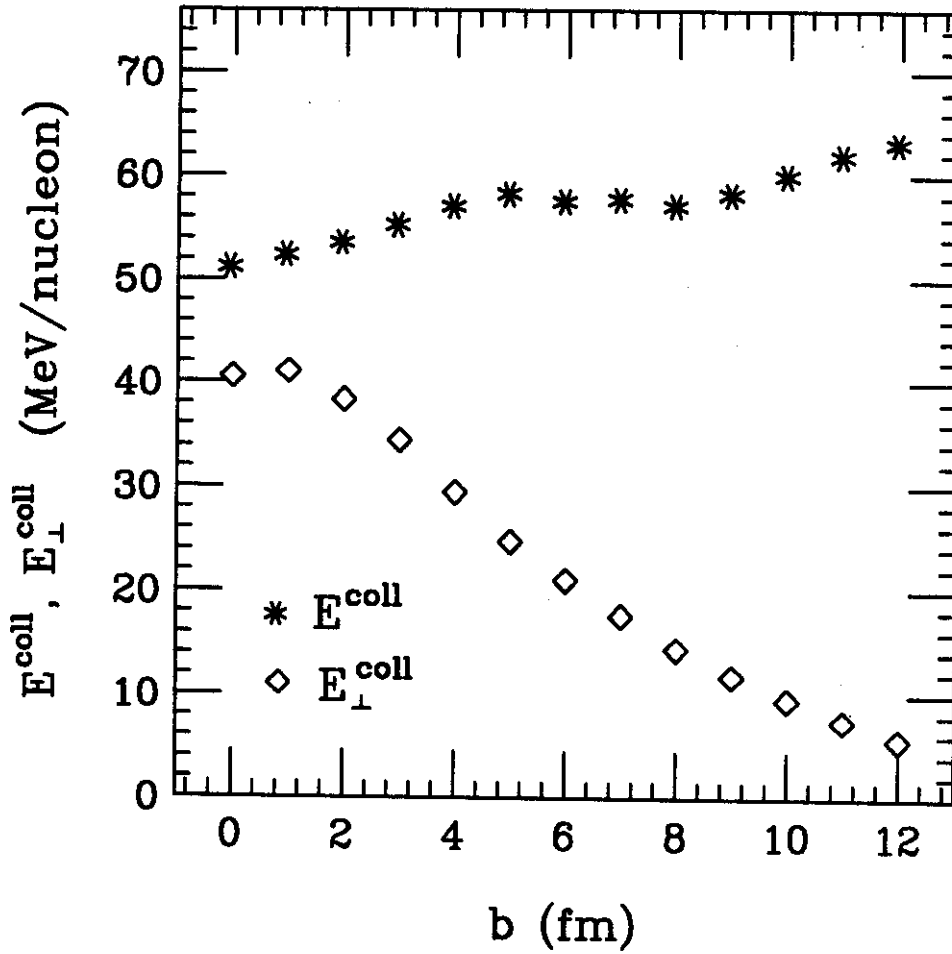
Fig. 31

Mo + Mo 60 MeV/nucleon b = 0 (with Coulomb)

$\rho(r,\theta)/\rho_0$

$v_r(r,\theta)/c$

$(S/A)(r,\theta)$

t = 0   16 fm/c   30 fm/c   56 fm/c   80 fm/c   124 fm/c   200 fm/c

— $\theta = 0°$
-- $\theta = 90°$

r (fm)
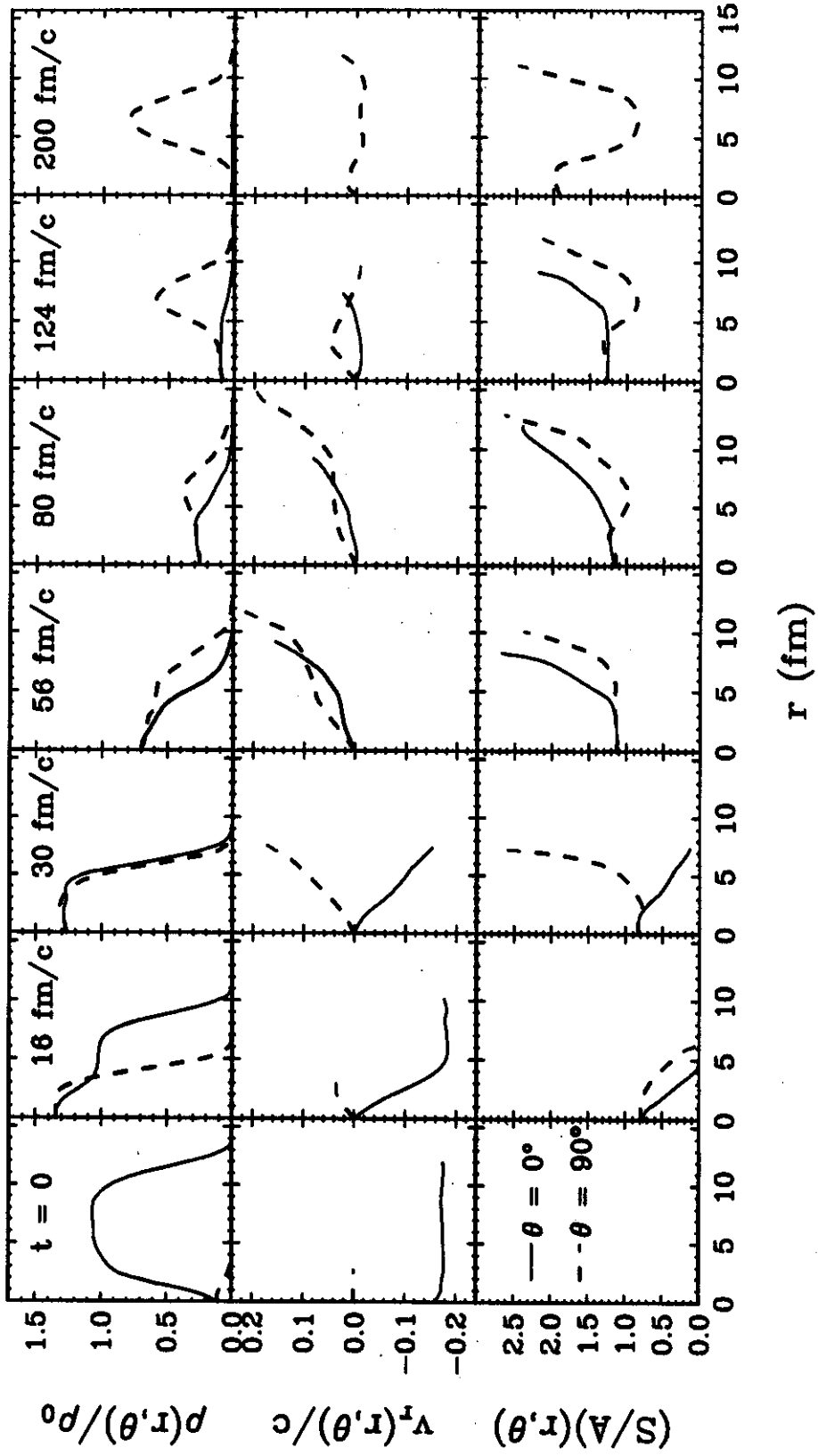
Fig. 32(a)

Mo + Mo 60 MeV/nucleon b = 0 (no Coulomb)

Fig. 32(b)

Fig. 33